NUCLEAR FUSION OF Li-6 H-2 CRYSTALS

by

Johan Otto

Submitted in partial fulfilment of the requirement for the degree

MASTER OF ENGINEERING

In the Department of Mechanical and Aeronautical Engineering

University of Pretoria

November 2016

Supervisor: Prof J. Slabber

Co-supervisor: Prof J.P. Meyer

1. Abstract

Title: Nuclear Fusion of Li-6 H-2 Crystals

Supervisor: Prof J. Slabber

Co-supervisor: Prof J.P. Meyer

Department: Mechanical and Aeronautical Engineering

Degree: Master of Engineering (Mechanical Engineering)

The inception of this study lies in mankind's need for energy in order to drive commerce, industry and development. Although several sources have been exploited in the production of energy, it is the personal opinion of the author that the most novel of these is atomic energy. It is known that humanity has become quite proficient in using nuclear fission, as is evidenced in the world's nuclear fleet; however the use of fusion for controlled energy production has not yet developed sufficiently for commercial use. It is, however, a popular anecdote that the production of energy from nuclear fusion is only forty years away – and always will be. During the literature survey, several forms of fusion producing processes are considered ranging from stellar bodies and magnetic confinement based reactors to percussive wave driven fusion as is used in fission-fusion warheads. This study focusses on the prospect of fusion at room temperature. The aim of this study is to further investigate a specific fusion process in order to determine if this may become a viable source for the production of energy. In the literature survey it is determined that the atoms in certain molecules such as Li-6 H-2 and H_2O can spontaneously overcome the Coulomb barrier and fuse to form new elements; releasing energy in the process. The mechanism for these two atoms are perceived to be similar, and the Li-6 H-2 reaction was selected based on the ease of observability, of the two α-particles that would form , should a fusion reaction take place. Furthermore, it is theorised in the literature survey that the reaction rate of the Li-6 with H-2 can be increased by exciting the molecules with X-ray radiation. In this study, an experiment is devised and conducted in order to determine if the reaction rate can indeed be accelerated as proposed. The results are compared to studies where the molecules were not excited in this manner as a baseline, and an additional determination lies in the practicality of energy production for commercial use in this manner. In the experiment, an X-ray source is used to bombard several samples of L-6 H-2 with wide spectrum Bremsstrahlung for several hours. Mathematical approximations, as well as simulations, are used in order to determine the energy deposition of the X-rays into the samples. This is done in order to determine if the process has viability as an energy production source, and in an attempt to determine if there is a specific wavelength that the process is partial to. In order to record possible fusion reactions; the samples are layered with several plastic detectors. These detectors are chemically etched and studied using microscopy, the appendix deals with experiments aimed at calibrating the process used to study these detectors. It is successfully shown that the reaction rate is increased by introducing X-rays to the Li-6 H-2 powder, however, the magnitude is far lower than was hoped for. Additionally, due to the low number of fusion reactions that took place, enough data is not available to determine an electromagnetic wavelength that is of particular interest. Finally, it is thus shown that the configuration used in this study is not a viable assembly for the production of power.

1.1. Publications

The following papers were produced as part of the study:

- Belyaev, V.B., Miller, M.B., Otto, J., Rakitianski, S.A., 'Quantum Generation Of Coherent Radiation Via The Molecular-Nuclear Transitions (Molecular-Nuclear Transitions)'. *Middle East Journal of Applied Sciences* 05.05 (2015): 107-111.
- Belyaev, V.B., Miller, M.B., Otto, J., Rakitianski, S.A., 'Nuclear fusion induced by X-rays in a crystal'. *Physical Review C*:93,034622 (2016)

The following paper was also submitted for review as part of the study:

- Belyaev, V.B., Miller, M.B., Otto, J., Rakitianski, S.A., 'Nuclear fusion induced by X-rays in a crystal'. *Submitted to Nature Physics* 15.10 (2015): NPHYS-2015-10-02778.

1.2. Acknowledgements

I would like to acknowledge the following people for their help and support:

- Prof J. Slabber, for his support and guidance;
- Prof S.A. Rakitianski, for his numerous inputs and placing his vast knowledge at my disposal
- Dr M. Miller, for his assistance and technical support at the JINR
- Ms Kravets, for her advice and support with track detectors
- Mr F de Beer, for making the resources at NECSA available and his assistance with X-ray equipment
- Mr L. Bam and Mr J. Rapakadi, for their assistance with the X-ray spectra
- Prof J.P. Meyer, for his support and eye for detail
- Dr M. du Toit, for her constant support and encouragement

I would like to thank the following institutions for their financial and technical support:

- The National Research Foundation for funding travel to and from the Joint Institute for Nuclear Research (JINR)
- The JINR for the use of its facilities and training
- NECSA for the use of its facilities
- The Thermofluids Research Group at the University of Pretoria

2. Index

2.1 List of tables

2.2 List of figures

2.3 Contents

2.4 Nomenclature

Li	Lithium
D	Deuterium (H-2)
IAEA	International Atomic Energy Agency
JINR	Joint Institute for Nuclear Research
SEM	Scanning electron microscope
Lifetime	Time taken before an atom/molecule undergoes a process $\mathrm{L} = \frac{\mathrm{time}}{\mathrm{reactions}} \times \mathrm{N_o}$ (Initial number of atoms/molecules)
NECSA	South African Nuclear Energy Corporation
NIST	National Institute of Standards and Technology
UV	Ultraviolet

3. Introduction

An analysis of Li-6D crystals indicated that spontaneous fusion might occur between the Li-6 and the H-2 within these crystals (V B Belyaev, Motovilov, & Sandhas, 1996). The rate of this spontaneous fusion is, however, too slow to be useful in power-generating applications, and is currently unknown. Past research has indicated that a nuclear resonance in Li-6D may be exploited by means of soft X-ray stimulation in order to increase the rate of the reaction shown in Equation 1 (V. Belyaev & Miller, 2011).

Li-6D + γ → Be-8 → α + α {1}

$$Q_{fusion} = BE(Be) - [BE(Li) + BE(D)] = 56.5 - (31.995 + 2.225) = 22.28 \left[\frac{MeV}{reaction}\right] = 1.602 \times 10^{-13} \times 22.28 = 3.569 \times 10^{-12} \left[\frac{J}{reaction}\right] \qquad \{2\}$$

$$Q_{decay} = 2 \cdot BE(He) - BE(Be) = 2 \cdot 28.296 - 56.5 = 0.092 \left[\frac{MeV}{reaction}\right] = 1.474 \times 10^{-14} \left[\frac{J}{reaction}\right] \qquad \{3\}$$

The output is thus 22.372 MeV/reaction[1] shown by combining equations 2 and 3.

3.1 Background

Belyaev, Motovilov and Sandhas (1996b) predicted a non-zero probability of spontaneous molecular-nuclear transitions (fusion of the atomic nuclei that constitute a molecule) for a special class of two- and three-atom molecules, under the condition that their nuclear subsystems have near-threshold resonant states of the corresponding compound nuclei (i.e. when all the nuclei of the molecule are fused). An experimental search for such a phenomenon in the molecules H_2O and Li-6D gave a lower limit of around 10^{19} years for their lifetime for the spontaneous nuclear fusion. Such an extremely small probability of the spontaneous fusion reaction could be caused by a non-zero difference between the energies of the initial molecular state and the final resonant state of the compound nucleus, since the spontaneous transitions are only possible when either the final state is below the

---

[1] This output does not as yet take the energy of the X-ray into account as this is not known.

initial one or their energies coincide exactly. Moreover, when the energies coincide, all the other quantum numbers for the initial and final states must be the same. The main reason for the small probability is the large distance between the nuclei.

After finding that the spontaneous molecular fusion is too slow to be of any interest, Belyaev, Miller and Sobolev (2006) put forward the idea of inducing such a fusion process by an external electromagnetic wave. This would be very similar to the atomic transitions in lasers. An external photon can cover the difference between the energies of the initial and final states, and make up the difference between their angular momenta and parities. It is also important that an external field can give the nuclei the kinetic energy that is needed to pass through the potential barrier.

In this study, the proposition is to explore the possibility of the electromagnetically induced fusion of molecularly bound D and Li-6 nuclei that constitute a cubic crystal while their compound nucleus Be-8 has a near-threshold resonance.

A resonant state (2+, 22.2 MeV, $\Gamma \approx 800$ keV) is close to the threshold 22.2808 MeV of its disintegration into the pair H-2 + Li-6. The dominant decay mode of this resonance is Be-8 → $\alpha + \alpha$. The initial kinetic energy of the Li-6D molecule in the crystal lattice is assumed to be zero. Therefore, the kinetic energy of the Be-8 atom is also zero. Momentum must be conserved and since the Be-8 atom is considered stationary, the energy released by the decay of the Be-8 atom must be equally shared by the alpha particles that have identical mass. Thus, the alpha particles have energies of $E\alpha$=11.2 MeV each and move away along the same line, but in opposite directions (resulting in a zero momentum of the system). These characteristics of the decay imply that the most efficient way of detecting the fusion event would be to look for the alpha-alpha particle coincidence.

In this present study, track detectors of the light-charged particles, namely CR-39 (plastic, based on the organic polymer compound allyl diglycol carbonate (ADC)) will be suggested as considered by Cassou and Benton (1978). The detectors can be used to identify the energies of alpha particles that come into contact with the detector lattice. The experiments should be conducted in the assembly of the type “multi-layer sandwich”, namely detector-sample-detector, assuming that the layout of the experiment is such that each layer of LiD powder will be encased by detectors on either side. This assembly is exposed to the X-ray radiation in order to stimulate the reaction stipulated in Equation 1. To process the results, the detectors are chemically developed using NaOH. The alpha tracks that have been etched are identified using optic microscopy.

3.2 Purpose

- The main objective of the study is to explore whether the application of X-rays increases the rate of fusions in Li-6D, i.e. Li-6 with H-2 to form Be-8.
- A secondary objective is to determine the optimum energy of the stimulating X-rays in order to maximise the rate of fusion in Li-6D.
- Finally, the implications of the results can be considered with reference to power generation.

The scope of this work is thus to determine if a lifetime of 10^{19} years, as set out by Belyaev et al. (2006), can be increased by the addition of energy in the form of X-radiation. An attempt will be made to determine the bandwidth of energy most likely to cause reactions to take place if the data obtained displays coherent patterns. Furthermore, the usefulness of the reaction as stimulated by X-rays for power generation will be evaluated.

3.3 Overview

- X-ray production methods are investigated to determine the ideal source for use in the experiment.
- X-ray spectra modelling techniques are considered to evaluate the energy distribution within the experimental sample.
- Track detectors are discussed, and etching procedures and influences are investigated.
- Nuclear fusion is explained and the reason for this investigation is mathematically described.
- Experimental procedures and results are considered.
- Reaction rate and suitability for power generation are analysed.

4. Calibration and preparation

4.1 Theory

4.1.1 Fusion

4.1.1.1 Introduction

It is believed that the dawn of the nuclear age was heralded by Einstein when he unlocked the almost boundless energy that was locked up mainly within the nucleus of atoms. Man thrust himself forward into an unknown world when he discovered the secret to the power of the core of the earth. Power could be produced by splitting the building blocks of reality itself. However, this discovery came at a time of great international turmoil, and much research was conducted on the development of destructive technologies that could utilise this power. This research also proved useful in funding other more benign endeavours. Once settled down, man was temporarily satisfied with the power that could be produced in this manner and, except for a few isolated incidents, the safest power-producing industry in the world was cultivated.

Presently, some work is aimed at the use of ceramic materials in the cladding of the reactor core to increase the maximum safe operating temperature and reactors are being designed to incorporate their own passive shut-down systems. The two great concerns of a nuclear reactor in this age are the breeding of fissile materials that could be used for the purpose of nuclear weapons and the storage of nuclear waste.

It is with this in mind that the discovery of the nucleus and the binding energy per nucleon, as shown in Figure 1, is reconsidered.

Nuclear fission is the process of moving from the right with a material like ^{235}U splitting to the left. The increased binding energy per nucleon is released as kinetic energy to produce the energy that is harvested. It is, however, very clear that results that are far more drastic could be obtained if the movement occurs from the early left to the right through a process called fusion.

This process was first used by humans when an attempt was made to increase the yield of atomic bombs. These thermonuclear warheads used the high temperature and pressure generated by an atomic explosion to fuse lightweight nuclei and produce energy similar to the heat that powers the stars.

4.1.1.2 Processes

The binding energy per nucleon, as seen in Figure 1, is at a maximum at $A \approx 56$ and decreases slowly for heavier nuclei.

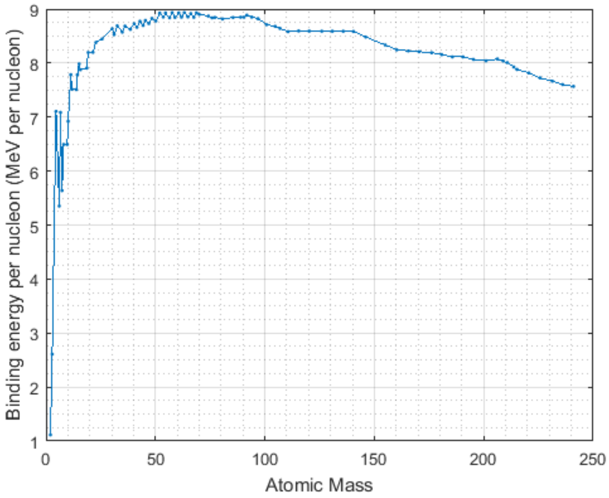

Figure 1: Binding energy per nucleon. Adapted from: (OpenSTAX, n.d.)

Inverting the process of fission, where a heavy nucleus is split into two or more lighter and more tightly bound nuclei, the process of fusion should produce energy by combining light nuclei. The energy released as kinetic energy is thus the difference between the binding energies of the initial and final states.

The Coulomb repulsion between two positively charged nuclei is the greatest problem when considering nuclear fusion. This repulsion must first be overcome before the nuclei can get close enough for the strong nuclear force to take over and fuse the nuclei into a single nucleus. The Coulomb potential is generally given by Equation 4:

$$V_C = \frac{ZZ'e^2}{4\pi\varepsilon_0(R+R')} \qquad \{4\}$$

In Equation 4, *Z* and *Z′* indicate the atomic numbers of the two nuclei involved respectively, *R* and *R′* are the effective radii (Martin, 2009).

This repulsive potential reaches its maximum when the nuclei of the radii *R* and *R′* touch each other i.e. $r = R + R'$.

Equation 4 can be reduced considering that generally $R = 1.2A^{\frac{1}{3}}$ fm (Martin, 2009). This is shown in Equation 5.

$$V_C = \left(\frac{e^2}{4\pi\varepsilon_0\hbar c}\right) \cdot \frac{\hbar c ZZ'}{1.2\left(A^{\frac{1}{3}}+(A')^{\frac{1}{3}}\right)} = 1.198 \cdot \frac{ZZ'}{A^{\frac{1}{3}}+(A')^{\frac{1}{3}}}\,[MeV] \qquad \{5\}$$

Using Z=3, Z′=1 and A=6, A′=2 for Li-6 and H-2 respectively, it is calculated that the maximum height of the potential barrier is V_C = 1.168 MeV, as described in Equation 4.

This can be considered a small amount of energy and should be achievable by simply colliding the nuclei using an accelerated beam. The accelerators, however, are not efficient for energy generation, as they consume much more energy than they produce. The practical reality is also that nearly all the particles would be scattered elastically in such collisions (Martin, 2009). In practice, the Coulomb barrier is thus overcome by supplying the energy thermally. The temperature that would be required can be calculated using Equation 6

$$T = \frac{E}{k_B} \; , \tag{6}$$

where k_B is Boltzmann's constant[2]. This means that a temperature of $1.355 \times 10^{10}\ K$ would be required for the Li-6D fusion. This temperature is an enormous hurdle, since no material can remain in a solid state at this temperature. Conventional shielding would thus be ineffective and other means would be required to contain such energetic plasma. The typical temperature of stellar interiors is 10^8 K, which is lower than the calculated temperature. Therefore, other phenomena that allow fusion to occur at lower temperatures must be at play in nature.

The first and most prominent is the process of quantum tunnelling. This means that the entire Coulomb barrier does not have to be overcome from above and that the reaction can thus occur at a lower energy. When considering quantum tunnelling in this instance, the Gamow factor (a function of the relative velocities and charges of the reaction products) is of the greatest relevance. Generally, the probability of Coulomb barrier penetration is represented by $P \propto e^{-G(E)}$, where G(E) is the Gamow equation described in Equation 7.

$$G(E) = \sqrt{\frac{E_G}{E}} \tag{7}$$

In Equation 7, E_G can be determined using Equation 8.

$$E_G = 2m^* c^2 (\pi \alpha Z Z')^2 \tag{8}$$

In Equation 8, m^* represents the reduced mass as calculated in Equation 9 and α is the Sommerfeld constant[3].

$$m^* = \frac{m \times m'}{m + m'} \tag{9}$$

The probability of barrier penetration is thus almost zero at low energies and increases as *E* increases. However, in reality, pair of nuclei is never isolated.

In plasmas, the particles present at a mean temperature have a Maxwellian energy distribution. This means that several particles have energies greater than the mean. The Maxwell-Boltzmann distribution is shown in Equation 10, and Figure 2 shows an example of this distribution.

$$f(v) = \sqrt{\left(\frac{m}{2\pi k_B T}\right)^3}\, 4\pi v^2 e^{-\frac{mv^2}{2k_B T}} \tag{10}$$

---

[2] $k_B = 8.6173324 \times 10^{-5} \left[\frac{eV}{K}\right]$ (CODATA, 2010a)

[3] $\alpha = 7.297\,352\,5698 \times 10^{-3}$ (CODATA, 2010b)

Equation 10 thus represents the probability per unit speed of finding a particle with a speed near v. The distribution of Equation 10 is given by *a* in Equation 11.

$$a = \sqrt{\frac{k_BT}{m}} \qquad \{11\}$$

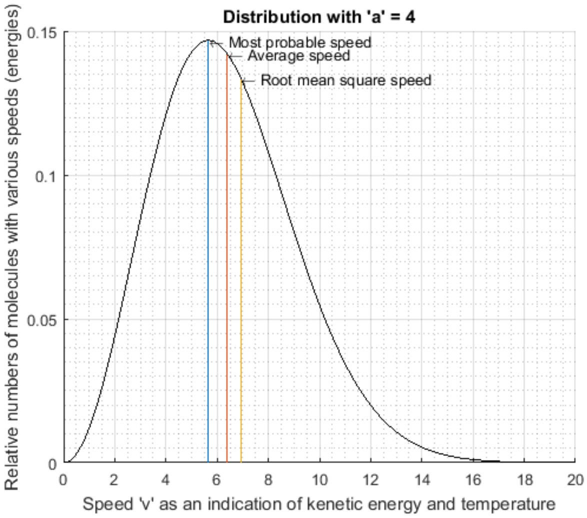

Figure 2: Maxwellian distribution. Adapted from: (HVAC Air Conditioning Designs, 2010)

The interplay is such that there is only a narrow band (dv) where these effects are significant enough to allow a reaction to take place[4], since the Maxwellian distribution vanishes at higher temperatures, but the Gamow function increases with higher energies. The probability of having both nuclei at the required relative velocity within the range v and $v + dv$ can thus be given by Equation 12 (Martin, 2009).

$$P(v) \cdot dv = \left(\frac{2}{\pi}\right)^{\frac{1}{2}} \left(\frac{m^*}{k_BT}\right) e^{\frac{-mv^2}{2k_BT}} v^2 \cdot dv \qquad \{12\}$$

The average fusion cross-section is represented by Equation 13 (Martin, 2009).

$$\langle \sigma_{ab} v \rangle = \int_0^\infty \sigma_{ab} v P(v) \cdot dv\,, \qquad \{13\}$$

where the elementary two-body cross-section σ_{ab}, for the fusion of particles *a* and *b*, is parameterised in Equation 14 (Martin, 2009).

$$\sigma_{ab}(E) = \frac{S(E)}{E} e^{-\left(\frac{E_G}{E}\right)^{\frac{1}{2}}} \qquad \{14\}$$

In Equation 14, *S(E)* is the so-called astrophysical S-factor where for ^{6}Li(d,α)α; $S(E) \xrightarrow[E\to 0]{} 16.9[MeV]$ (Musumarra, Pizzone, Blagus, Bogovac, Figuera, Lattuada, Milin, Miljanic, Pellegriti, Rendic, Rolfs, Soic, Spitaleri, Typel, Wolter & Zadro, 2001) and the exponential function follows from the tunnelling mentioned by combining equations 5 and 7.

---

[4] dv represents the band at which the velocity of the particles allows a reaction to take place.

Using the number of densities of n_a for Li-6 and n_b for H-2, the reaction rate can be determined as shown in Equation 15:

$$R_{ab} = n_a n_b \langle \sigma_{ab} v \rangle = n_a n_b \left(\frac{8}{\pi m^*}\right)^{\frac{1}{2}} \left(\frac{1}{k_B T}\right)^{\frac{3}{2}} \int_0^\infty S(E) e^{\left(-\frac{E}{k_B T} - \left(\frac{E_G}{E}\right)^{\frac{1}{2}}\right)} \cdot dE \qquad \{15\}$$

For Equation 15, the maximum of the integrand is when E = E_0 as calculated in Equation 16 (Martin, 2009).

$$E_0 = \left(\frac{1}{4} E_G (k_B T)^2\right)^{\frac{1}{3}} \qquad \{16\}$$

This can be represented as shown in Figure 3.

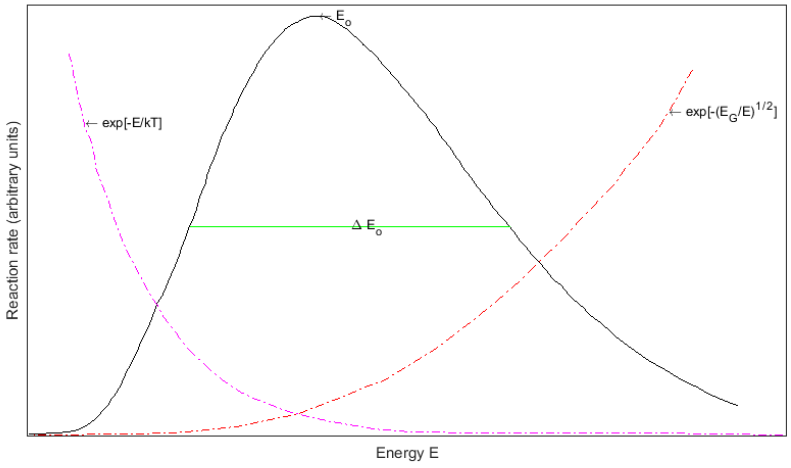

Figure 3: Fusion reaction rate. Adapted from: (Martin, 2009)

The dashed curve on the right of Figure 3 represents the barrier penetration, whereas the left dashed curve is proportional to the Maxwell distribution. The solid curve is the combined effect that is proportional to the probability of fusion with a maximum at E_0 and a width of ΔE_0 (Martin, 2009).

Fusion thus takes place within the range of E_0 and $E_0 + \Delta E_0$, where ΔE_0 is represented by Equation 17 (Martin, 2009).

$$\Delta E_0 = \frac{4}{3^{\frac{1}{2}} 2^{\frac{1}{3}}} E_G^{\frac{1}{6}} (k_B T)^{\frac{5}{6}} \approx 1.63 E_G^{\frac{1}{6}} (k_B T)^{\frac{5}{6}} \qquad \{17\}$$

At a temperature $T = 2 \times 10^7\ K$, for example, using $m_{Li-6} = 5\,603 MeV$ and $m_D = 1\,876 MeV$ (Audi, Wang, Wapstra, Kondev, MacCormick & Xu, 2012), it is calculated that $E_G = 13.296 MeV$ and subsequently $E_0 = 21.453 keV$ and $\Delta E_0 = 14.043 keV$. This is an obtainable range. However, if room temperature is considered, $T \approx 300K$, then $E_0 = 13.048 eV$ and $\Delta E_0 = 1.341 eV$. This range is nearly insignificant and it would be extremely difficult to not only produce so little energy, but also to confine the energy to such a narrow band.

4.1.1.3 *Fusion reactors*

Deuterium is considered a fuel, since it is available in large quantities in seawater and is relatively easy to separate. Furthermore, the Coulomb barrier that needs to be overcome is the same as for a proton, and the following exothermic reactions can be induced as shown in equations 18 and 19.

H-2 + H-2 → He-3 + n + 3.27 MeV {18}

H-2 + H-2 → H-3 + p + 4.03 MeV {19}

Tritium could also be used, as shown in Equation 20, since it produces more energy than the other known reactions, and has a larger fusion cross-section, as shown in Figure 4.

H-2 + H-3 → He-4 + n + 17.62 MeV {20}

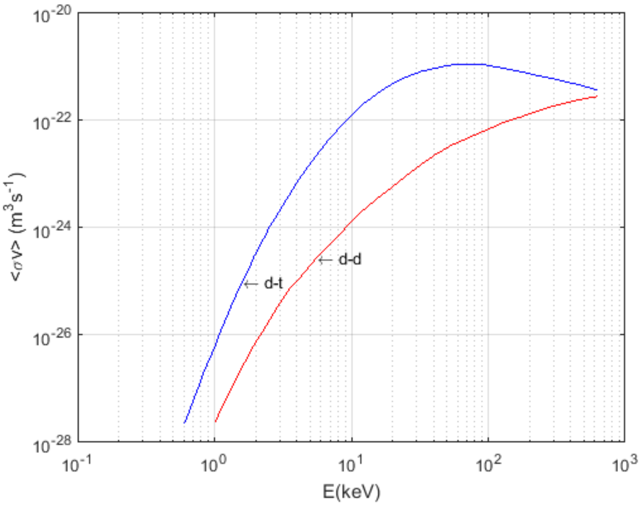

Figure 4: Values of the quantity $\langle\sigma v\rangle$. *Adapted from:* (Martin, 2009)

In Figure 4 the top line is for the d-t reaction shown in Equation 20 and the bottom line is for the combined d-d reactions that are indicated in equations 18 and 19.

The disadvantage of using tritium is that it has a half-life of only 12.32 years (IAEA, 2012) and does not occur naturally. The manufacturing processes are also expensive.

The energy produced by fusion processes will be lost by heat radiated from the hot plasma, mostly through electron Bremsstrahlung. The power loss is proportional to $T^{\frac{1}{2}}Z^{2}$ per unit volume (Martin, 2009) where Z is the atomic number of the ionised atoms. Thus, the power produced by fusion will be exceeded by the power lost at a certain temperature. The fusion inefficiencies are worsened by neutrons that escape containment and thus external energy must be provided to sustain the process.

The Lawson criterion is a numerical expression that provides a measure as to the practicality of a particular design shown in Equation 21.

$$L = \frac{energy\ output}{energy\ input} = \frac{R_{ab}t_{c}Q}{energy\ input} \qquad \{21\}$$

For Equation 21, Q is the energy released in the fusion reaction, R_{ab} is the reaction rate, and t_c is the plasma confinement time.

Clearly, L should be greater than 1 for a useful system. This indicates that either a long containment time or a high particle density (or both) is essential for a useful system. The plasma containment is done using either inertial or magnetic confinement. Most research has gone into magnetic confinement where the plasma is confined by magnetic fields and heated by electromagnetic fields (Martin, 2009). Particle losses can be reduced by magnetic geometry that ensures indefinite circulation. The simplest configuration is a toroidal field, which is achieved by passing current through a donut-shaped solenoid. For practical applications, the toroidal field has a poloidal field superimposed, in order to correct non-uniformity, and the combination leads to particles travelling around the axis of the torus in helical orbits. Reactors that make use of these principles are called tokamaks, where the plasma itself generates the poloidal field.

4.1.2 Nuclear transitions in molecules

4.1.2.1 Introduction

In forcing nuclei to fuse, there are methods other than raising the temperature to assist the process. Since the greatest obstacle to be overcome in fusion is the Coulombic barrier between the nuclei, most approaches require that the particles be supplied with energy equivalent to that represented by the barrier. The approach used in this instance, however, relies on quantum tunnelling to pass through the barriers between the nuclei. Quantum tunnelling is used to describe the quantum mechanical phenomenon when a particle moves through a barrier that it would not be able to pass through in terms of classical laws. It is generally explained using the Heisenberg uncertainty principle due to the wave-particle duality of nature.

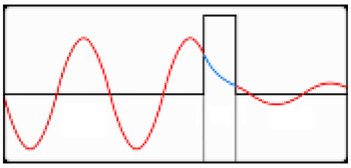

Figure 5: Visualisation of quantum tunnelling

Figure 5 indicates a particle, with an energy represented by the frequency of the wave, meeting an obstacle that requires more energy than is available to pass. The wave’s amplitude represents the particle’s probability to exist at a certain point. Through collapsing the probability on the other side of the obstacle, the particle can pass through the obstacle without a loss of energy.

The likelihood of the nuclei tunnelling through the barrier can be increased by either making the barrier thinner, or keeping the particles close to one another for a prolonged period – meaning that penetration may even occur at a low probability. This can be done by placing the nuclei that are to be fused within a molecule, where they remain in close proximity for an extended period. The barrier within the molecule is then reduced even further by electron screening (Belyaev, Motovilov & Sandhas, 1996a). Electron screening occurs in multi-electron atoms where the outermost electrons experience a reduced nucleic charge due to screening by the innermost electrons. Therefore, the presence of electrons reduces the effective nuclear charge while they exist between the nucleus of one atom and another particle.

Furthermore, it was noticed that resonance could possibly amplify the nuclear transition probability for certain systems (Belyaev et al., 1996a). If the compound nucleus has a resonant state at the threshold energy, a molecule and nucleus can be considered as two degenerate states of the same physical system if the quantum numbers of the nuclear resonance and molecular state coincide (Belyaev et al., 2006). Some work such as (V. Belyaev et al., 2006) has been done to study the fusion of Li-6D → Be-8 and this research is considered in this section.

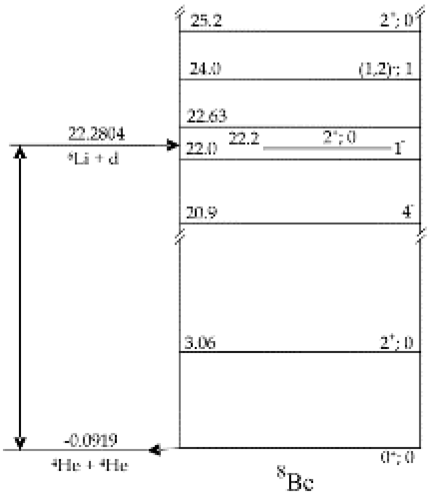

Figure 6: Be-8 state representation (Tilley, Cheves, Godwin, Hale, Hofmann, Kelley & Weller, 2004)

4.1.2.2 *Muon-catalysed fusion*

Muon-catalysed fusion is a process that involves the use of muons to facilitate fusion at temperatures that are significantly lower than in stellar instances. A muon is an unstable subatomic particle that is analogous to an electron because it has a charge of -1 and a spin of $\frac{1}{2}$, but its mass is 207 times that of an electron. The half-life of a muon is 2.2 μs (Jones, 1986). However, in this time, it is capable of forming mu-mesic atoms by replacing the electron in an ordinary atom. Mu-mesic atoms are smaller than typical atoms because the greater mass of the muon allows the orbit of the muon to be proportionally closer to the nucleus of the atom[5] (Bracci & Fiorentini, 1982).

Since an H-atom with a muon is far smaller, the distance between atoms in a molecule where one is mu-mesic is also significantly smaller. The result is that there is a greater probability that nuclear fusion could occur, so that fusion occurs in such molecules at a rate 10^{85} times faster than in molecules without mu-mesic atoms (Rafelski & Harley, 1991). Once the fusion has occurred, the muon is released and it can be utilised to facilitate another fusion event. That is why it can be considered a catalyst. Jones (1986) found that a muon could be used to catalyse more than 150 reactions before being lost to decay or sticking to an atom with Z>1, although muon-catalysed fusion can occur using such atoms as well (Harley, Muller & Rafelski, 1990). This process is shown in Figure 7, where *d* refers to deuterium, *t* refers to tritium and μ refers to a muon.

---

[5] This is only the case for an atom that would only contain one electron. Should several electrons be bound to an atom, its size would be determined by the electrons, even though the muon orbit would still be significantly closer.

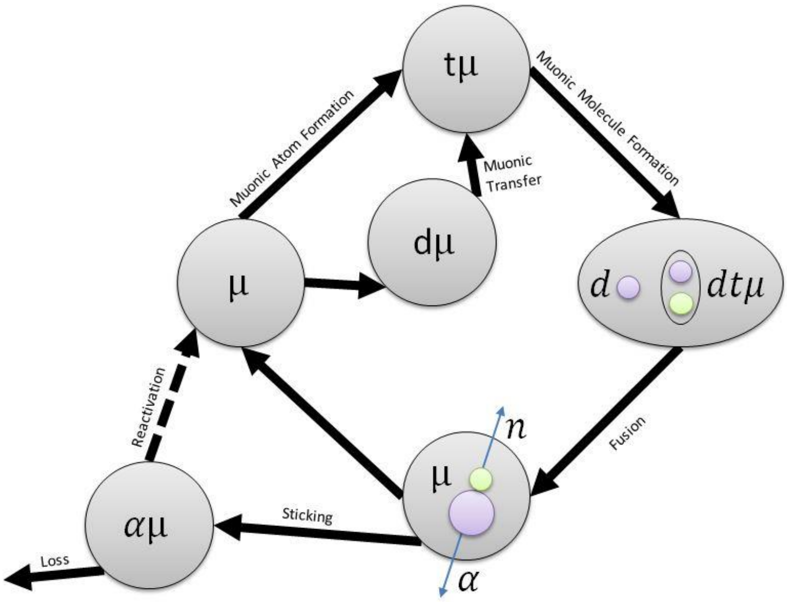

Figure 7: Schematic diagram of a muon-catalysed fusion cycle. Adapted from: (Kawamura, Ishida, Matsuzaki, Imao & Nagamine, 2010)

Unfortunately, the energy produced by fusion events facilitated by muons is not enough to counterbalance the energy required to produce muons, even though so many reactions can be catalysed (Eliezer, Tajima & Rosenbluth, 1987).

4.1.2.3 Molecular-nuclear transition Li-6D → Be-8 search with a pared $\Delta E - E$ microscope

The probability for spontaneous molecular-nuclear transitions can be represented in the form of Equation 22[6].

$$W(s^{-1}) = \omega(E_1)e^{-0.6\pi\eta(E_2)} \cdot Q \qquad \{22\}$$

In Equation 22, $\omega(E_1)$ is the frequency in which nuclei in a two-atom molecule approach the Coulomb barrier, Q is the overlap integral and η is the Sommerfeld parameter.

Belyaev et al. (2006) recorded transitions when double coincidences were noticed, since the unstable Be-8 decays into two He nuclei each with an energy of 11.2 MeV. Originally, experiments in the study by Belyaev et al. (2006) yielded several events per day and, therefore, background events needed to be determined and eliminated. This was done by producing specific ionisation loss (dE/dx) detectors, and a thin layer of Li-6D was deposited onto a Mylar film that was placed between two planar Si-charged semi-conductor detectors. A thickness of 9 μm of fine Li-6D crystalline powder was used. Additional detectors were used to exclude background events produced by cosmic ray particles.

---

[6] The reason for this is described in section 4.1.2.4.

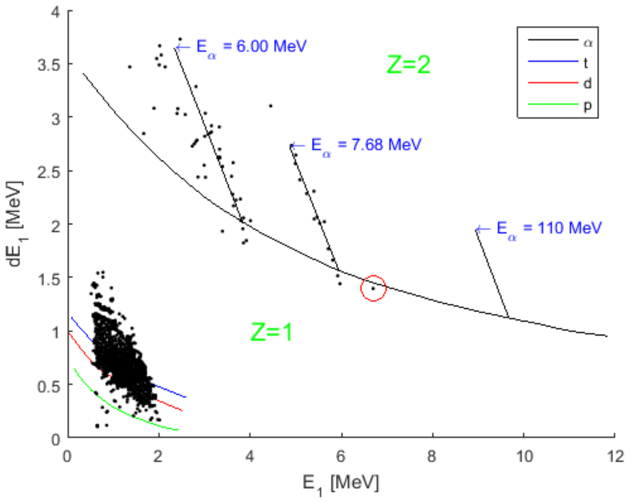

Figure 8: Two-dimensional spectrum for the measurements. Adapted from: (Belyaev et al., 2006)

The results of Belyaev et al. (2006) are presented in Figure 8, where dots represent particles being detected and lines with labels indicate particle energies. Figure 8 indicates that only one positive event (where the particle was an α particle and had the expected energy) was noticed. Most of the observed events are due to traces of radon gas in the measuring chamber, emanating from the construction matter of the vacuum chamber where the experiment was conducted. Analysis indicated that some other events were caused by the Li-6+n$_{\text{thermal}}$ reaction[7].

The half-life period was thus calculated as follows in Equation 23 (Belyaev et al., 2006):

$$T_{\frac{1}{2}} \geq \ln(2) \cdot \frac{\varepsilon A m}{\frac{dN}{dT} M} = 2.4 \times 10^{19}\ [y] \qquad \{23\}$$

In Equation 23, A is Avogadro's number, ε is the detector efficiency, m is the mass of the Li-6D sample, M is the molecular mass of the Li-6D compound and $\frac{dN}{dT}$ is the counting rate. The calculated value is thus the lower limit for the lifetime.

Belyaev et al. (2006) concluded that some factors must be slowing the fusion process and that more detailed theory of the effect is needed. It was recommended that more sensitive experiments be conducted.

4.1.2.4 Fusion reactions in molecules via nuclear threshold resonances

The Li-6D → Be-8 reaction can decay into either n + Be-7, p + Li-7 or $\alpha + \alpha$.

To determine the transition probability, the model described in equations 22 to 32 is used.

Firstly, the resonant state, which is represented by ψ_{res}, is chosen as an outgoing Coulomb s-wave, shown in Equation 24 (Zettili, 2009).

$$\psi_{res(r)} = \frac{1}{N_{res}} \cdot \frac{e^{i\eta \ln(\kappa r)}}{r} \qquad \{24\}$$

---

[7] The thermal neutrons are produced by some of the equipment operating at the Joint Institute for Nuclear Research (JINR).

Equation 24 is a solution to the Schrödinger equation where κ is the wave number, *r* is the radius between the particles and η is defined in Equation 25 (Zettili, 2009).

$$\eta = Z_1 Z_2 \alpha \sqrt{\frac{\mu c^2}{2E}} \tag{25}$$

In Equation 25, Z_1 and Z_2 are charge numbers, α is the fine structure constant, μ is the reduced mass of the system, *C* is the speed of light and *E* is relative energy of outgoing particles as described in Equation 26 (Zettili, 2009).

$$E = \frac{k^2}{2\mu} \tag{26}$$

The molecular state is representing the motion of the D and Li-6 under the influence of an attractive potential, but with a strong Coulomb repulsion at the origin. This is chosen as the product of a regular Coulomb solution and an exponentially decreasing function that is associated with the size of the molecule shown in Equation 27.

$$\psi_{mol}(r) = \frac{1}{N_{mol}} \cdot \frac{F_0(\kappa, r)}{r} \cdot e^{-\kappa r} \tag{27}$$

The transition amplitude is thus given by the overlap of the two functions in Equation 28.

$$I = \int \psi_{res}(r) \psi_{mol}(r) \cdot d^3 r \tag{28}$$

For the sake of calculating the overlap, the representation shown in Equation 29 is used for the regular Coulomb functions.

$$F_0(\kappa, r) = C_0(\eta) r e^{ir} M(1 - i\eta, 2, 2ir), \tag{29}$$

where

$$M(a, b, z) = \frac{\Gamma(b)}{\Gamma(a)\Gamma(b-a)} \cdot \int_0^1 e^{zt} t^{a-1} (1-t)^{b-a-1} \cdot dt, \tag{30}$$

and

$$C_0(\eta) = \frac{e^{-\frac{\pi\eta}{2}} \Gamma(1 + i\eta)}{\Gamma(2)}. \tag{31}$$

Using equations 28 to 31, the space integration can be completed analytically. All distances are considered to yield the solution shown by Equation 32.

$$I \propto 4\pi C_0(\eta) \cdot \frac{\Gamma(2)\Gamma(2+i\eta)}{|\Gamma(1+i\eta)|^2} \cdot \int_0^1 \left(\frac{1-t}{t}\right)^{i\eta} \times \frac{dt}{\left(1 - i(2t-1)\right)^{2+i\eta}} \tag{32}$$

Near the threshold energy, $\eta \gg 1$, and is thus evaluated using the saddle-point method. The saddle point lies at $t_1 = 1 + \frac{1}{2}\left(\sqrt{\sqrt{2}+1} + i\sqrt{\sqrt{2}-1}\right)$. The leading term of the system shown by Equation 32 can thus be reduced to Equation 33.

$$I \propto \frac{C_0(\eta)}{\kappa} \cdot \frac{\Gamma(2+i\eta)}{|\Gamma(1+i\eta)|^2} \cdot \frac{e^{0.614\pi\eta}}{\sqrt{\eta}} \cdot \left(A + Li\left(\frac{1}{\eta}\right)\right) \tag{33}$$

In Equation 33, A is an η-independent constant. A manipulation of Equation 33 yields Equation 34 (Belyaev et al., 1996b).

$$I \propto \eta^{\frac{3}{2}} e^{\left(0.614-\frac{1}{2}\right)\pi\eta} \qquad \{34\}$$

This state indicates that, unlike the usual Coulomb barrier penetration factor that decreases for an increasing η, the factor now increases as η increases. The resulting conclusion is that the resonant state is essentially contributed to by the overlap integral from intermediate and large distance regions.

4.1.2.5 Induced molecular-nuclear transitions in water and some other molecules

A condition of molecular-nuclear transitions is that energy values for the initial molecular state and the final resonant state of the atomic nucleus must be identical. This is completely a matter of chance. However, work shown in Belyaev and Miller (2010) postulates that stimulation of these reactions by external radiation seems attractive. There is uncertainty in the widths of the nuclear resonances in the order of a few keV, but it is reasonable to assume that the molecular level is several keV higher than that of the resonant system. The molecular-nuclear complex can thus be considered a two-level system that may be considered analogous to a two-level quantum system as considered in optics proposed by (Belyaev, Motovilov & Sandhas, 1996b).

Consider the gain factor K as in Equation 35, where the gain factor is used to describe the proportionality constant between the energy that goes into the system and the energy that is produced i.e. $E_{in} \times K = E_{out}$.

$$K = e^{gL} \qquad \{35\}$$

In Equation 35, L is the linear size of the hypothetical system being considered and g is described by Equation 36 (Belyaev & Miller, 2010).

$$g = N \cdot \lambda^2 R \qquad \{36\}$$

For Equation 36, N is the Lochmidt constant ($2.68 \times 10^{-19} cm$), λ is the wavelength of the incident radiation and R is described in Equation 37 (Belyaev & Miller, 2010).

$$R = \frac{W_\gamma}{4(W_\gamma + \sum W_i)} \qquad \{37\}$$

In Equation 37, W_γ represents the induced radiation probability and $\sum W_i$ is the sum of all possible channels of decay. Belyaev and Miller (2011) indicate that $R \approx \frac{1}{8}$.

The defining probability with a multipolarity of 1 can thus be written as shown in Equation 38 (Belyaev & Miller, 2010).

$$W_\gamma = \int_0^{J_1} {}^{J_1}_{0}\Psi_{res}(r) r^{l} \, {}^{J_2}_{0}\Psi_{mol}(r) r^2 \cdot dr \, , l = |J_1 - J_2|, \qquad \{38\}$$

where ${}^{J_1}_{0}\Psi_{res}(r)$ and ${}^{J_2}_{0}\Psi_{mol}(r)$ are wave functions, as described in section 4.1.2.4, with angular moments of J_1 and J_2 respectively. As long as the molecular state energy exceeds that of the resonant state within the resonance width, the integrant of the wave functions is large due to overlap.

Assuming the energy range as described by Equation 39, g can be determined as shown in Equation 40.

$$\Delta E = \frac{c}{2\pi\lambda} = 1\ [keV] \qquad \{39\}$$

$$g = 2.68R \cdot 10^{3}[cm^{-1}] \qquad \{40\}$$

This results in a gain factor *K,* as indicated in Figure 9:

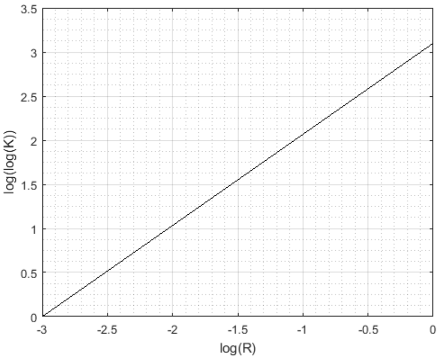

Figure 9: Gain factor versus ratio R. Adapted from: (Belyaev & Miller, 2011)

4.1.2.6 Fusion in LiD crystals

LiD crystals are isometric hexoctahedral crystals that have a perfect cubic formation and a lattice constant[8] of 4.0684Å (Staritzky & Walker, 1956). In this crystal formation, the Li and D atom pair remains in close proximity for an extended period and this prolonged exposure increases the probability for fusion to occur. When in crystal form, the atoms can be considered to have a kinetic energy of 0 relative to one another and this can be changed by bombarding the lattice with photons. These photons will impart energy to the atoms in the lattice, thus raising the relative kinetic energy between the atoms. The result is that the atoms, which are in close proximity, increase the probability for quantum tunnelling to occur. These atoms are also excited, which raises their energy, thus reducing the remaining energy required to overcome the Coulomb repulsive force, also increasing the probability of fusion.

4.1.2.7 Conclusions

There is strong evidence to suggest that molecular-nuclear transitions can occur for Li-6D and that electromagnetic radiation should be able to stimulate these reactions. This can thus be considered a process where energy is amplified. For the Li-6D case, several keV photons could be sufficient to induce the fusion and thus produce two 11.2 MeV α particles (V. Belyaev & Miller, 2011).

4.2 Track detectors

4.2.1 Introduction

The fusion reactions, as indicated in section 4.1.2.3, can be observed in various manners. Nevertheless, a bulk-processing methodology was selected since the experiment requires a

---

[8] The lattice constant refers to the distance between nuclei in the crystal lattice. Since LiD crystals are cubic, this distance applies to all three-dimensional directions.

protracted exposure time. CR-39 will be used and section 4.2.2 explores this and similar detectors and techniques.

4.2.2 Literature review

4.2.2.1 Track formation

Tracks are formed in certain substances due to the damage caused by ionised particles on the matrix of the substance. The first law of thermodynamics dictates that the damage done to the matrix should be representative of the energy lost by the ion. This can be represented by Equation 41 (Fleischer, Price & Walker, 1975).

$$n\int_0^\infty \Delta E(r) 2\pi r \cdot dr \tag{41}$$

Near the ion path, the ion excites electrons in the lattice to higher energy levels. This causes long chains in molecules to break and produce free radicals. Some of these electrons may even be loosened from their atoms and ejected. This leads to the creation of positive charge centres due to the absence of electrons. The released electron also yields an X-ray and both of these cause damage to the lattice at a greater distance from the original ion path.

The effective radius of a track produced in this manner is represented by Equation 42 (Fleischer et al., 1975).

$$r_{eff} = \left(\frac{l\Omega}{n\pi k}\right)^{\frac{1}{2}} \tag{42}$$

For Equation 38, Ω represents the conductance of the material lattice, *n* is the number of pores in the lattice, *r* is the pore radius, *l* is the depth of the pore and *k* is the conductivity of the etchant.

The charge of the ion moving through the lattice can be empirically calculated using Equation 43 (Fleischer et al., 1975).

$$Z^* = Z(1 - e^{-130\frac{\beta}{Z^{\frac{2}{3}}}}) \tag{43}$$

In Equation 43, Z^* represents the positive net charge of the indent particle, Z is the atomic number of the indent particle and β is the speed of the indent particle relative to the speed of light.

When considering that the dynamics of the ion velocity collisions is far greater than that of the orbital electron velocity, the orbital electron velocity may be disregarded.

Figure 10 illustrates the effects in a crystal structure and polymer when a particle traverses it.

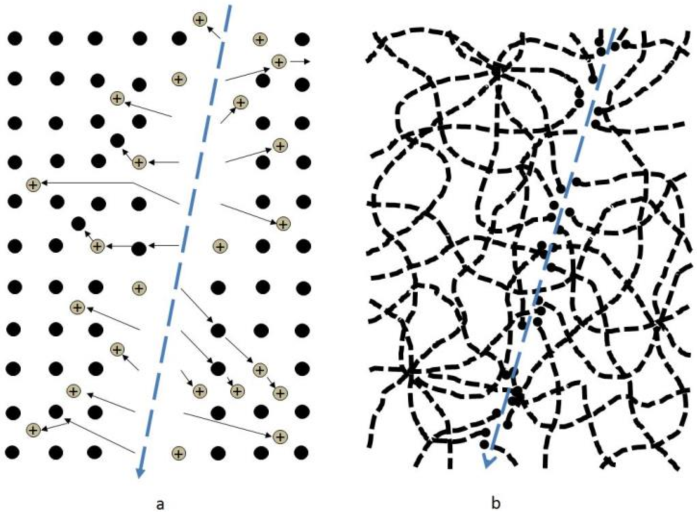

Figure 10: The atomic character of a particle in (a) a crystal; and (b) a polymer. Adapted from: (Fleischer et al., 1975)

In a crystal, the damage consists of a continuous disorder composed of vacant lattice sites and of interstitial ions or atoms. New chain ends and other chemically reactive sites are formed in the polymer.

At low energies (<50 keV) and ions with high atomic masses (>50 amu), the dominant mode of energy loss can be considered to occur through atomic collisions. The imparted kinetic energy limit is confined to $\frac{2mv^2}{1-\beta^2}$ (Fleischer et al., 1975) and the damage mode is due to displaced atoms and vacancies. The energy deposited per unit length is $\frac{dE}{dx}$. However, consideration for this model is inconsistent due to the release of delta rays. These rays are released when the incident particle knocks a nucleus out of its position in the lattice, which frees the electrons around that atom from orbit and releases them into the matrix.

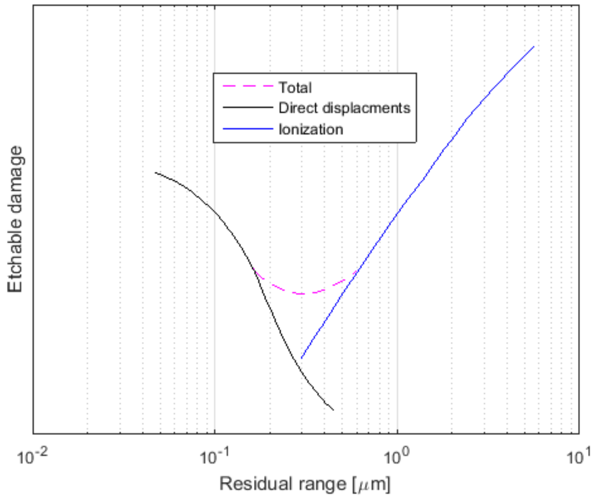

Figure 11: Etchable damage from stopping a heavy nucleus partitioned into the effects of ionisation and of atomic displacement at low energies. Adapted from: (Fleischer et al., 1975)

Figure 11 indicates the type of damage done by an incident particle on the detector material matrix. The y axis is unitless and indicates the scale of the damage in the matrix. The black line indicates damage caused by direct displacements of the incident particle. The brown line is further damage in the detector matrix due to the repulsion of ionised particles in the matrix, and the yellow line represents the combination of these two types of damage. The x axis indicates the distance from the original impact of the incident particle. The conclusion is that, close to the original impact, the main form of damage is through direct displacement, whereas after about 0.3 um, the main driving force of damage in the matrix is ionisation.

Many other mechanisms are considered, but the main mode of energy loss for ions with greater energies and lower atomic masses is described by the ion explosion spike demonstrated in Figure 12. This model is based on the main ion ionising atoms in the lattice leaving behind an array of electrostatically unstable adjacent ions. Here the material fails locally if the Coulomb repulsive force is greater than that of localised yielding. The Coulomb repulsive force can be represented by Equation 44 (Fleischer et al., 1975).

$$\sigma_e = \frac{n^2 e^2}{\epsilon a_o^4} \qquad \{44\}$$

For Equation 44, σ_e represents the force per unit area, ϵ is the dielectric constant for the material and a_a is atomic spacing within the material matrix. The yielding criterion is shown in Equation 45 (Fleischer et al., 1975).

$$\sigma_e > \frac{Y}{10}, \qquad \{45\}$$

where Y is Young's modulus in Equation 45. This does not necessarily occur on every plane. However, for most detectors that use plastic material for tracking the damage, one to three ionisations per 20 atomic planes is sufficient for detection after chemical etching.

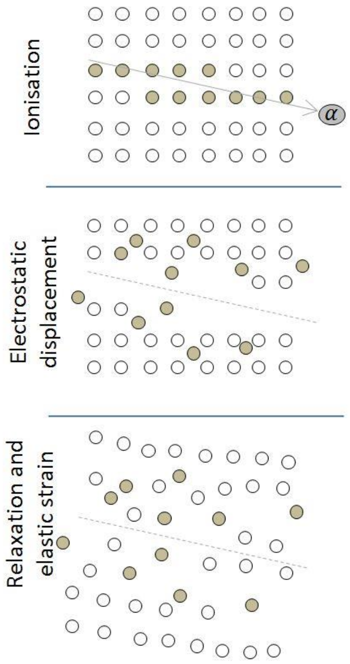

Figure 12: The ion explosion spike mechanism for track formation in inorganic solids. Adapted from: (Fleischer et al., 1975)

As shown in Figure 12, the original ionisation left by the passage of a charged particle (top) is unstable and ejects ions into the solid, which creates vacancies and interstitials (middle). Later, the stressed region relaxes elastically (bottom), which strains the undamaged matrix.

4.2.2.2 Etching

The formed tracks are very small and would require extremely accurate equipment to evaluate it. The tracks are etched because it increases the size of the damage in the lattice by chemically removing material from the lattice. Tracks become visible when chemicals rapidly and preferentially attack damaged material. This means that etched holes are formed due to the removal of the damaged lattice.

During etching, two types of processes should be considered. The first is the chemical dissolution along the particle track, represented by v_T. The second is the general attack on the etched surface of the material represented by v_G where both v_T and v_G are rates of material removal in terms of depth of material removed per unit time. When the etching time is short, it can be assumed that both v_T and v_G are constant. Equation 46 can thus be generated. This is graphically represented in Figure 13.

$$l = (v_t - v_G)t \tag{46}$$

In Equation 46, l represents the length of the track after etching, and t represents the period that the detector was etched for. The diameter of the track can be determined using Equation 47 (Fleischer et al., 1975).

$$D = 2v_G t\sqrt{\frac{v_t - v_G}{v_t + v_G}} \tag{47}$$

In Equation 47, *D* is the diameter of the etched track and all other variables have their aforementioned meanings. Finally, Equation 48 shows the time limit for which these conditions are applicable (Fleischer et al., 1975) to be:

$$t < \left(\frac{R}{v_G}\right) \cdot \left(1 + \frac{(1 - \sin(\theta)) \cdot \left(\cos\left(\frac{\theta}{2}\right) + \sin\left(\frac{\theta}{2}\right)\right)}{\left(\cos\left(\frac{\theta}{2}\right) - \sin\left(\frac{\theta}{2}\right)\right) \cdot \cos(\theta)}\right) \tag{48}$$

In Equation 48, *R* is the distance between the end of the particle track and the original detector surface, and θ is half of the angle of the etched track. The decreasing velocity also rounds the tracks outwards for short tracks. In other words, if the track depth is longer than the depth of the etched track (R>l) for a specific track, then the etched track will have a sharp edge, whereas the tip of the etched track will be round if l>R, as shown in Figure 16.

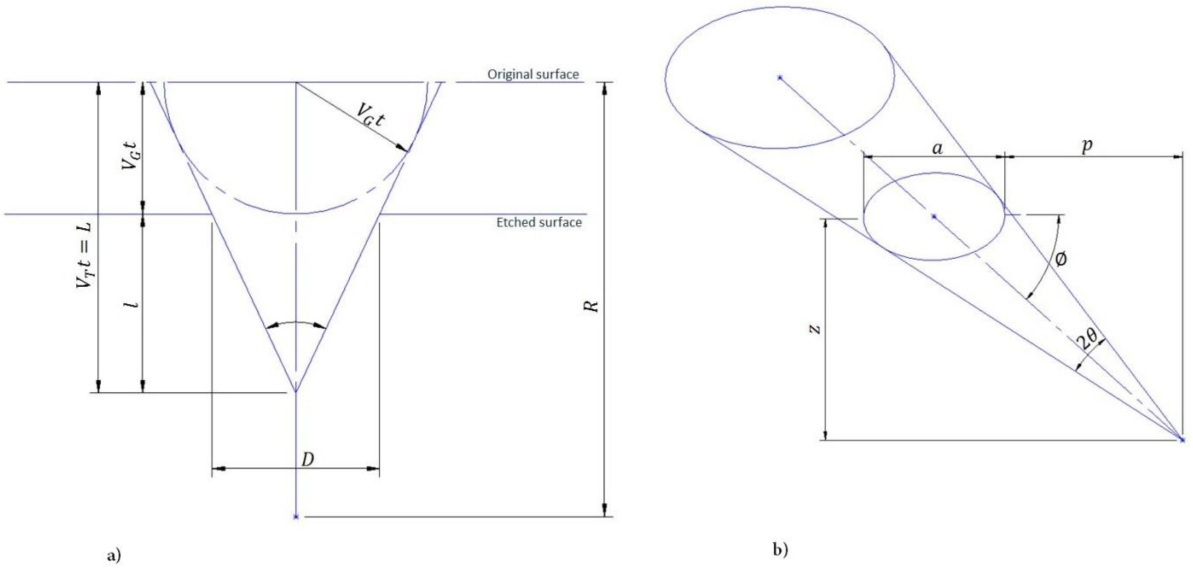

Figure 13: Track geometry with v_T and v_G constant. Adapted from: (Fleischer et al., 1975)

In Figure 13, a) is the geometry of an etched track for a vertically incident particle, and b) is the etched track geometry for an incident particle, where ϕ is the dip angle. In both of these cases R>l.

Since the chemical used removes material, not only from the damaged matrix around the track, but also from the bulk of the detector, it is important to note that if the material is etched for too long, there is a possibility that the track would no longer be visible. This would be due to bulk etching having removed all the material around the track. The efficiency of a certain etching process η is represented by Equation 49.

$$\eta = \frac{tracks\ etched}{tracks\ made} \qquad \{49\}$$

In order to visualise how tracks are registered or lost, Figure 14 is provided.

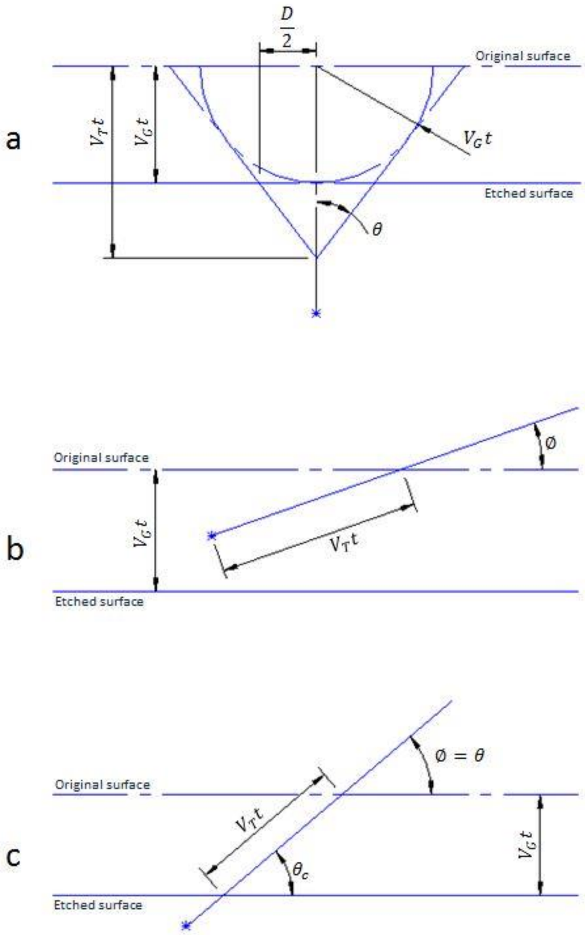

Figure 14: Track registration geometry. Adapted from: (Fleischer et al., 1975)

As indicated in Figure 14a, track pit shape is determined by the general rate of attack v_G and the preferential attack rate v_T along the damage trail.

In Figure 14b, for angle incidence ϕ less than $\sin^{-1}\left(\frac{v_g}{v_T}\right)$, the surface is removed at a greater rate than the normal component of v_T , and therefore no track is observed. In Figure 14c, the critical angle $\theta_c = \sin^{-1}\left(\frac{v_g}{v_T}\right)$ above which tracks are registered.

The etching efficiency is not exactly the same for all materials. Table 1 can be used to determine efficiencies.

Table 1: Etching efficiencies for short etching times (Fleischer et al., 1975)

Case		**Relation for η**
i	Tracks random through volume; θ constant along length of track	$\eta = \cos^2\theta$
ii	Tracks random in orientation from external thin source	$\eta = 1 - \sin\theta$
iii	Tracks random through volume; θ decreases linearly to zero along particle range	$\eta = 1 - \sin\theta$
iv	Tracks random through volume; θ an arbitrary function of R	Numerical calculation required

Prolonged etching under the right conditions may remove more pits. This means that small features that were not perceptible originally are enlarged. It also allows for tracks that began and ended beneath the original material surface to be encountered.

4.2.2.2.1 External effects

Beyond the solubility of the track detector in the etching substance, a few other environmental conditions may affect the etching process, such as the following:

- The heating of the track detector before etching will reduce the size of tracks and even remove some through the process of creep or annealing.
- Mechanical effects play a role, such as the formation of dislocations in the material.
- Chemical pre-treatment of the material may alter etching rates.
- Electrical effects should not be neglected. Since the ion explosion model is based on the removal of electrons, a current may replace electrons and thus repair or prevent the damage to the matrix.
- Photochemical and irradiation effects also play a role. The irradiation of a detector may for example increase the v_T of an etch.

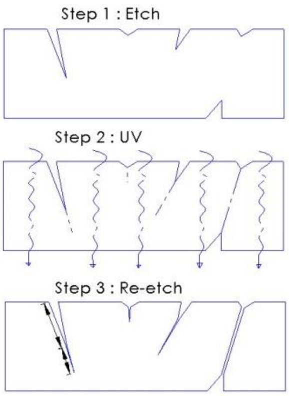

Figure 15: Particle identification by measuring etch pit lengths L at residual ranges R. Adapted from: (Fleischer et al., 1975)

In Figure 15 the use of ultraviolet (UV) radiation in developing tracks is depicted. If a particle stops in a single sheet, both L and R can be measured at the same time if the detector is a plastic where v_T can be increased by UV radiation. This three-stage process requires an initial etch, UV exposure and a short final etch of the same sheet. Thus, the detectors in Step 1 are etched under normal conditions, but R>l and thus the UV radiation in Step 2 articulates the damage to the matrix along the entire track length. In Step 3, re-etching allows for the removal of material of an additional length of l', where $l' + l = R$.

4.2.2.2.2 Techniques

Determining how a material should be etched is a matter of trial and error. This is due to the fact that many environmental factors do not influence all materials to exactly the same extent. The methodology is simply to begin with a sample that is known to have tracks on its surface. To etch this material, a chemical reagent that is known to dissolve the sample material should be selected, preferably at a constant rate. The temperature and concentration of this reagent can be varied to control the attack rate. This method is not only used for track studies, but also for metallurgical studies. A useful consideration is thus to cross-reference with such works, since if a dislocation will show, then so too will a track. Finally, surfaces should be smooth on an optical scale.

4.2.2.3 Materials

4.2.2.3.1 Generally

The main concern when considering a material for track detection purposes is the mobility of positive current carriers[9]. If these carriers are very mobile, the positive charges created by the ion moving through the matrix may diffuse away from the main track, thus failing to increase the localised strain.

Table 2: Relation of track formation to electrical resistivity (Fleischer et al., 1975)

Minerals		**Resistivity range** $\left[\frac{\Omega}{cm}\right]$
I	Track-forming insulators: silicate minerals Alkali halides Insulating glasses Polymers	$10^6 - 10^{20}$
	Poor insulators: MoS_2	3000–25000
	Semiconductors: V_2O_5 glass	2000–20000
II	Non-track-forming semiconductors: Germanium Silicon	10–2000
	Metals: Aluminium Copper Gold Platinum Tungsten Zinc	$10^{-6} - 10^{-4}$

The secondary restriction is of course that the electron mobility also needs to be low, so that the ejected electrons are not replaced, thus neutralising the ions that may be formed.

4.2.2.3.2 CR-39

The chemical composition for the CR-39 track detector is $C_{12}H_{18}O_7$ and it has a density of about 1.3 g/cm^3 (Roussetski, 2006).

4.2.2.3.2.1 Etching

The etching process for this material is for it to be placed in an NaOH solution at about 70 °C. The concentration is determined by the required etching rate. The track detector should be left in the solution for several hours before being removed, depending on the energy of interest. For this track detector, the efficiency can be represented by Equation 50 (Roussetski, 2006), where all the variables remain the same, as indicated in section 4.2.2.2.

$$\eta = 0.5(1 - \sin(\theta_c)) \qquad \{50\}$$

---

[9] Similar to "holes" in semiconductors that allow current to pass through them.

4.2.2.4 Detection

Even though the tracks that have been made by the ions are now etched, the data has yet to be captured through some type of methodology. One of the most common means of track detection is through a microscope. However, certain steps can be taken to increase the sensitivity of track detection. This may be achieved by enhancing the track contrast. The contrast can be improved through interference contrast microscopy by filling the etched tracks with opaque substances or flame polishing the detector surfaces. Automated and integrative systems can discover tracks. There are several ways to enlarge tracks to make them more visible.

Table 3: Track enlargement methods (Fleischer et al., 1975)

Technique	**Track density where useful**	**Limitations or special features**
Etch aluminium-backed plastic from front; transmits light where metal is removed.	$< 100\,\frac{tracks}{cm^2}$	Oblique tracks require longer etching time; non-uniform hole sizes.
Apply potential: a) Observe spark location. b) Scan enlarged holes.	a) $< 10\,\frac{tracks}{cm^2}$ b) $< 10^4\,\frac{tracks}{cm^2}$	High voltage can enlarge holes, including ones that were not quite open.
Apply potential; scan holes evaporated in thin aluminium coating by discharge.	$< 3\,000\,\frac{tracks}{cm^2}$	This technique alters etched tracks.
Press dye through holes onto filter paper.	$< 10\,\frac{tracks}{cm^2}$	A separate sheet shows track locations.
Blow NH_3 through holes, thus staining sensitive paper.	$< 1\,\frac{track}{cm^2}$	This technique gives separate sheet showing track location and a rapid scanning rate ($10^3\,\frac{cm^2}{min}$).
Measure resistance of track etched across membrane in electrolyte.	1 to 10 tracks in total	This technique can give etching rates v_T and v_G.
Enlarge images using slide projector.	10^4 to 5×10^6 tracks	Tracks are individually counted on a projection screen.
Measure UV light transmission in Mylar, because it is very absorbent.	10^3 to 10^7 tracks	This technique detects light when the hole is not quite through the sheet.

Another novel way to discover the location of tracks is through the spark-scanning technique. This method involves placing the detector on a dielectric plate, covering it with aluminised Mylar and applying a voltage to this set-up. Sparks will then jump through the perforations in the detector, which leaves imprints on the Mylar that may be examined.

4.2.2.5 *Identification*

The final step is to identify the ions that have left the tracks. This is not only an important step in determining the relevance of an ion track, but also the state of the ion itself.
All detection techniques require an original calibration with known ions in order to validate results.

Etch rate can be compared to residual range in order to calculate ion properties. The goal of this method is to determine a single relation between these two variables in order to identify the ion. Equation 51 shows a definition for the track etching rate v_t where *B* and ξ are empirical (Fleischer et al., 1975).

$$v_t = BJ^{\xi} \tag{51}$$

For Equation 51, *J* is described by Fleischer et al. (1975) using Equation 52.

$$J = a\left(\frac{Z^{*2}}{\beta^2}\right) \cdot (\ln(\beta^2\gamma^2) + k - \beta^2) \tag{52}$$

Equation 52 is then related to time through Equation 53 (Fleischer et al., 1975).

$$t = \int_{R_o}^{R_o+L} dR\, [v_t(J)]^{-1} \tag{53}$$

In Equation 53, *R* is the track depth. The method described in equations 51 to 53 varies in efficacy, depending on the energy of the ion.

When the energy is 10<E<1 000 MeV, the relation is well approximated by power laws. However, for 0.1<E<10 MeV, a scanning electron microscope (SEM) is needed to make observations and there is no analytical relationship between *J* and *R*.

The properties of the track profile can be studied to identify the incident ion, but this requires very accurate observations.

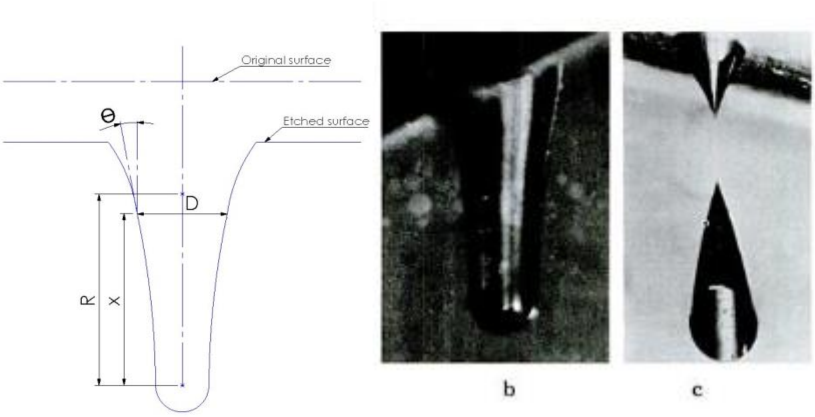

Figure 16: Track profile method of particle identification (Fleischer et al., 1975)

In Figure 16 the images represent the following:

a) Representation of an etched track (transforming $\theta(x)$ into $v_T(R)$)
b) Heavy cosmic ray being stopped
c) Heavy cosmic ray passing through an electrophoresis cell made of Lexan and flown on one of the Apollo missions

The measurement of the etch pit diameter may also be used to obtain ion properties. This method does not require an SEM, but it is less accurate than the previous methods mentioned.

4.2.3 Conclusions

The use of CR-39 is convenient, since it is easily inserted into most experimental set-ups and does not require any power or control systems to be used as a detector. Conclusions about specific methodologies are drawn in Appendix A. However, the most relevant conclusion is that each batch of etched detectors should have a calibration method, since the process depends on many factors that can easily vary.

4.3 X-rays

4.3.1 Introduction

A controlled method of delivering the required energy to the Li-6D crystals is in the form of X-rays. In order to determine the power increase in the process, the input power must first be thoroughly investigated. The processes of X-ray production are considered for the selection of an appropriate source and the X-ray spectra involved are investigated so that a thorough analysis of the theoretical energy throughout the sample can be evaluated.

4.3.2 Literature review

4.3.2.1 Basics

X-rays are a form of electromagnetic radiation. Specifically, they tend to have a wavelength of 0.01 to 10 nm. Hard X-rays have energies greater than 10 keV and are generally used for imaging purposes.

4.3.2.2 Producing X-rays

X-rays are most commonly produced by converting electrical energy into X-rays and heat. The heat is an undesirable, but inevitable by-product. Thus, X-ray tubes are designed to maximise X-ray production and dissipate heat as rapidly as possible.

Electrons are accelerated in a tube by applying a potential difference between the cathode and the anode in a vacuum chamber. The electrons then accelerate and interact with the anode where they react with the material, which produces both heat and electromagnetic waves, as shown in Figure 17. The anode design is of integral importance. However, the material involved is not the only important factor when considering the anode design. Most anodes are shaped like discs and are rotated at relatively high speeds. This is done for heat dissipation.

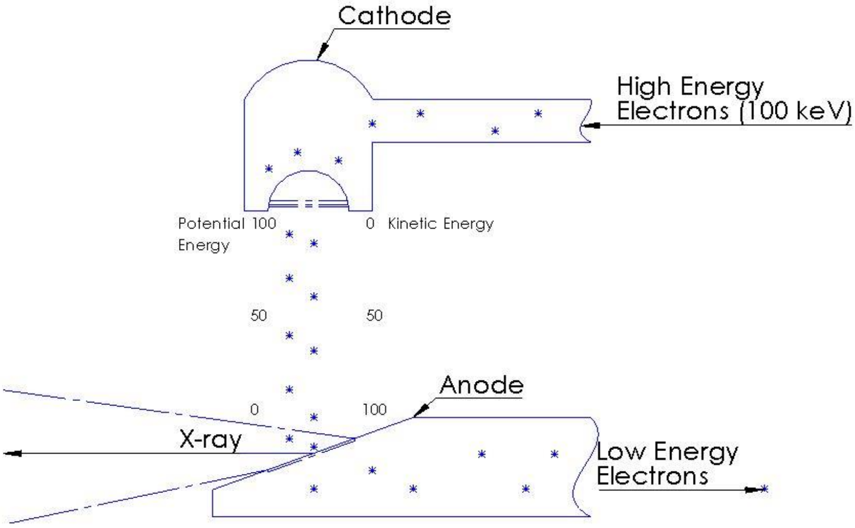

Figure 17: Energy exchange within an X-ray tube. Adapted from: (Sprawls, 1995)

In Figure 17 the percentage of the type of energy is indicated. It is shown that all the electron energy is in the form of potential energy at the top (near the cathode) and none is in the form of kinetic energy. The bottom 0% (anode) of the electron energy is in the form of potential energy and 100% is in the form of kinetic energy.

The entire anode is not a target, therefore the area where the radiation is produced is known as the focal spot. The dimensions of the focal spot are determined by the incoming electron beam. Small focal spots produce less blurring and are thus more generally used for imaging purposes, whereas large focal spots have greater heat dissipating capacity.

Three main electrical quantities can be adjusted to control X-ray production. These are electrical potential, electrical current and exposure time. The electron energy or potential can be varied to determine the energy range of the X-rays.

In the conversion to X-rays, the types of electron energy involved, namely potential, kinetic and binding energy, should be considered. Potential energy is carried by the electrons at the cathode, and is determined by the voltage. For every 1 V applied, each electron carries 1 eV of potential energy. Once emitted from the cathode, the electrons experiencing the electrical force pulling them towards the anode are accelerated. The increase in velocity leads to an increase in kinetic energy at the cost of potential energy. By the time the electron reaches the anode, all the potential energy will have been converted to kinetic energy. Equation 54 shows that KE at the anode is equal to the voltage applied between the anode and the cathode, where V is the applied potential energy measured in eV.

$$E_{kin} = V \tag{54}$$

Equation 56 is used to determine the velocity of the electrons at the anode.

$$E_{kin} = m_o c^2 \left(\frac{1}{\sqrt{1 - \frac{v^2}{c^2}}} - 1 \right) \tag{55}$$

$$\therefore \sqrt{1-\frac{1}{\left(\frac{V}{m_0c^2}+1\right)^2}}\cdot c = \sqrt{1-\frac{1}{\left(\frac{V}{0.511\times10^6}+1\right)^2}}\cdot c = v \tag{56}$$

Considering equations 54 to 56, it is clear, for example, that the electrons move at 0.548 times the speed of light with a potential difference of 100 kV.

The electrons then interact with the individual atoms of the anode material. These reactions produce either characteristic or Bremsstrahlung X-ray photons or heat. Characteristic X-rays are produced when the incoming electrons manage to eject one of the electrons from one of the orbitals of the atoms of the anode material. Consequently, an electron occupying a higher orbital drops down to replace the void and releases a characteristic X-ray photon in the process. The energy of the characteristic X-rays can be accurately predicted using the Bohr model and this is used extensively in spectrometry, since the target material composition may be determined by measuring the characteristic X-rays produced.

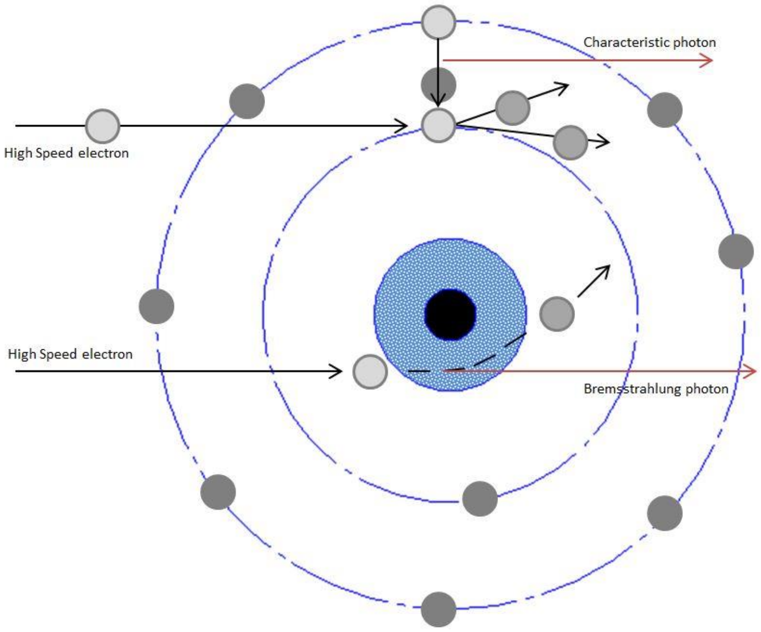

Figure 18: Electron-atomic interactions that produce X-ray photons. Adapted from: (Sprawls, 1995)

On the other hand, Bremsstrahlung X-rays are produced when the electrons pass through the electron cloud close enough to the nucleus that the Coulomb attractive force acts and deflects the electron. The electron then loses speed and follows another path. Due to conservation laws, a photon that carries the lost energy is produced. The braking force and angle thus lead to a continuous, rather than a specific Bremsstrahlung radiation spectrum, as is the case with characteristic radiation, since it is based on the electron’s proximity to the nucleus. This may vary widely for every electron that moves towards the anode.

Figure 18 graphically depicts how both types of X-rays are produced. The top electron collides with an electron that occupies one of the nucleus’s orbitals and ejects this electron. The result is that an electron drops down from a higher orbital to fill the vacant position and produces a characteristic X-ray in the process. The bottom electron passes close by the nucleus and because of the braking force of the nucleus, the electron's trajectory is changed and an X-ray is produced to compensate for this braking force.

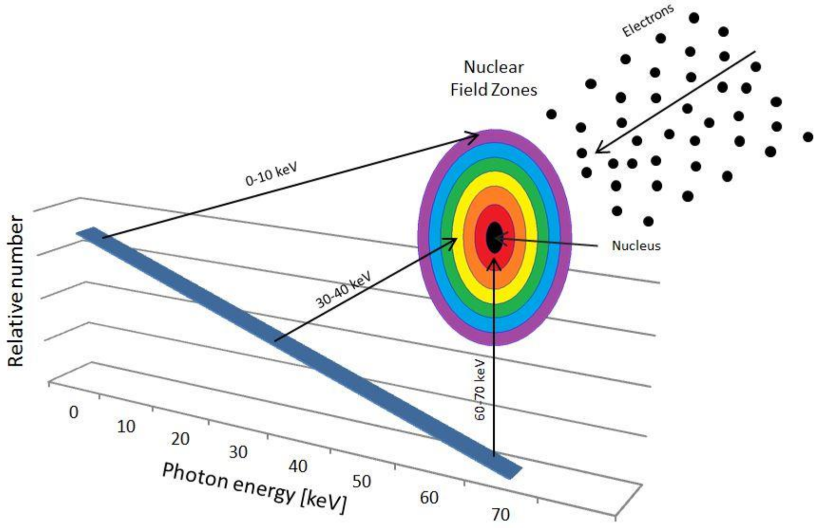

Figure 19: Bremsstrahlung production (simplified model). Adapted from: (Sprawls, 1995)

The Coulomb force decreases as the distance that the electron passes from the nucleus increases. The maximum theoretical energy an X-ray can have is equivalent to the kinetic energy of the electron, considering the case where the electron experiences a total braking force. However, this will not happen, so the highest X-ray energy is just below that of the potential applied to the X-ray tube. However, very few electrons pass this close to the nucleus, since the target is extremely small. Figure 19 depicts why the Bremsstrahlung spectrum can be described by Equation 53. The circumference of concentric circles around the nucleus increases as the distance from the nucleus increases, which indicates that ever more electrons will experience a reduced braking force.

The end result is that the direct emission spectrum represents Kramer's formula as a function of the energy at a specific point shown in Equation 57, where *C* is the Kramer's constant, Z is the atomic number of the target material and E_0 is the maximum energy of the electrons.

$$Count(E) = CZ(E_o - E) \qquad \{57\}$$

The energy emission by Bremsstrahlung derived in this manner can thus only be found in absolute terms by knowing the exact value of the constant *C*. A value for *C* as provided by Unsworth and Greening (1970) is C = 2.76×10^{-6}.

The produced X-rays then exit the tube and travel to their target or detector. Many of these X-rays are scattered and absorbed within the anode itself and all of them experience a level of attenuation. The result is that most of the X-rays have the energy of about a third of the maximum energy, as shown in Figure 20.

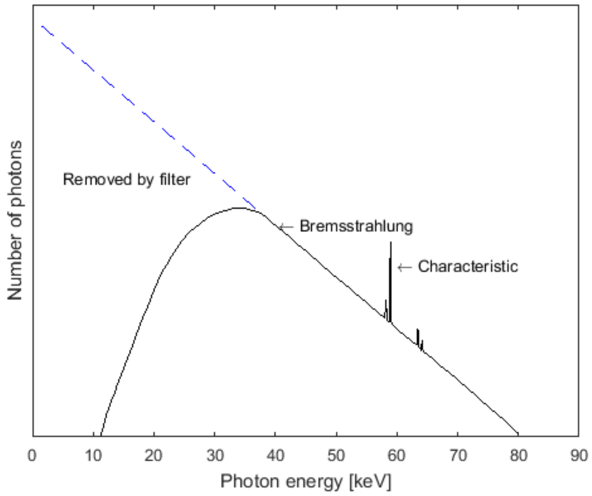

Figure 20: Typical operating spectrum. Adapted from: (Sprawls, 1995)

In Figure 20 the straight line as described by Kramer's formula can be seen as the original X-ray spectrum. Due to attenuation of X-rays by the anode and other materials that the X-rays must pass through, the low-energy X-rays are lost, as shown by the shaded region. The sharp peaks represent prominent characteristic X-rays that are entirely a function of the anode material. The y axis represents the number of photons produced (or detected) and the integral of the un-attenuated spectrum is equal to the total energy produced in the form of X-rays.

The production of characteristic radiation is however far more efficient than that of Bremsstrahlung. Consequently, as much as 25% of the total radiation energy could be in the form of characteristic X-rays, should the applied potential be high enough.

4.3.2.3 Efficiency

As indicated, most of the electrons that reach the anode are absorbed and their energy is simply used to produce heat. The efficiency is a product of the anode material and the applied potential. An approximation is shown in Equation 58 (Sprawls, 1995), where *V* is applied potential voltage and *Z* is the atomic number of the target nucleus.

$$\eta = VZ \cdot 1.1 \times 10^{-6} \qquad \{58\}$$

Atoms in a material with a higher atomic number pose as larger targets for the electron as described in Figure 19, and this produces more X-rays than an anode material with a lower atomic number. An increase in the potential difference also leads to a higher production of X-rays per unit heat due to an increase in efficiency according to Equation 58. For tungsten with a potential difference of 100 kV, the efficiency would thus be about 0.814%.

4.3.2.4 Attenuation

The attenuation of an X-ray beam is calculated in Equation 59 (Jackson & Hawkes, 1981):

$$\frac{I(t)}{I_0} = e^{-\mu t} \qquad \{59\}$$

In Equation 59, t represents the thickness of the material that the X-ray beam is passing through, μ is the linear attenuation coefficient, $I(t)$ is the intensity of the beam after it has been attenuated and I_0 is the original intensity of the beam.

Equation 59 assumes that no scattered X-rays reach the detector. The linear attenuation coefficient for electromagnetic radiation can be related to the mean free path τ in the target or the atomic cross-section σ_a, as shown in Equation 60 (Jackson & Hawkes, 1981).

$$\mu = \frac{1}{\tau} = n\sigma_a \qquad \{60\}$$

This leads to the mass attenuation coefficient $\frac{\mu}{\rho}$, as shown in Equation 61 (Jackson & Hawkes, 1981), where N_A is Avogadro's number.

$$\frac{\mu}{\rho} = \frac{N_A}{A} \cdot \sigma_a \qquad \{61\}$$

The XCOM database (NIST – Physical Measurement Laboratory, 2014) is used to produce attenuation coefficients throughout this paper.

4.3.2.5 Anode angle

For the X-rays that are produced to follow an exit path that is not coaxial to the incoming electron beam, the anode cannot be perpendicular to the beam. However, the angle of the anode plays a role in the generation of X-rays. Figure 21 shows the inbound electron beam with an intensity I_e striking the anode that is at an angle α, which results in an X-ray beam with intensity I_0.

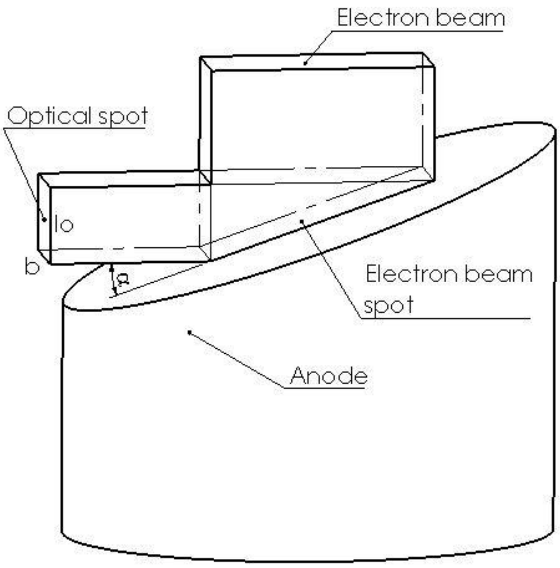

Figure 21: Electronic and optical focal spots for an anode at angle α. Adapted from: (Beckhoff, Kanngießer & Langhoff, 2006)

As a result of the angle of the anode, the intensity of the X-ray beam (if no attenuation is considered) can be described by Equation 62.

$$I_0 = I_e \sin\alpha \qquad \{62\}$$

Assuming that some of the electrons penetrate into the anode material before producing X-rays, it should also be considered that some of the X-rays produced below the surface are attenuated by the target material itself.

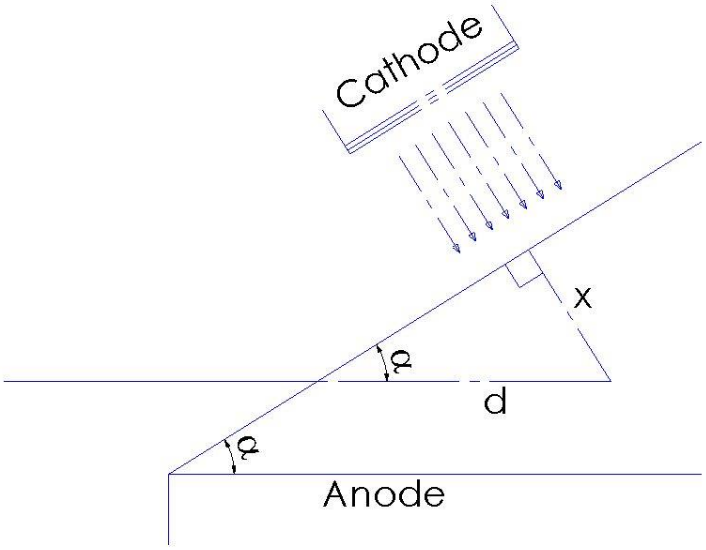

Figure 22: X-ray tube geometry and the relation between depth of X-ray production and X-ray photon path length through target. Adapted from: (Tucker, Barnes & Chakraborty, 1991)

Figure 22 indicates that, for a photon produced at a depth *x*, the distance travelled inside the target material can be shown by Equation 63, where:

$$d = \frac{x}{\sin(\alpha)}. \qquad \{63\}$$

The attenuation correction factor *F* that should be considered for this reason is described in Equation 64.

$$F = e^{-\frac{\mu x}{sin(\alpha)}} \qquad \{64\}$$

4.3.2.6 Target material selection

As indicated, the energy flux of the Bremsstrahlung is determined by the size of the field of the braking nucleus and thus by the atomic number of the target material atom. A higher nuclear charge results in more efficient X-ray production. Since the incoming electrons will produce a lot of energy on the surface of the anode material, the material's thermal properties are also of critical significance. Clearly, the material requires a high heat capacity[10] to survive, as well as good thermal conduction so that the heated area can be cooled effectively.

In order to evaluate materials, these factors are combined and the most appropriate material for a fixed anode maximises: $Z\theta_{max}\lambda$. Similarly, $Z\theta_{max} \cdot \sqrt{\rho\lambda c}$ should be maximised for a rotating anode.

---

[10] It is for this reason that Lead, Tin or Platinum is not considered.

Table 4: List of possible anode materials and the order of their suitability for both fixed and rotating anodes (Krestel, 1990)

Element	Atomic number Z	Permissible temperature θ_{max} at $1.33 \times 10^{-2}\ Pa$ in °C	Thermal conductivity $\lambda\left[\frac{W}{cm \cdot K}\right]$	Fixed anodes		Rotating anodes		
				$Z\theta_{max}\lambda$	Order of suitability	$\sqrt{\rho\lambda c}$	$Z\theta_{max} \cdot \sqrt{\rho\lambda c}$	Order of suitability
Cu	29	1 032	3.98	119 113	8	3.68	110 135	10
Mo	42	2 167	1.38	125 599	7	1.88	171 106	8
Ag	47	832	4.18	163 450	4	3.18	124 350	9
Ta	73	2 587	0.55	103 868	9	1.13	213 402	6
W	74	2 757	1.3	265 223	1	1.81	369 273	1
Re	75	2 557	0.71	136 160	6	1.38	264 650	4
Os	76	2 280	0.87	150 754	5	1.77	306 706	3
Ir	77	2 220	1.46	249 572	3	2.06	352 136	2
Pt	78	1 742	0.71	96 472	10	1.41	191 585	7
Au	79	1 063	3.14	263 687	2	2.81	235 975	5
U	92	1 132	0.25	26 036	11	0.75	78 108	11

In Table 4, ρ represents the material density and *c* its specific heat. Thus, it is clear from Table 4 that the ideal material to use as an anode target is Tungsten, which is why this material will be recommended for use in the experiment.

4.3.2.7 Physical tube

The supplied current is of course directly proportional to the photon emission, since doubling the current would double the number of electrons fired. Assuming that the energy is dissipated, the number of photons produced would also double. In the interest of maximising the photons produced, a higher current would be desirable. Figure 23, however, shows operational curves for various X-ray tubes.

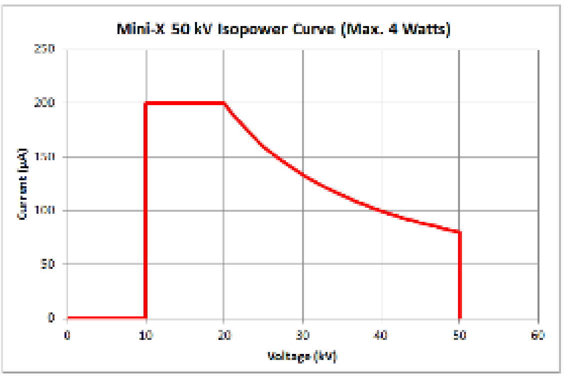

Figure 23: Isopower curve for mini-x tube (AMETEK, 2014)

The specific tube represented by Figure 23 is designed to operate between 10 and 50 kV. The maximum current that the circuitry can handle is 200 mA, and for this reason, there is a plateau at the beginning of the curve. The maximum power that this specific device can handle is stated as 4 W. Therefore, the current must decrease as the voltage increases by the well-known relation shown in Equation 65.

$$P = VI \tag{65}$$

A balance must thus be reached when choosing the operational point for the X-ray source since, as depicted in Figure 20, most of the low-energy X-rays are lost due to attenuation. The voltage must thus be high in order to produce enough high-energy photons, but the current must also be high in order to increase the total number of photons.

4.3.2.8 Conclusion

The production of X-rays is a complex process that is based on several complex interactions. However, assumptions can be made to simplify the production modes for functional predictions. One should know much about the specific X-ray tube that is being analysed to accurately model the produced Bremsstrahlung. Much research has been conducted on the accurate modelling of X-ray spectra and, although characteristic energies are easily modelled, there are also several semi-empirical models for tungsten target tubes in particular. This is convenient, since Tungsten is the most applicable material and is used in the X-ray tube at the South African Nuclear Energy Corporation (NECSA).

4.3.3 Modelling of X-ray spectra

4.3.3.1 Introduction

In an attempt to determine if the X-ray spectrum plays a role in the overall reaction rate at a particular point in the sample, effort was devoted to the ability to model the X-ray spectrum. The modelling is also used to determine the most applicable X-ray tube design for the purpose of the experiment.

Kramer's formula is used for the model. However, an attenuation factor *F(E)* is included to determine the X-ray spectrum at a given point, as shown in Equation 66 (an adapted form of Equation 57).

$$Count(E) = CZ(E_o - E)F(E) \tag{66}$$

The attenuation factor *F(E)* can be represented as a combination of all the materials that attenuate the X-rays. An example based on Figure 24 is shown in Equation 67.

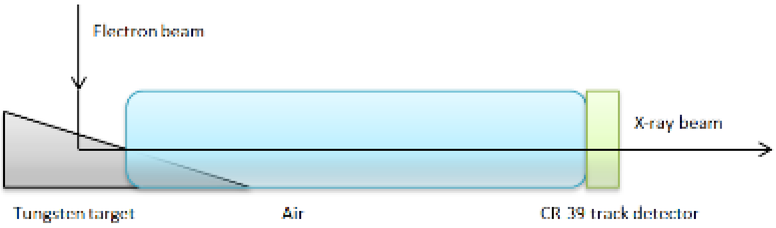

Figure 24: Set-up for X-ray attenuation example

$$F(E) = F_{tung}(E) \times F_{air}(E) \times F_{CR-39}(E) = e^{-\mu(E)_{tung}t_{tung}} \times e^{-\mu(E)_{air}t_{air}} \times e^{-\mu(E)_{CR-39}t_{CR-39}} \tag{67}$$

4.3.3.2 Attenuation coefficient fitting

An initial study into attenuation was done using data from Grodstein (1957). In an example, six attenuation coefficients were obtained at varied energies. The logarithm of each value at every known energy was used to generate a polynomial. This polynomial could be used to generate values for energies that are not given; the order of the polynomial was one less than the data points provided. Figure 25 shows a sample where air and Tungsten are considered. Cr-39 molecules are composed of light atoms. Consequently, the curves in each instance will be similar to those of air, which is why they will not be shown.

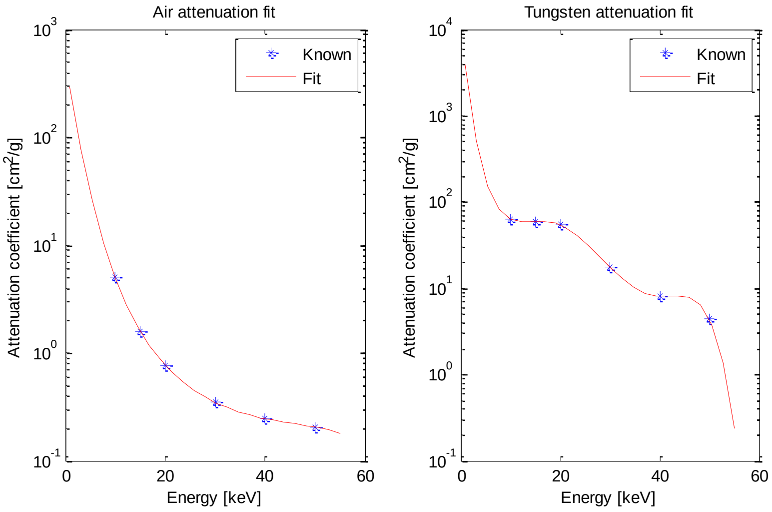

Figure 25: Attenuation fits for air and Tungsten

It is clear from Figure 25 that accurate results cannot be expected for values outside the range of known values. Nevertheless, a clear pattern is that, at low energies, the attenuation coefficients are extremely high, since low-energy X-rays are more easily attenuated. These fits can then be used to determine the attenuation factors as in the example shown in Figure 26.

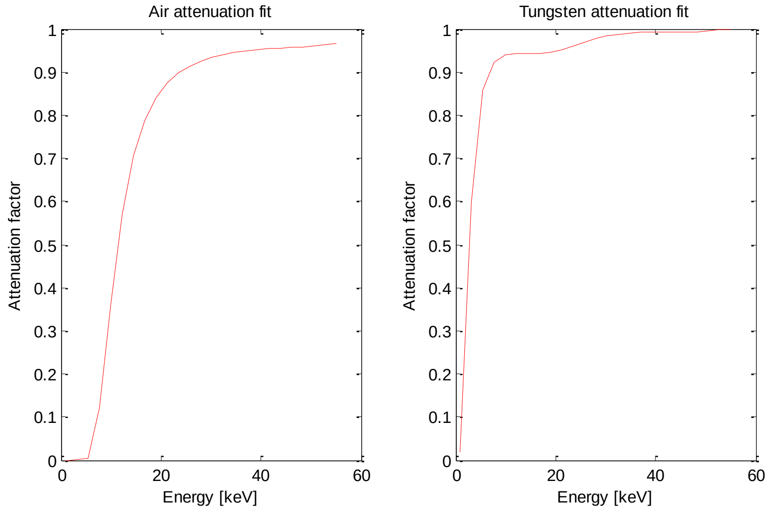

Figure 26: Attenuation factor example for air and tungsten

The attenuation factor is nonetheless a function of both the attenuation coefficients and the thickness of the material, where an increase in thickness will decrease the attenuation factor with a logarithmic proportionality as described by Equation 68.

$$F(E) = e^{-\mu(E)t} \qquad \{68\}$$

The total attenuation thus depends on the experimental set-up, where the Tungsten attenuation is a result of the X-ray machine configuration and the air attenuation relates to the distance of measurements from the X-ray source.

This approach may be accurate for materials with small atomic numbers, but for larger nuclei they fail to accurately represent some sharp edges. These sharp edges are a result of the atomic absorption edges. An example of these edges is shown in Table 5 for Tungsten. As explained in characteristic radiation production, the same effect may be reversed. In this process, the photon has exactly the energy required to push an electron into a higher orbital shell and there are specific energy levels between which the attenuation coefficients vary drastically. For this reason, the XCOM database (NIST – Physical Measurement Laboratory, 2014) is used to provide attenuation coefficients at a greater resolution. However, the energy levels that will be considered may not coincide with these values and thus, in order to provide nearly continuous results, an exponential interpolation algorithm was employed and plotted in Figure 30. The purpose of Figure 30 is to indicate how the interpolation matches the known data. Therefore, an example of both heavy and light elements is shown. LiH is used because its chemical properties are assumed to be equivalent to LiD.

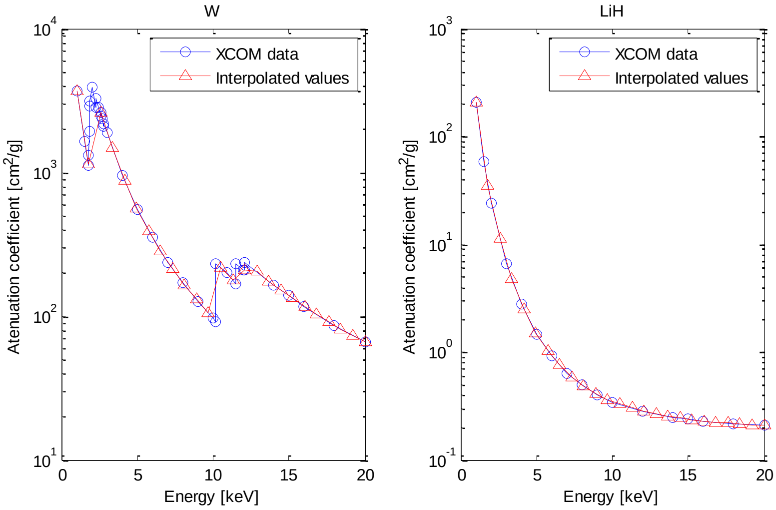

Figure 27: Attenuation coefficients for Tungsten and LiH

Figure 27 shows that there is a close correlation between the XCOM values and the interpolated values for materials that do not have sharp absorption edges or in energy areas where sharp edges are absent.

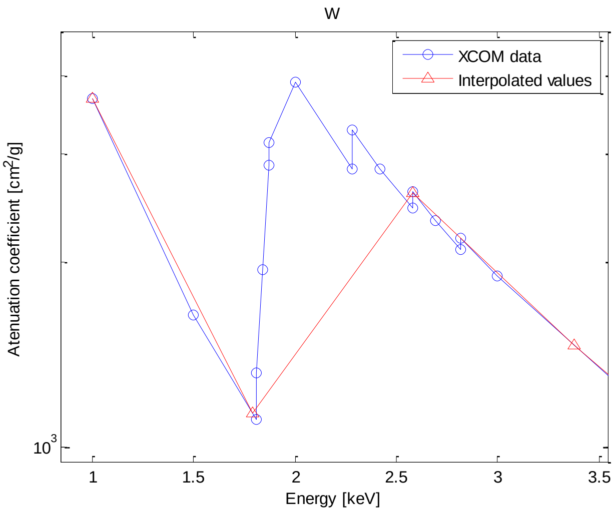

Figure 28: Closer evaluation of Tungsten attenuation coefficients

An analysis of a location where there is an absorption edge is seen in Figure 28. Here it is clear that the resolution of the analysis does not cover the effect of the absorption edges exactly. However, an increase in resolution, as shown in Figure 29, indicates that an accurate correlation is achievable using this method.

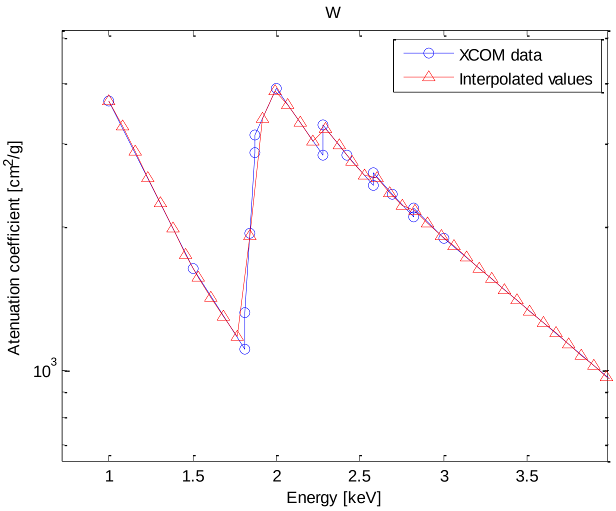

Figure 29: Closer evaluation of Tungsten attenuation coefficients with increased resolution

These attenuation coefficients can then be used as before to determine the attenuation factor at various energies when including the thickness of the materials. An example is shown in Figure 30.

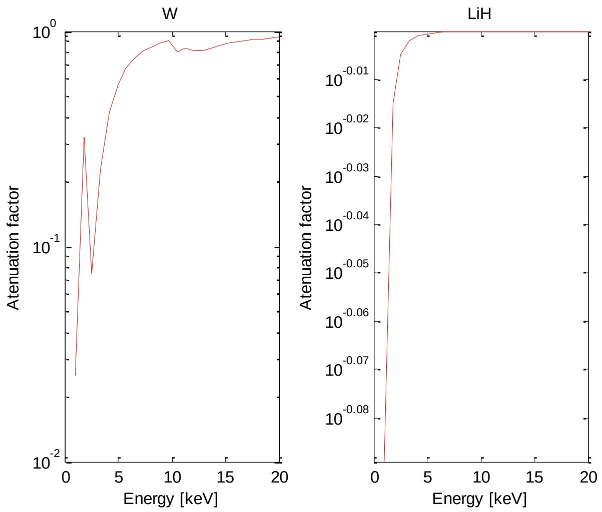

Figure 30: Attenuation factors for Tungsten and LiH

The two methods can thus be compared, and assuming that the XCOM interpolated values are more accurate, Figure 33 shows a good correlation between the methods in areas without absorption edges. In Tungsten, for example, the polynomial and interpolation methods are equivalent above 25 keV. This means that the polynomial method can be used if processing power is an issue to provide results that are useful. However, if accurate readings are a priority, the interpolation method is suggested at a high enough resolution.

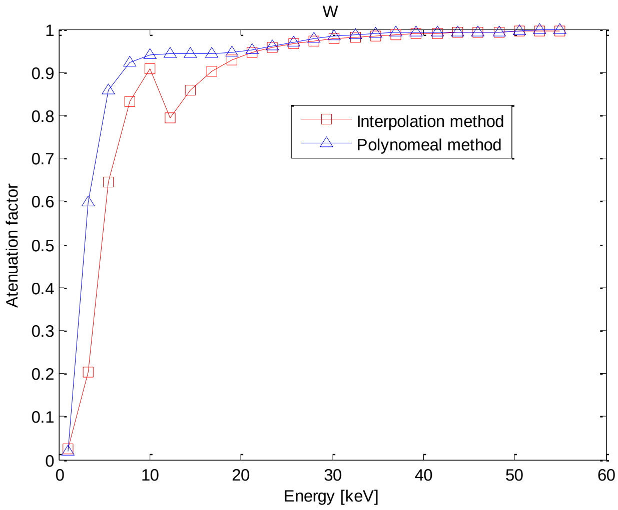

Figure 31: Comparison of attenuation factors

4.3.3.3 Factors influencing Bremsstrahlung

As indicated in section 4.3.2.6, the material selection plays a role in the resulting spectrum. Figure 32 shows that a higher atomic number has a significant effect on the produced spectrum. Clearly, more photons are produced in these instances. The results in Figure 32 are obtained by the application of Equation 64 with a maximum energy of 100 keV.

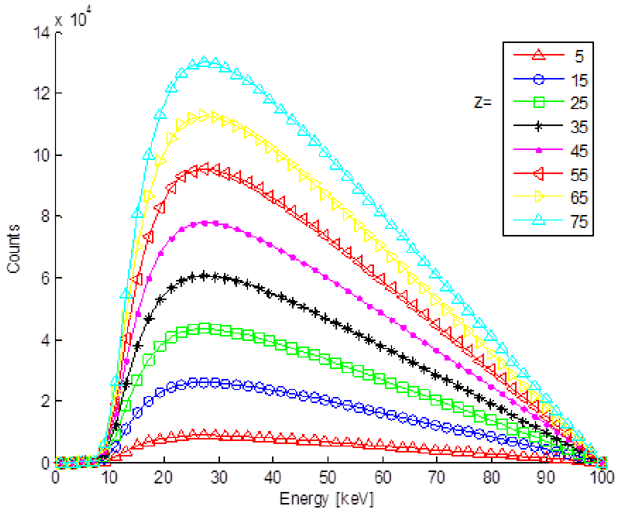

Figure 32: Bremsstrahlung spectra for elements with varying Z

On comparing the integrals of each of these cases, it can be calculated that the increase in energy produced by simply varying material is on average 36% for every increase of 10 Z for the values indicated. It is thus beneficial to have a higher Z value, as more electron energy is converted into photons. This is in agreement with the requirements for Equation 54.

The anode angle has also been indicated to have an effect. Figure 33 displays this relation graphically. However, direct analysis is pointless, since this effect is greatly influenced by the penetration depth. The useful point to note is that greater angles have fewer losses of photons into the anode material, as is to be expected. Note, however, that a significant increase in photons is no longer achieved by increasing the angle after about 35°.

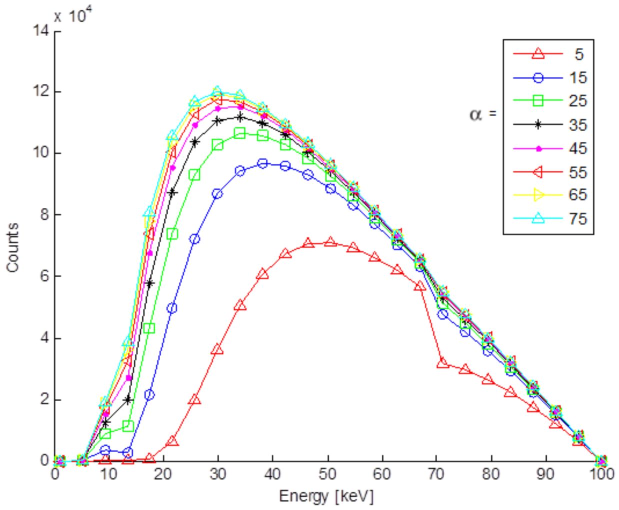

Figure 33: Effect of varying anode angle α on the X-ray spectrum

The dramatic drop near 70 keV for the 5° case occurs because the X-rays pass through much more of the anode material than at the other angles. Tungsten's attenuation thus becomes more pronounced and, consequently, the absorption edge that occurs in that region leads to a drop in photons.

Finally, varying the potential across the tube has been shown to have the most significant effect on the Bremsstrahlung spectrum, as described by Kramer's formula (Equation 53).

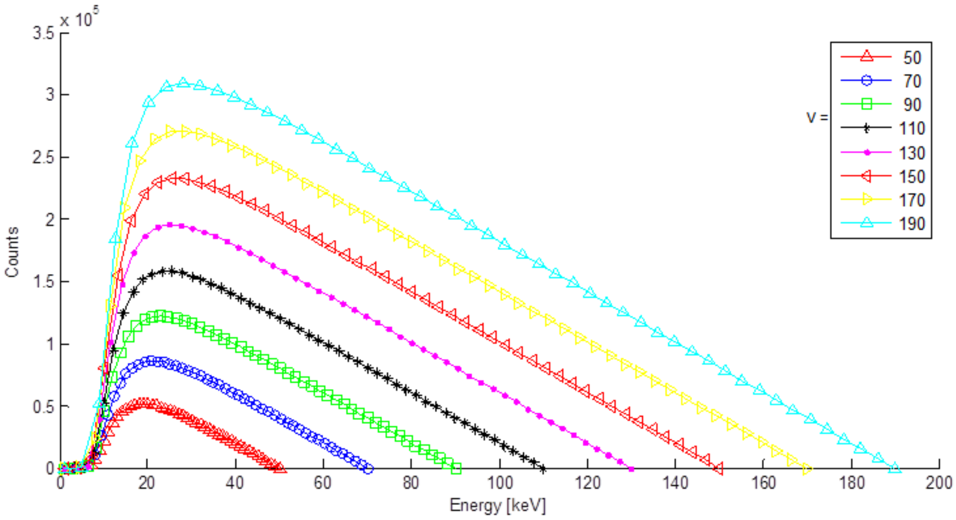

Figure 34: Effect of varying the applied voltage on the X-ray spectrum

Figure 36 emphasises that the photon intensity at every energy level can be increased by increasing the potential difference. This naturally also increases the total energy of the spectrum.

4.3.4 Measured spectra

4.3.4.1 Measurements

In order to analyse a true X-ray spectrum, communications with NECSA yielded results from one of its Tungsten sources.

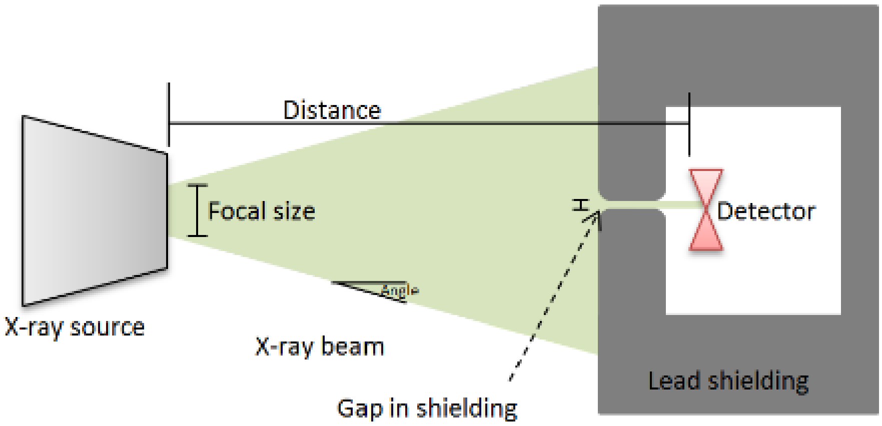

Figure 35: Schematic of X-ray measurements[11]

The experimental set-up required to measure the X-ray spectra is depicted in Figure 35. The voltage applied to the X-ray source, as well as the focal size of the source, are both controlled variables that are selected by the operator. The exposure time and distance between the detector and source are also controlled. Since X-ray detectors are extremely sensitive, shielding is required to prevent over-exposure of the detector. A small gap in the shielding allows X-rays to pass on to the detector and

---

[11] Components in the schematic are not to scale.

the shielding must be sufficient to block all X-rays that do not pass through the gap. A Germanium detector is used.

The first set of results (primary measurements) was generated while operating for 10 minutes at 0.5 mA with a distance of 250 cm between the detector and the source, a focal size of 1 mm and the X-rays emitted in a cone with a spread of 40°. The measurement interval for this experiment was 0.042 keV. Some of these spectra are indicated in Figure 36. The characteristic X-rays, in the form of peaks, can quite clearly be seen to deviate from the Bremsstrahlung spectrum shape.

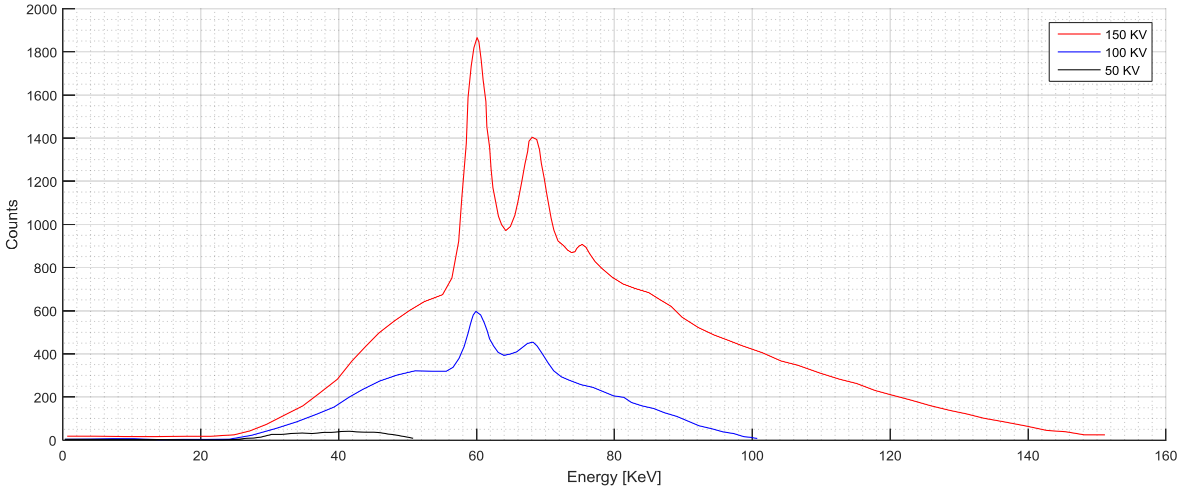

Figure 36: Primary NECSA measurements (smoothed)

The second set (secondary measurements) was compiled by operating for five minutes at 0.1 μA with the detector a distance of 105 cm from the generator. All other operational fields are identical to those used in the primary measurements. The energy intervals that are measured are increased to 1 keV. Therefore, the results of Figure 37 show less noise. The magnitudes of the secondary measurement counts are greater than those of the primary measurements because they are closer to the source, but also because of the larger measurement interval.

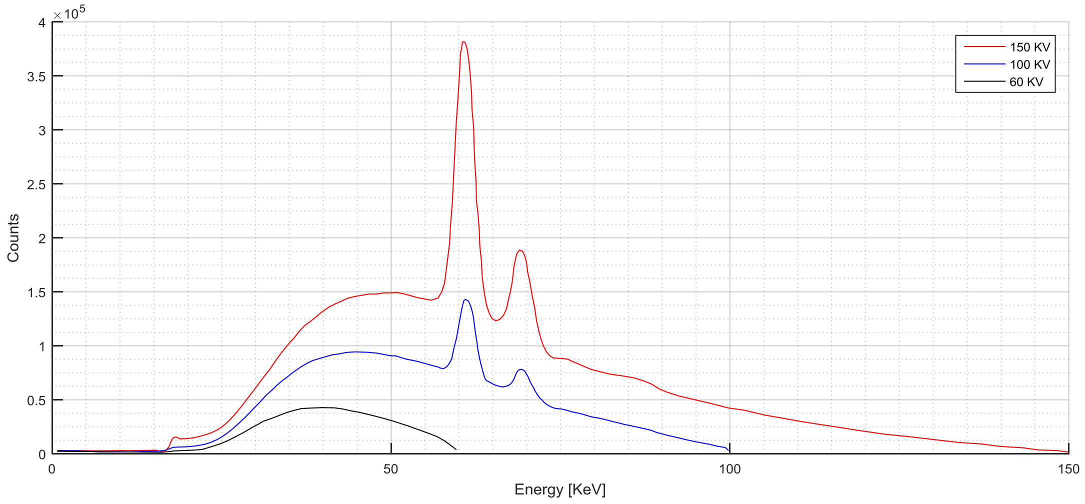

Figure 37: Secondary NECSA measurements

In order to compare the primary and secondary results, the spectra must first be normalised by dividing the entire spectrum by the number of counts at the energy interval that has the maximum number of counts for each spectrum respectively.

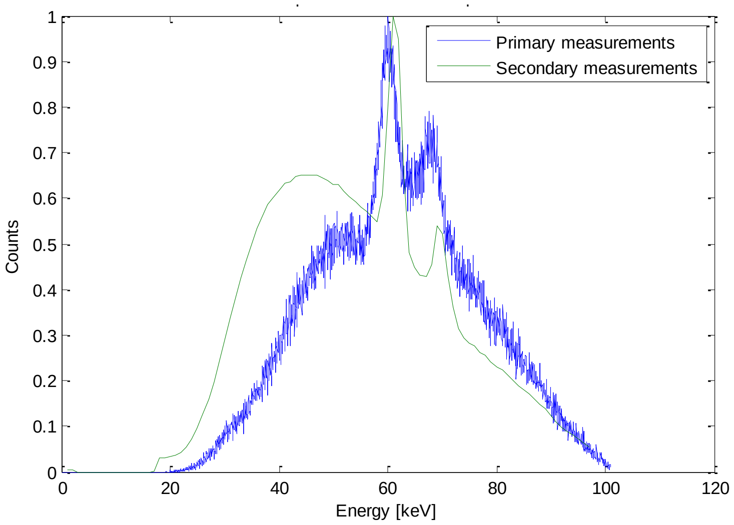

Figure 38: Initial comparison of measured spectra

Figure 38 shows that there is a correlation for the characteristic locations, but that the spectra are not coincident. Since the geometries differ, the secondary spectrum is adjusted by attenuating the spectrum through an additional 145 cm of air, using the photon cross-section data of NIST – Physical Measurement Laboratory (2014) as a source for the attenuation coefficients. The spectra can now be compared since the geometries match.

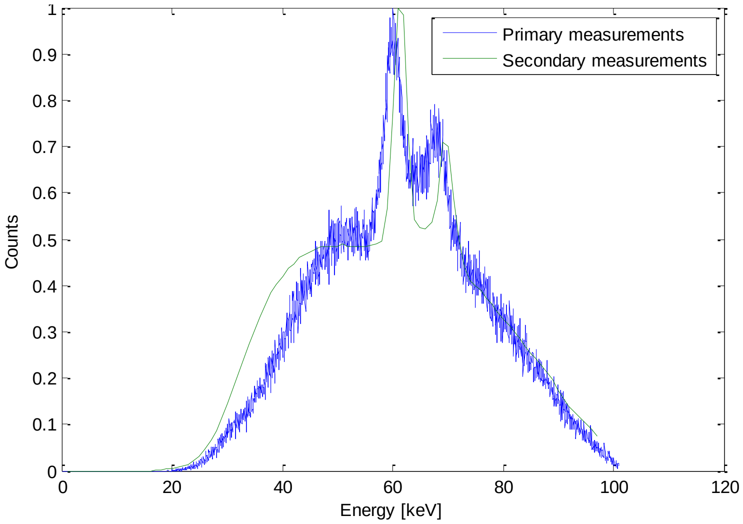

Figure 39: Spectral comparison with added attenuation

Upon integrating both spectra, it is determined that there is a 96.6% correlation (shown in Figure 39). It was noted that it was very difficult not to over-expose the detector and this may account for some of the discrepancy. The rest may be attributed to a slight difference in environmental conditions and a difference in the age of the equipment between the two experiments. Since there are fewer results in the secondary measurements, it would take less computational time to use these results for a numerical comparison. Consequently, the secondary results will be used as the baseline in the experimental section.

4.3.4.2 *Shifting of spectra*

As introduced in section 4.3.2.2, each target element will produce characteristic X-rays. The energies of these characteristic X-rays are well documented and can be identified based on the orbital location of the electrons that are ejected to produce this type of radiation. Since these characteristic rays produce characteristic peaks in the X-ray spectra, the peaks of the measured results should coincide with the energies where characteristic X-rays are produced. The characteristic X-ray line energies for Tungsten are shown in Table 5.

Table 5: X-ray absorption edges and characteristic X-ray line energies [keV] (Plechaty, Cullen & Howerton, 1975)[12]

Atomic number and element	K-series						L-series											
	K edge	KN_{III}	KM_{III}	KM_{II}	KL_{III}	KL_{II}	L_I edge	L_IN_{III}	L_IM_{III}	L_IM_{II}	L_{II} edge	$L_{II}N_{IV}$	$L_{II}M_{IV}$	L_{III} edge	$L_{III}N_V$	$L_{III}M_V$	$L_{III}M_{IV}$	$L_{III}M_I$
		$K\beta_2$	$K\beta_1$	$K\beta_3$	$K\alpha_1$	$K\alpha_2$		$L\gamma_3$	$L\beta_3$	$L\beta_4$		$L\gamma_1$	$L\beta_1$		$L\beta_2$	$L\alpha_1$	$L\alpha_2$	L_I
Intensity	-	5-15	~20	~10	100	53-65	-	~5	35-20	20	-	5-25	100	-	5-20	~90	10	20-5
74 W	69.517	69.100	67.244	66.951	59.318	57.982	12.092	11.675	9.819	9.526	11.535	11.284	9.671	10.199	9.959	8.396	8.335	7.388

For the purpose of evaluation, the values of Table 5 are graphically represented and superimposed on Figure 38 to generate Figure 40. It can be seen here that there is a slight deviation from the theoretical values.

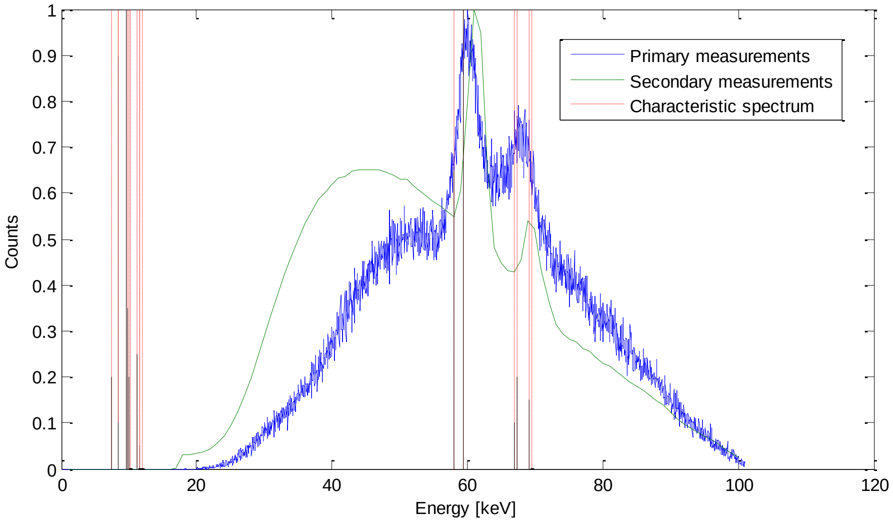

Figure 40: Characteristic evaluation

The deviation is magnified in Figure 41.

---

[12] *K* and *L* refer to the electron orbitals for the atom.

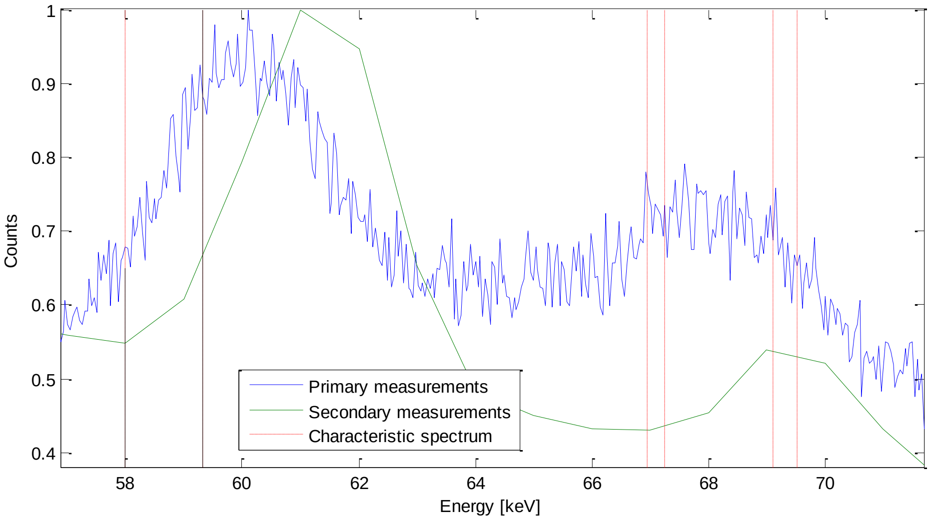

Figure 41: Magnification of Figure 40

The spectra for both the primary and secondary measurements are shifted lower by 0.77 keV and 1.68 keV respectively to ensure that the peaks line up with the energies where characteristic X-rays should occur, as shown in Figure 42.

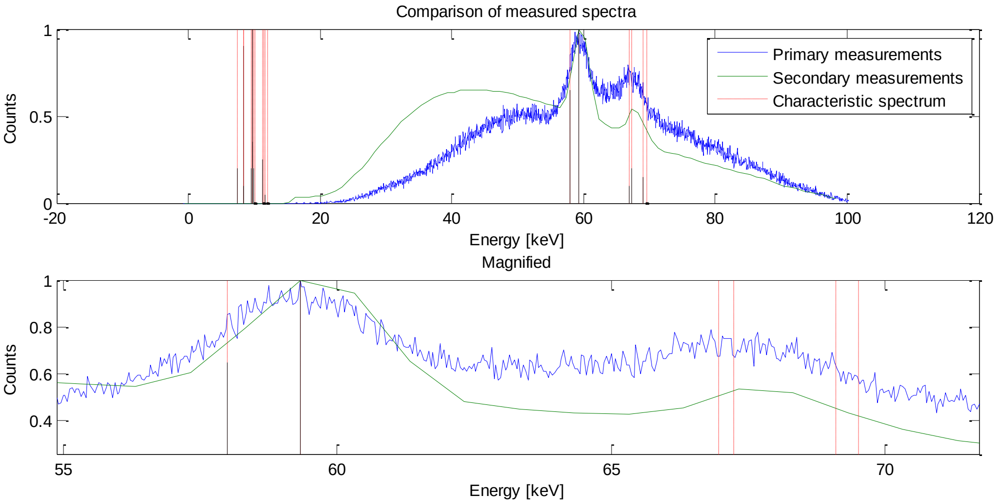

Figure 42: Shifted spectra

The shift is a result of the detector, as well as the energy interval sizes. For the smaller intervals, the shift is smaller, whereas the shift is less than two intervals for the secondary set. For the purpose of analysis, this shift will be permanently applied and considered a correction for measurement faults.

4.3.4.3 Fitting

In order to determine if theoretical models are in any way useful, a theoretical model is compared to the spectrum that was measured by NECSA. The spectra are both normalised by setting the Bremsstrahlung peak of both spectra as equivalent, since exposure time and current can be varied to allow for the differences in magnitude.

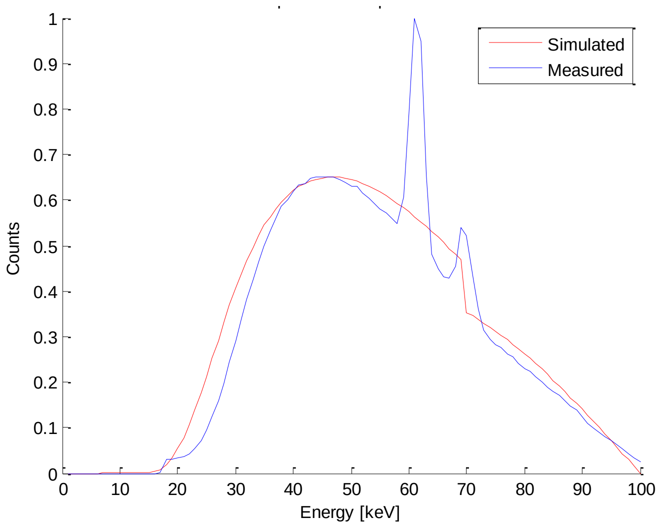

Figure 43: Fitting simulated data to measured data

The spectrum provided by the theoretical model can be made to match the measured spectrum by applying various filters. These filters change the shape of the spectrum due to attenuation, and although the thickness of some filters (like air) is known, the thickness of certain filters are unknown (such as the depth of the Tungsten target and the thickness of the Beryllium lens on the X-ray tube). These values are optimised in order to attempt to match the measured shape. The theoretical model accounts for absorption edges, but does not include characteristic X-ray emissions. This will account for a discrepancy in the results. The average error in the shown instance (Figure 43) is 6.49%. More strenuous optimisation algorithms can be used to reduce the deviation in the theoretical results.

4.3.5 Conclusions

The X-ray spectrum produced by NECSA should be used as a baseline, rather than using theoretical results, since it includes the characteristic X-ray emissions. The NECSA results also inherently include the attenuation of the anode material target, the anode angle and the general performance characteristics of the specific equipment. The theoretical and physical results can be made to match above 93.5% for Bremsstrahlung, and when considering the attenuation as an exponential interpolation method, the attenuation coefficients can be accurately calculated using the NIST data (NIST – Physical Measurement Laboratory, 2014).

5. Experiment

5.1 Preparation

5.1.1 LiD powder

The LiD powder was provided by Sigma-Aldrich and has a deuterium enrichment of 98%. For non-proliferation reasons, it no longer supplies Li-6D and the LiD powder provided has a Li-6 enrichment equivalent to that of the isotope in nature, which is 7.59%[13].

LiH is hygroscopic and it was imperative that the material be prepared in a dry environment. Several steps were taken to ensure that this would be the case. The material was originally in the form of crystal chunks, which is not suitable for placement between detector plates. The chunks were opened in an anaerobic chamber that consists of a dry CO_2 atmosphere. Argon could also have been used, but it releases soft X-rays at just above 3.2 keV that may affect the experimental results. Desiccants were present in the chamber and, since a positive pressure of CO_2 gas had to be maintained, the compressed gas was released in the physical vicinity of the LiD, freezing any residual moisture particles.

The chunks were processed into powder form using a mortar and pestle. When the sample assembly was completed and the chamber seal was released, a noticeable reaction took place between the incoming moisture-rich air and the LiD powder present on the container surfaces. This served as an indication that the process occurred in an extremely low-moisture environment, since such a reaction did not take place during the preparation. A schematic of the glove box is provided in Figure 44.

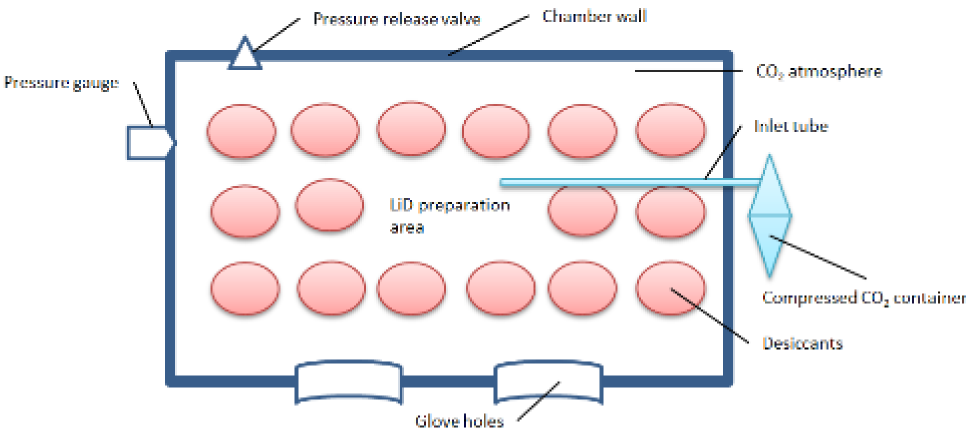

Figure 44: Glove box schematic

5.1.2 CR-39

CR-39 was stored in a container that only high-energy cosmic radiation could penetrate. The containment was opened within an anaerobic chamber made of plastic with a CO_2 environment. The samples were assembled and irradiated at NECSA. On return, the samples were disassembled once more in an anaerobic chamber to avoid Radon tracks[14]. The detectors were cleaned using ethanol

---

[13] The composition of the LiD powder is noted in Table 10.

[14] The energy of α-particles emitted by Radon decay is shown in Table 9, and the decay is shown in Figure 5 of Appendix A.

and an ultrasonic shaker and were then washed with ultrapure water. The detectors were then etched to enlarge the tracks in two sessions using a 6.25 $\frac{mol}{l}$ solution of NaOH at 70 °C for eight hours. The detectors were then once more cleaned using ultrapure water and an ultrasonic shaker.

5.1.3 Samples

The first two samples were designed as indicated in Figure 45. These were manufactured from Perspex. A Perspex lid with a thickness of 5 mm was placed on the bottom of each of these before assembling the final product, and was tested to be airtight at a pressure of 1 atm.

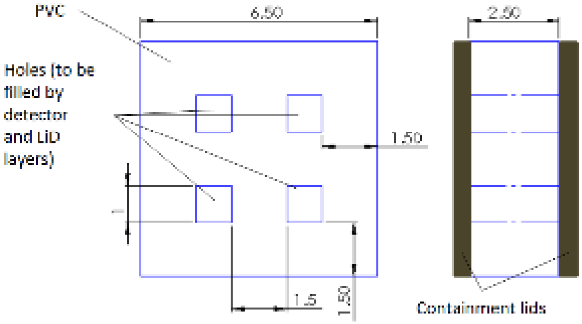

Figure 45: Original sample container configuration

These samples were then introduced into the anaerobic chamber along with the unopened LiD and unopened CR-39 detectors. The detectors also had dimensions of 1 cm by 1 cm and were dropped into the sample with LiD powder in between. Figure 46 shows how the containers were filled with layers of LiD powder, which were separated by CR-39 track detectors.

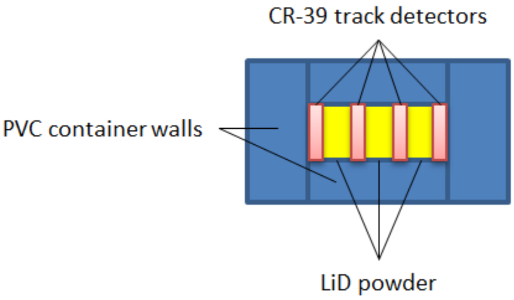

Figure 46: Powder/detector set-up

As a matter of convention, holes that are used to contain powder/detector layers are referred to as “lines”. Because of the slight differences in dimensions, some of the lines could not be compiled or only partially compiled. This is to say that the powder/detector sequence could not be fully achieved in every one of the available lines. They were labelled alphabetically in a clockwise fashion. The detector number and orientation were recorded in every instance. Once preparation was complete, adhesive was used to secure another Perspex lid on the exposed side of the sample, and silicone sealant was used over the interface to ensure there was no leak.

The second sample container configuration, as shown in Figure 47, has a slightly different design. While the purpose of the first design is to analyse the effects with a high resolution, this design needs to consider the bulk reaction rate difference.

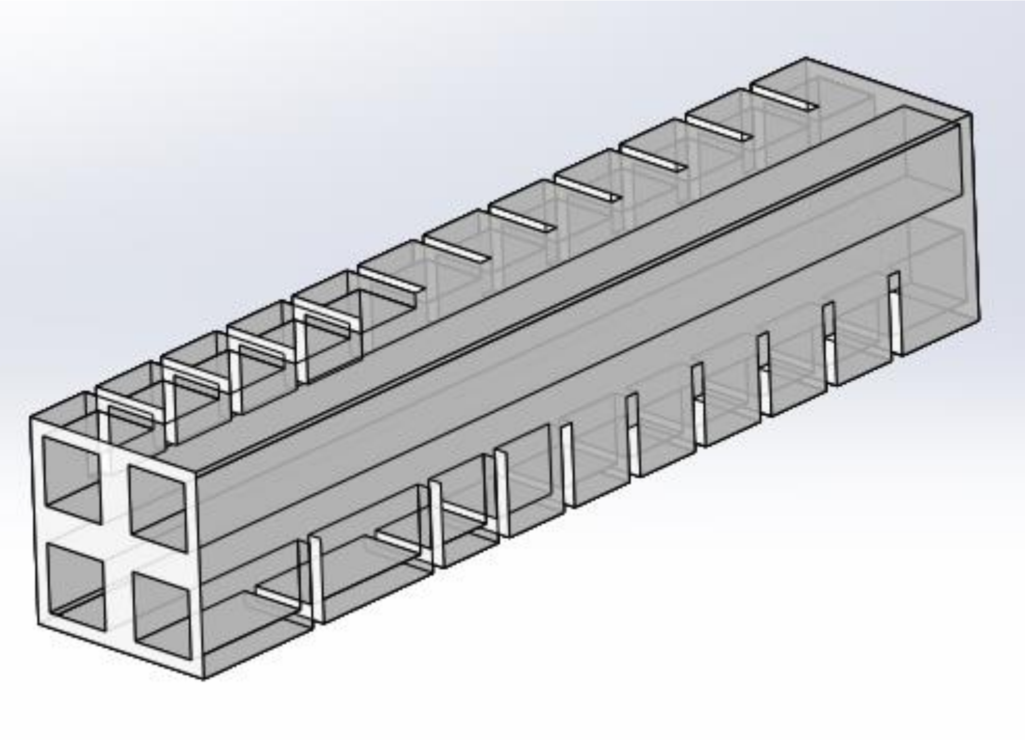

Figure 47: Secondary sample design

The Perspex structure is 13.2 cm long and contains tubes with an internal size of 0.95 cm. A lid was sealed onto the one side and the tubes were filled with LiD powder. As each hole in the side was reached, a detector was slid into place. Some 1 cm of powder was thus inserted between each detector, except for two cases where the detectors were 2 cm apart. In the two empty channels, detectors were placed for control purposes. The sample was also sealed at the top and sealant was used to ensure that air does not enter through the detector-Perspex interface. The powder/detector assembly is thus similar to that illustrated by Figure 46, the only differences between the original and secondary container designs being how the detectors are introduced into the assembly, the dimensions and the thickness of the LiD layers.

5.1.4 Anaerobic chamber

The purpose of the anaerobic chamber is thus to grind the LiD particles into powder and assemble the samples to be exposed in a CO_2 environment so that the LiD does not react with either moisture in the air or the atmosphere provided. Desiccants will also be used in the chamber to collect H_2O.

5.1.4.1 Manufacture

A plastic crate was converted for this purpose. Two holes were made for gloves to be inserted and they were sealed. Since the plastic was opaque, a Perspex window was fitted to the crate and sealed into position. A pressure gauge was added to measure the internal pressure as a safety precaution. Two bicycle valves were installed so that the CO_2 could be introduced and the initial atmosphere may be displaced. A weatherproofing sponge was used to line the lid of the crate and ropes were used to apply external force to the lid under operating conditions. A schematic of the prominent features of the glove box is shown in Figure 44.

5.1.4.2 Testing

The chamber should operate at atmospheric conditions. For this reason, it does not need to be considered a pressure vessel. The chamber was tested by filling it with smoke and increasing the internal pressure. The chamber was then visibly inspected for signs of leaking smoke. This test was repeated twice, since the first test led to the resealing of certain sections. During the second test, the smoke did not leak out under atmospheric conditions and a slight increase in pressure could be obtained without the seal being broken. The main cause of leakage was the deformation of the chamber under increased pressure.

5.1.4.3 Conclusions

The chamber was considered acceptable, since the gases within the chamber would pose no threat in the event of leakage into the atmosphere and it would only be operated for a few hours. The chamber will thus be kept with an overpressure of at least 0.05 atm and CO_2 will be periodically added to ensure that this overpressure is maintained.

5.1.5 X-ray source

The X-ray source that was used to generate photons for the bombardment of the samples was a XYLON Y.TU 225-D02 tube. The X-ray tube was operated with a potential difference of 100 kV. As shown in Figure 48, the total current available was 30 mA when drawing 3 000 W. The focus size of the target used was 5.5 mm and the spread of the emitted radiation was a cone of 40°. A permanent 0.8 mm thick Beryllium filter was present, as the X-ray tube window and the Tungsten anode have a flat profile. Water was used as a coolant to cool the system. When the X-ray generator is operated at 3 000 W, the cooling system requires 2 400 W.

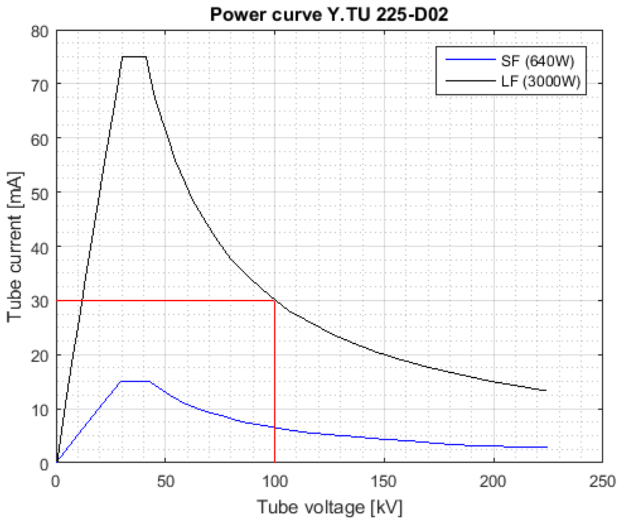

Figure 48: Tube operating conditions

5.2 Set-up and procedure

The set-up for the irradiation experiment was relatively simple, as shown in Figure 49.

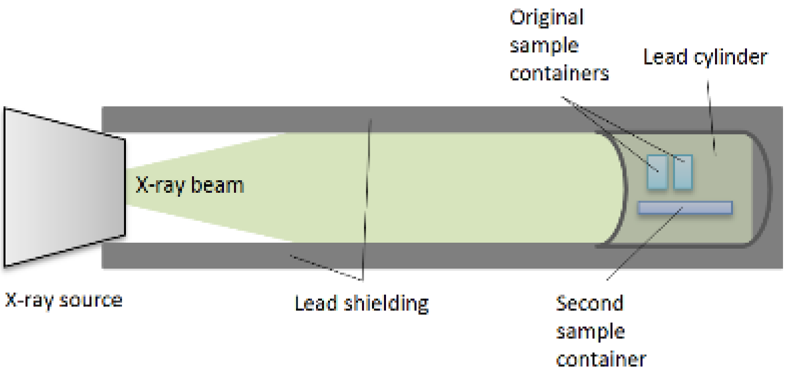

Figure 49: Irradiation experiment set-up

The X-ray source was aligned with the sample containers and lead shielding walls were erected to contain the X-rays within the testing environment. As an additional safety precaution, the experiment set-up was rigged with a trip switch that was connected to a motion detector – so that the X-ray source would shut down as soon as someone entered the room where the irradiation was taking place. Three sample containers were prepared, two of the original design and one of the secondary design. The two containers of the original design were lined up behind one another and the secondary design container was placed next to them. This translates into powder/detector lines perpendicular to the incoming X-rays. The second sample container design was placed 58 cm away from the X-ray source and the original sample containers were placed in line, 60 cm and 64 cm from the source respectively. The time that the source was active was recorded so that the power drawn by the system could be used for analysis. Once irradiation was complete, the samples were collected and disassembled in anaerobic conditions.

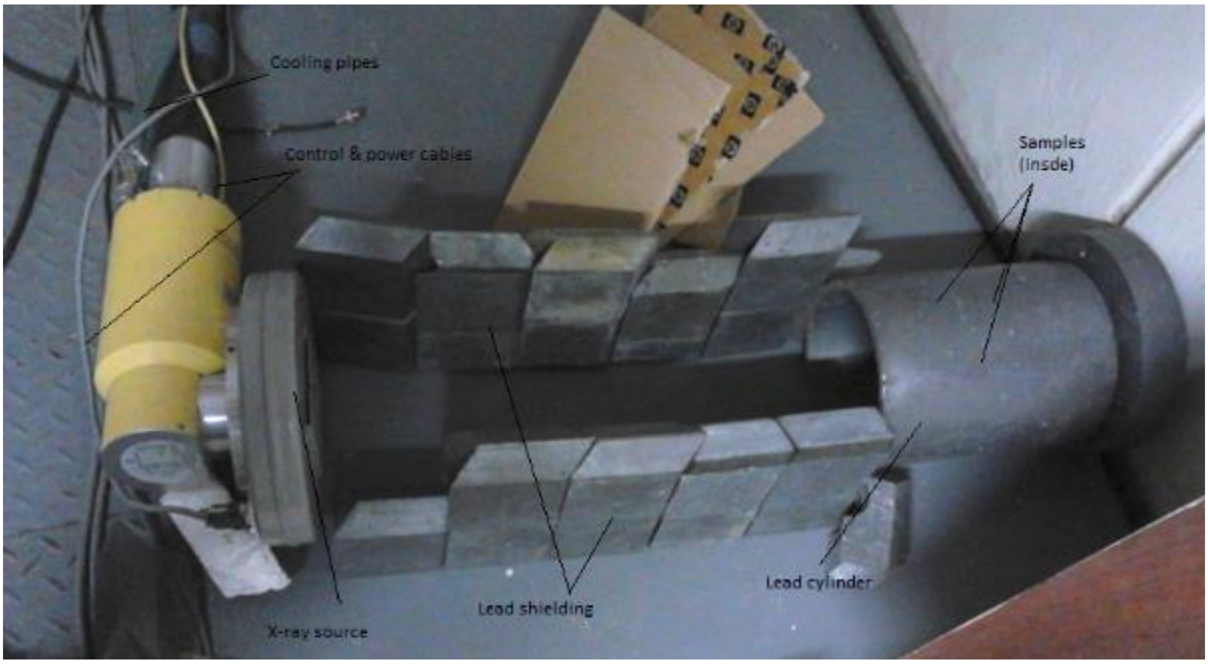

Figure 50: Photograph of experimental set-up

5.3 Conclusion

The experimental set-up has been designed in such a way as to minimise environmental interference. Safeguards such as desiccants were in place in order to limit moisture, and a positive-pressure CO_2 environment was maintained during preparation so that Radon contamination may be minimised. The sealing of the samples whilst within containment further aided in avoiding environmental interference from occurring during the testing phase.

Detectors were spaced at fixed dimensional intervals so that the energy disposition into the crystals could be more accurately modelled during the investigation phase. The etching of the detectors was done in a controlled environment, and the detectors were properly cleaned limiting the aging of the detectors during microscopy.

Safety precautions were taken when setting up the x-ray bombardment phase, and a source was selected in order to provide a large number of x-rays of the required energy.

6. Theoretical analysis

6.1 Energy deposition

6.1.1 Introduction

The energy absorbed by the material should be considered when calculations are made as to the efficiency of the process. To determine the energy absorbed by the material, a theoretical analysis of each of the samples is considered.

6.1.2 Procedure

6.1.2.1 Area correction

Since the total area covered by the X-rays varies as a function of distance to the source, it must be recognised that the intensity is decreased. A visualisation is provided in Figure 51.

In order to determine the effect on the intensity of the X-rays by the dispersion, the calibration experiment mentioned in section 4.3.4 is used. Beginning with a diameter of 1 mm as a source, with a spread of 40°, the effective point source can be calculated at a distance of 1.192 mm into the X-ray tube.

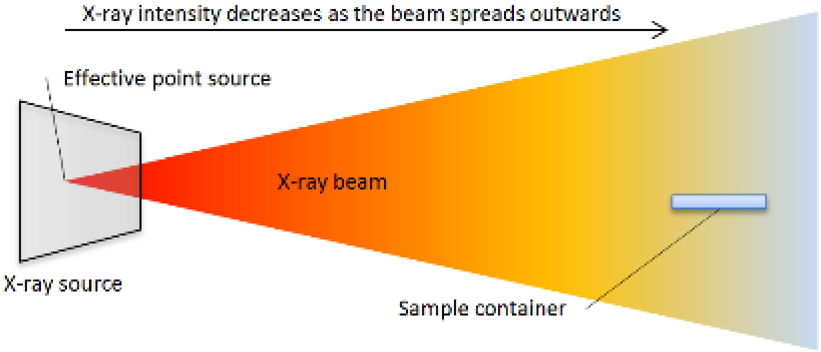

Figure 51: X-ray beam dispersion

The beam diameter at 105 cm is calculated as 1 764.11 mm. This translates into an area of 2.44×10^6 mm^2. The Germanium target is circular and has a diameter of 6.5 cm and an area of 3.32×10^3mm^2. This means that the fraction of X-rays being received by the detector is 0.1%.

By the same method, using a 5.5 mm source diameter, the effective point source is 2.681 mm away. This refers to the experiment where the LiD samples were irradiated. The case for a detector at 58 cm and 76 cm away from the source respectively is to be considered.

The effective areas are 750.996×10^3 mm^2 and 1.286×10^6mm^2 respectively, whereas the area of the sample is 90.25 mm^2. This leads to the respective fractions being 1.201×10^{-4} and 7.014×10^{-5} respectively. The difference between the two is 58%. This indicates that a simple adjustment cannot be made to represent the total energy loss through position.

A correction will thus have to be made for the total energy available per unit distance from the source. However, calculation indicates that for a Δt of 0. 095 mm (the relevant thickness of LiD)[15], the difference is only 0.039% and can thus be considered negligible. (Assuming that it is negligible would mean that the energy actually absorbed is less than the calculated energy absorbed in the material. This would result in the calculated efficiency of the system being lower than that of the true efficiency.)

Effectively, the intensity deviation as a function of distance from the source can be surmised as shown in Equation 69 for the particular test set-up.

$$I(x) = I_o \times \frac{A_{powder}}{\frac{\pi}{4}((0.2681+x)\cdot 2\tan(40))^2} \tag{69}$$

6.1.2.2 Compton scattering correction

Since the walls used to contain the X-rays within the experimental set-up are Lead, a consideration must be made as to the effect of Compton scattering. Compton scattering occurs when photons are scattered from charged particles – in this case the electrons surrounding the lead atoms. The Compton formula is shown in Equation 70 (Williams, 1977).

$$\lambda_f - \lambda_i = \Delta\lambda = \frac{h}{m_e c}(1 - \cos\theta) \tag{70}$$

In Equation 70, *h* represents Plank's constant, *c* is the speed of light in a vacuum, λ represents the photon wavelength and m_e is the rest mass of an electron. Since this investigation deals with the photons in energy form and not in wavelength form, the conversion shown in Equation 71 can be applied (where *E* is the photon energy).

$$E = \frac{hc}{\lambda} \tag{71}$$

Combining equations 70 and 71 yields Equation 72, which can be simplified to Equation 73.

$$\frac{hc}{\lambda_f} = \frac{hc}{\lambda_i} + \frac{hc}{m_e c^2}(1 - \cos\theta) \tag{72}$$

$$E_f = \left(\frac{1}{E_i} + \frac{1}{m_e c^2}(1 - \cos\theta)\right)^{-1} \tag{73}$$

---

[15] This is calculated in section 6.2.3.

In order to evaluate the effect of Compton scattering, a case where a photon collides with the lead barrier once and then recoils and hits the samples must first be considered, as illustrated in Figure 52.

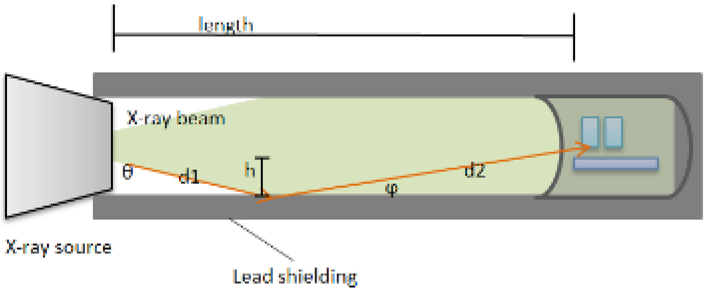

Figure 52: Single Compton scattering case

In order to determine the energy of a phonon that followed the path as shown in Figure 52, the distance travelled, as well as the incident angles, must be determined. This is done using trigonometry as considered in equations 74 and 75.

$$\phi = \tan^{-1}\left(\frac{h}{l - \frac{h}{\tan(90-\theta)}}\right) \qquad \{74\}$$

$$dist = \frac{h}{\sin(90-\theta)} + \frac{h}{\sin(\phi)} \qquad \{75\}$$

The energy lost in the scattering process, as well as the additional attenuation of the photon, must be considered. The distance calculated in Equation 75 must be used when considering a beam of X-rays that follows a specific path in order to provide accurate results.

In order to determine the effect of the increase in the number of X-rays that hits the samples after being recoiled, a Monte Carlo simulation was set up with the dimensions of the experimental set-up. An example is shown in Figure 53.

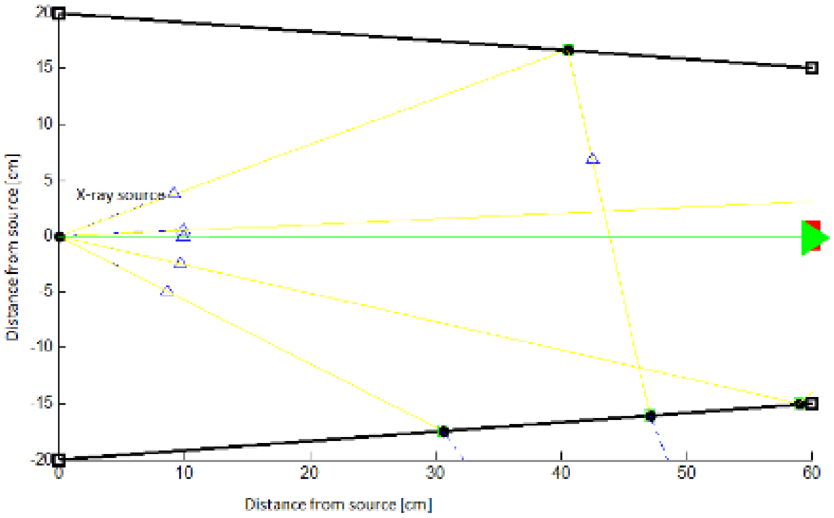

Figure 53: Two-dimensional scattering example

In Figure 53, the yellow lines track the movement of the photons, black dots indicate where photon calculations are made from, the black lines are the walls, the red box is the target (representing the sample) and the green line indicates a photon that has hit the target. This simulation was allowed to run so that observations may be made from it. The result is shown in Figure 54.

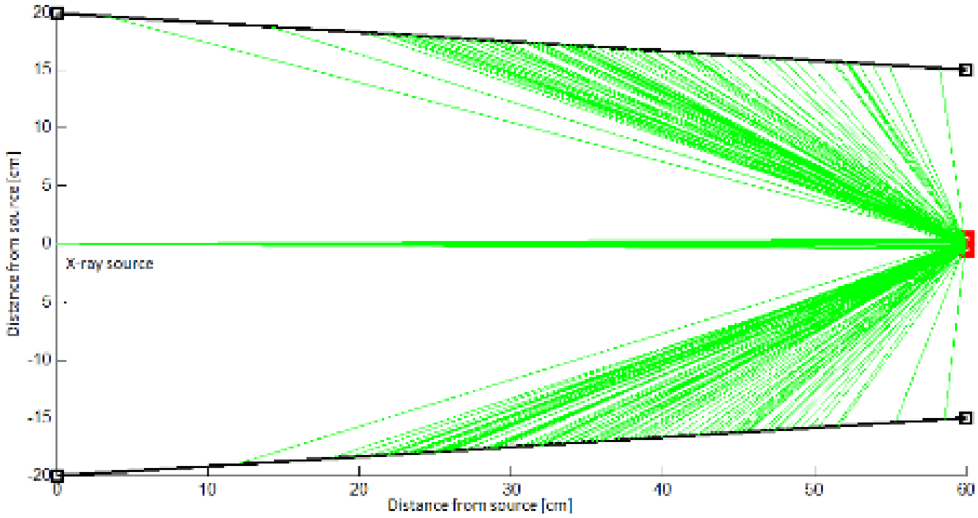

Figure 54: Two-dimensional scattering results

Figure 55 could be generated from the data on which Figure 54 is based.

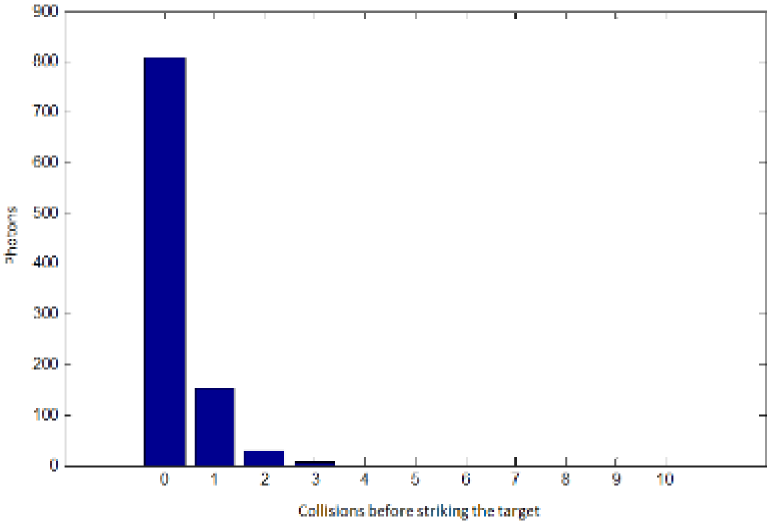

Figure 55: Collision distribution for the two-dimensional scattering problem

Figure 55 shows that most of the photons that reach the target stick to the target without colliding with the walls of the experiment. However, the total number of photons that reach the target is increased by 22.35% if photons that collided with the walls are considered. This is, however, only valid for a two-dimensional problem. The model or the three-dimensional problem is shown in Figure 56.

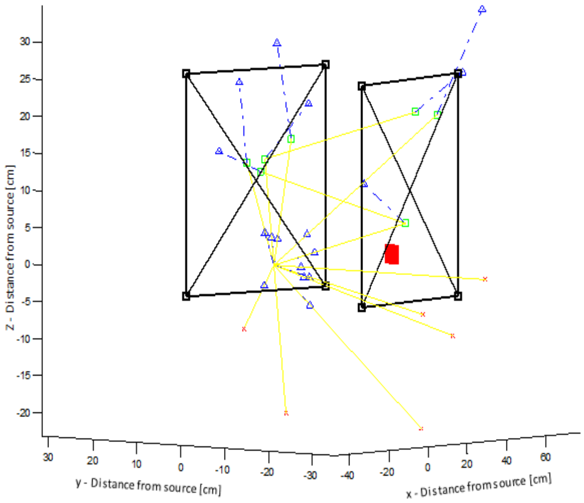

Figure 56: Three-dimensional scattering example

The legend for Figure 56 is the same as for Figure 53. Running a simulation in three dimensions indicates that, for the specific problem, the percentage of photons that hit the target indirectly is below 10^{-4}. In order to accommodate this, the attenuation coefficients that were selected from the NIST data (NIST – Physical Measurement Laboratory, 2014) include incoherent Compton scattering in order to provide conservative results.

6.1.2.3 Exposure correction

The generated spectrum from the calibration experiment in section 4.3.4 was produced by running a current of 0.1 μA over 100 keV for five minutes. This constitutes a power of 3×10^{-5}W and an energy of 9×10^{-3}J for the calibration test. The set-up for the sample irradiation was at a current of 30 mA for 111.466 hours. This means that 3 000 W was being used and that a total of 1 203 832 800 J was consumed (if the cooling system is ignored). The energy produced by the measured energy spectrum in section 4.3.4 must thus be increased in order to represent the magnitude of the energy produced during the irradiation of the LiD samples. The number of photons produced throughout the measured spectrum must thus be increased by a factor of 1.34×10^{11}. This then represents the energy spectrum for the experiment.

6.1.2.4 Build-up factor correction

When considering the energy absorbed by any shielding material, three standard methods can be used to evaluate the problem. Consider attenuation as described by Equation 76, where $I(x)$ is the intensity of the X-rays at point x, I_0 is the intensity of the X-rays at the source and *x* is the distance travelled by the X-rays through the material under consideration.

$$I(x) = I_0 \times e^{\mu x} \qquad \{76\}$$

The first approach is to consider μ as the linear attenuation coefficient, but this analysis ignores Compton scattering, as well as pair production photons. Therefore, it underestimates the thickness of the shielding required. The second approach defines μ as the linear energy absorption attenuation coefficient. However, this approach assumes that all scattered photons eventually reach the detector. It thus overestimates the thickness of the shielding required. A midway method that allows more accurate results is the use of a build-up factor to correct for Compton scattering and pair production without assuming that all scattered photons reach the detector. The formula that replaces Equation 76 is thus Equation 77.

$$I(x) = I_0 B(E,t) \times e^{\mu x} \tag{77}$$

In Equation 73, μ represents the linear attenuation coefficient and the build-up factor is introduced by the expression B(E,t) – showing that the build-up factor is a function of both photon energy and the shielding thickness for a specific shielding material. In this study, the energy absorbed is only investigated for LiD and so analysis for this material is considered. Since LiH and LiD are chemically equivalent, the readily available build-up factors for LiH are considered as displayed in Table 6

Table 6: Table of build-up factors for LiH (Wallace, 1974)

	µx			
Energy (MeV)	**1**	**2**	**4**	**7**
0.5	2.56	5.66	17.8	52.9
1	2.08	3.75	8.48	18.1
2	1.8	2.72	4.77	8.23
3	1.65	2.33	3.72	5.88

The build-up factor increases for lower energies and it seems that it may play a big role, since the energies considered in this study range between 0.01 and 0.1 MeV..

Table 7 is provided to investigate the value of µx at various energies for LiH based on data from NIST (NIST – Physical Measurement Laboratory, 2014) for the linear X-ray attenuation coefficients.

Table 7: µx values for LiH

Energy (keV)	$\frac{\mu}{\rho}$	μ	μx **(1 cm)**	μx **(0,095 mm)**
10	0.345	0.274	0.274	0.003
15	0.238	0.189	0.189	0.002
20	0.209	0.166	0,166	0.002
30	0.189	0.150	0.150	0.001
40	0.179	0.142	0.142	0.001
50	0.173	0.137	0,137	0.001
60	0.167	0.133	0.133	0.001
70	0.162	0.129	0,129	0.001
80	0.158	0.125	0,125	0,001
90	0,154	0,122	0,122	0.001
100	0.150	0.119	0.119	0.001

Although the standard thickness of LiD powder is 1 cm, the energy absorption calculations are only applied to 0.0095 cm at a time[16]. The last column in .

Table 7 indicates that this results in a nearly negligible µx value.

Investigation of Table 6 displays a power-relation between build-up factors as energy changes for a constant µx. Applying the fitted relation, the build-up factors are extrapolated and shown in Table 8

---

[16] Calculated in section 6.2.3.

Table 8: Extrapolated build-up factors

	µx			
Energy (MeV)	**1**	**2**	**4**	**7**
0.01	6.50	38.31	519.55	5898.02
0.05	4.40	17.24	126.66	815.97
0.1	3.72	12.23	68.96	348.10
0.25	2.98	7.76	30.88	112.89
0.5	2.56	5.66	17.80	52.90
1	2.08	3.75	8.48	18.10
2	1.80	2.72	4.77	8.23
3	1.65	2.33	3.72	5.88

In order to determine the build-up factor for the µx to be used, Wallace (1974) suggests that linear interpolation between known values provides relatively acceptable results. It is also known that the build-up factor for a µx of 0 is 1. It is thus determined that at 10 keV for the width under evaluation, the build-up factor is 1.0165, and at 100 keV, it is 1.00272. The values determined here are based on double interpolation and may therefore not be entirely accurate, since the change in build-up factor at these low-energy regions is clearly not linear in nature. The second approach will therefore be employed in the evaluation of the deposited energy where the linear energy absorption coefficient will be used, as accurately provided by NIST (NIST – Physical Measurement Laboratory, 2014). Overestimation of the energy absorbed in the material is an acceptable approach, since this will decrease the approximation of efficiency, which yields more conservative results.

6.1.2.5 Resulting spectrum

For graphic purposes, the area correction is originally neglected in the first part of this section.

The calculated spectrum, as far as magnitude and distribution throughout energy range is concerned, is thus applied at the source. Attenuation, as described in section 4.3, is then applied for various distances from the source for each photon energy.

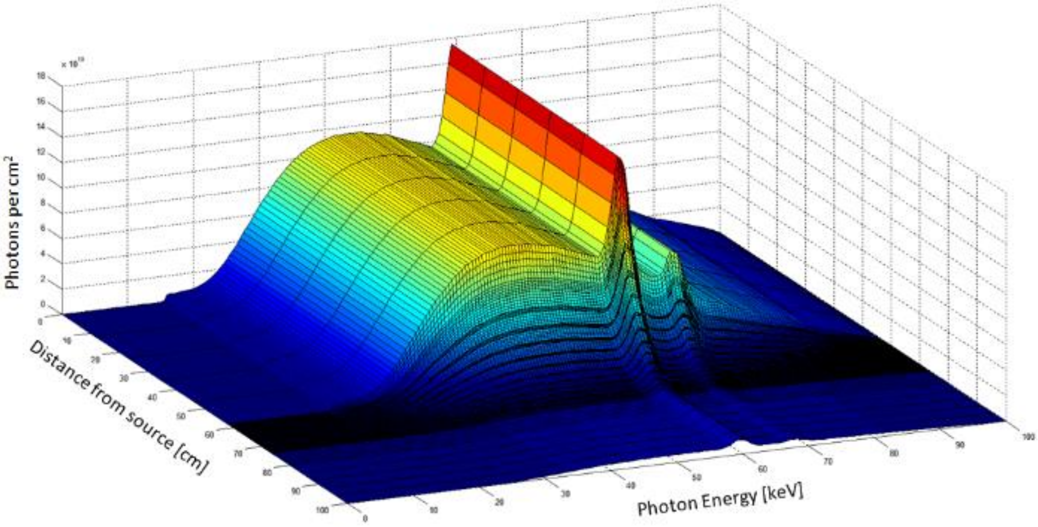

Figure 57: X-ray distribution for Sample 1

Figure 57 shows this distribution. This three-dimensional representation was selected to assist with the visualisation of the effect of attenuation on the entire spectrum as the X-rays travel through the air and the sample. The shape of the spectrum at a distance of 0 cm from the source is identical to the shape that is expressed in Figure 37 at 100 kV, but the magnitude has been adjusted as described in section 6.1.2.3. The spectrum change is very gradual, while the distance from the source is below 58 cm, since the X-rays are only being attenuated by air and this occurs after 76 cm. The resolution for the internal area is greater because it is of greater importance (since this is where the energy deposition is investigated). The dramatic reduction in the magnitude of the spectrum is a result of the X-rays being attenuated by denser materials, such as the Perspex, LiD and CR-39. The sharp reductions (seen as narrow dark bands) are a result of the CR-39, since this material has a greater attenuating effect on the X-rays than the LiD powder. As the X-rays move away from the source, there is a clear flattening of the spectrum and, especially, the hump that is originally visible in the spectrum at 30 keV has been reduced to a plateau. This is a result of the attenuation coefficients varying for X-rays of different energies.

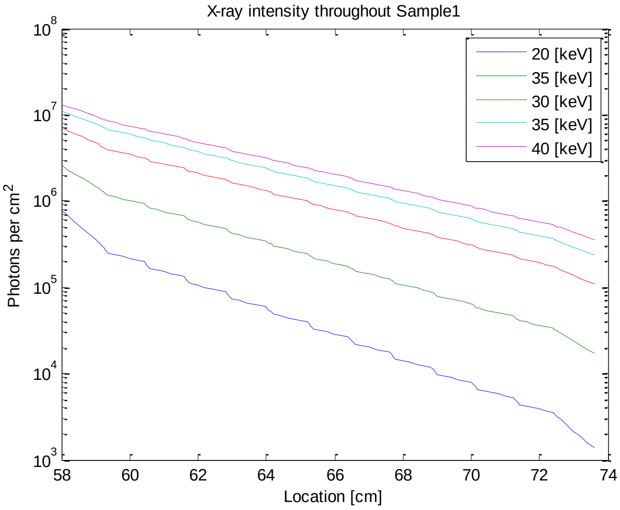

Figure 58: X-ray intensity in Sample 1 for various energies

The X-ray dispersion correction mentioned in section 6.1.2.1 has been made and Figure 58 indicates the resulting distribution. The attenuation through air is disregarded for Figure 58, since it is not being investigated, and the energies shown were selected, since they are near the 30 keV range that is representative of the 100 kV source. As attenuations tend to be more profound at lower energies, investigation of the distribution at 20 keV, for example, shows how the sample composition affects attenuation in the form of steps. These steps are not a function of the calculation, since there are 10 data points between each change in the gradient of the curve. The original and final steep declines occur where the X-rays are being attenuated by the Perspex. The gradual declines occur when the X-rays are attenuated by the LiD and the short, sharp declines occur as the X-rays are attenuated by the CR-39 detectors. The location referred to in the x axis of Figure 58 represents the distance from the X-ray source where the intensity of the indicated photon energy is being investigated. A physical representation of this set-up is shown in Figure 59.

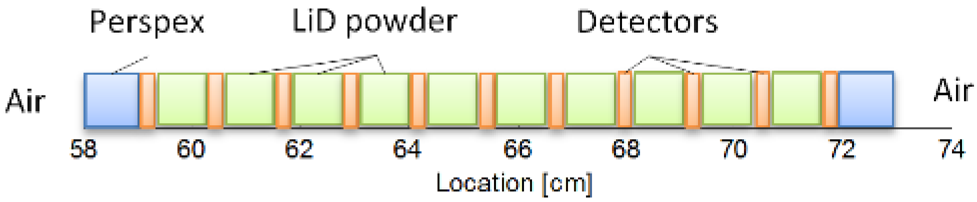

Figure 59: Physical set-up for Figure 58

6.1.2.6 Energy absorbed

The energy absorbed for a particular energy is represented as:

$$E = A \times E_{photon} \int_{x_1}^{x_2} I_0 A(x) B(E,t) S(x)(1 - e^{\mu x}) \cdot dx \qquad \{78\}$$

In Equation 78, I_0 is the intensity of the X-rays of the energy in question at the source for this experiment (with the exposure correction mentioned in section 6.1.2.3 already applied), $A(x)$ represents the area correction discussed in section 6.1.2.1, $B(E,t)$ is the build-up factor discussed in section 6.1.2.4, $S(x)$ is the Compton scattering correction discussed in section 6.1.2.2, x_1 and x_2 are distances from the X-ray source and A is the area being irradiated.

$A(x)$ does not vary greatly over $\Delta x = 0.095\text{mm}$ and can therefore be defined as $A(x_1)$. This approach yields slightly conservative results, since it implies that there is slightly more energy available through Δx. Equation 69 can thus be applied to simplify some of the terms so that Equation 79 can be substituted into Equation 78.

$$I_0 A(x) \approx I_0 A(x_1) = I(x_1) \qquad \{79\}$$

$B(E,t)$ has been determined, but not accurately, and therefore the decision is made to set $B(E, 0.0095) = 1$. In order to ensure that the energy in the sample is not underestimated, μ is used as the linear energy absorption coefficient.

Similar to $A(x)$, $S(x)$ is defined greatly by geometry. Consequently, the assumption can be made that $S(x) \approx S(x_1)$, as conservative results are yielded before this. Section 6.1.2.2 also shows that it may be assumed that $S(x) \approx 1$. The application of all these assumptions on Equation 78 yields Equation 80.

$$E = A \times E_{photon} \int_{x_1}^{x_2} I(x_1)(1 - e^{\mu x}) \cdot dx \qquad \{80\}$$

The total energy absorbed by the LiD powder is, however, being examined and the energy absorbed at all X-ray energy levels must be considered. This results in the application of Equation 81 for the total photon energy absorbed.

$$E = A \int_{E_1}^{E_2} E_{photon} \left(\int_{x_1}^{x_2} I(x_1)(1 - e^{\mu x}) \cdot dx \right) \cdot dE \qquad \{81\}$$

6.1.3 Conclusions

The theory discussed provides an accurate method of determining X-ray intensity throughout the sample. The energy deposition can be determined through integrals, as described in Equation 80 and Equation 81.

6.2 Tracks

6.2.1 Introduction

The α particles released by the molecular-nuclear transition, as described by Equation 1, will be used to determine if the reaction took place. Practically, if α particles that satisfy the criterion of being produced, as described by Equation 1, are detected, then causality indicates that the reaction took place. The detection of α particles in this study is done by the use of CR-39 track detectors, where the identification of particles is done by studying the track left by the particle in the detector. The identification of fusion reactions thus relies on the identification of the particles released by the fusion reaction under investigation. This is done by studying the damage left by particles in the CR-39 matrix.

6.2.2 Calibration

To calibrate the measured energies to energies of the environment in the control group, a list of general alpha-emitting decay schemes are shown in Table 9. These natural α sources must be identified since they will cause tracks in the detectors. By considering these natural sources, a means of identifying tracks left by α particles produced by the fusion reaction in the Li-6D crystals can be devised.

Table 9: Natural α sources

Source	**Energy [MeV]**
Ra-226	4.78
Rn-222	5.49
Po-218	6
Po-214	7.68
Po-210	5.3
$\boldsymbol{n + Li}$**-6**	4.783

The last source is not generally relevant in standard areas. However, the operation of the SAFARI-1 research reactor at NECSA may be responsible for the production of neutrons that may indeed react[17] with the Li in the LiD. This means that although particles produced by this reaction do not generally occur naturally, they should be expected to occur in the experiment.

For the purpose of analysis, some of these energies are simulated using TRACKTEST (Nikezic, 2005). This software provides a means of visualising the tracks that α particles will make. It is noted in Appendix A that track detector variations and the conditions they are etched in have profound effects on the resulting tracks. This data should thus not be used as a direct calibration, but rather as a general impression of the expected tracks.

---

[17] This is since the effective cross-section for Li-6 for thermal neutron capture is very high ($\sigma = 900b$) and the background in the laboratory may thus be sufficient. (Belyaev, Motovilov, Miller, Sermyagin, Kuznetzov, Sobolev & Vasiliev, 2001).

All the tracks produced in this section are computationally modelled through an etching process using a $6.25\frac{mol}{l}$ solution of NaOH at 70 °C for eight hours.

Figure 60 is an example of the output of the TRACKTEST software. The display firstly indicates the depth of the track into the detector material measured in micrometres. This is represented in the image in the vertical axis. The major and minor "axes" that are referred to next are the diameters of the track oval that would be visible if the detector is observed from a position perpendicular to the detection surface. These are also measured in micrometres. Both the oval and the track shape into the detector are displayed in the visualisation. The space between the dotted horizontal line and the solid horizontal line is the detector surface that has been removed due to the bulk etching of the detector material, as discussed in section 4.2.2.2. The nearly vertical line that passes through the oval from the dotted line represents the actual depth of the track that was originally made by the α particle. A flaw with TRACKTEST is that if the track is under-etched (in other words the actual track extends past the etched track), the line still ends at the etched track. For each simulation, the α particle that made the track is shown in the figure heading. Descriptions of what the visual results would be are based on the use of an optical microscope to study the track detectors, where the light from the light source passes from the one side of the detector to the other, where the lenses are.

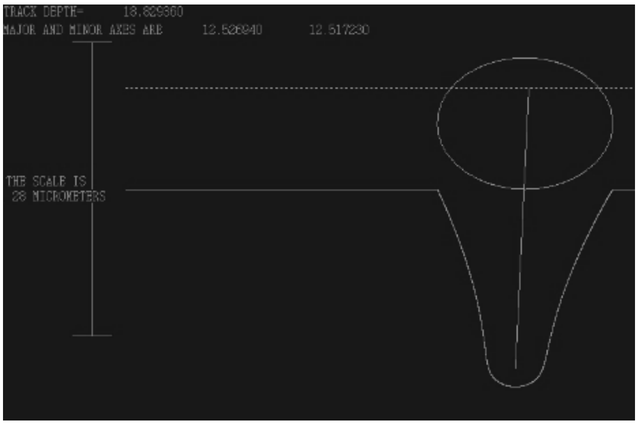

```
TRACK DEPTH=        18.829360
MAJOR AND MINOR AXES ARE        12.526940        12.517230
```

Figure 60: Simulation for 4.78 MeV

Figure 60 shows that the etched track depth is greater than the original track depth and the result is a rounding of the tip. This would be seen as a very dark hole (due to the steep gradient of the sides of the track) with a prick of light at the very centre (since the rounded tip would act as a lens). This would be the easiest track to characterise and any track with an axis greater than 12.5 μm would not even be considered when analysing the surface of the detectors. The reason for this restriction is that, as described in section 4.2.2.2, larger diameters could only be formed by α particles that have less energy. Since α particles of 4.78 MeV can be produced naturally, these and α particles with lower energies should not be considered when attempting to identify α particles that occur as a result of fusion.

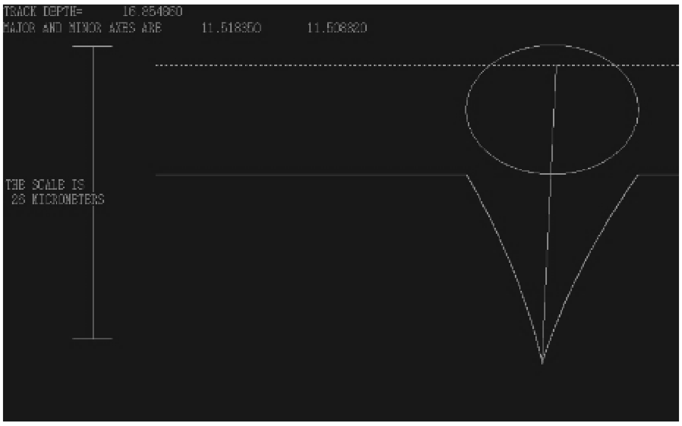

Figure 61: Simulation for 5.49 MeV

Figure 61 is produced by the application of a more energetic α particle, as produced by Rn-222. In this instance, it can be observed that the tip at the end of the track is not rounded. Consequently, there will not be a light spot in the centre of the track. The walls of the etched track are steep and when observed, it will simply appear as a dark spot.

Figure 62: Simulation of 6 MeV

Figure 62 is derived as being formed by an α particle that is produced by Po-218 and would be seen as a completely dark spot, similar to Figure 61. The diameters of the holes are, however, dissimilar, and this could be used to differentiate between the tracks. The implication is that the track diameter can be used to identify the energy of the α particle that produced the track.

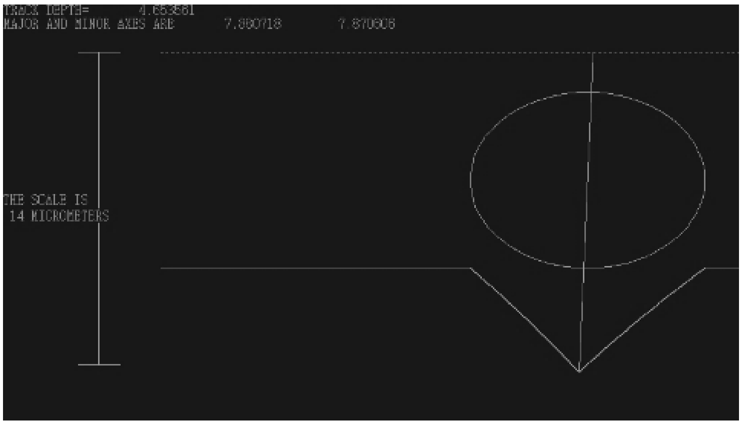

```
TRACK DEPTH=        4.653561
MAJOR AND MINOR AXES ARE      7.860718        7.870606
```

Figure 63: Simulation of 7.68 MeV

Figure 63 is produced by using an α particle that was emitted by Po-214. The first thing that should be noticed is that the track is very shallow. Secondly, the sides of the track wall are less steep than those of the previous examples. Since the track shape is not concave, there will be no lensing effect. Nevertheless, the track will be less dark than those illustrated in Figure 61 and Figure 62 and, consequently, it would display as a dark grey spot instead of a black spot on the surface of the detector.

```
TRACK DEPTH-        1.150745
MAJOR AND MINOR AXES ARE      4.342507        4.328052
```

Figure 64: Simulation of 10 MeV

Figure 64 shows a very shallow track, and these tracks are generally quite light. Unlike very low energies that also have a shallow track, as shown in Figure 65, there is no lensing effect, so the track should be darker than the material surface and not lighter. Although TRACKTEST cannot analyse higher energies, it is simple to extrapolate the physical characteristics.

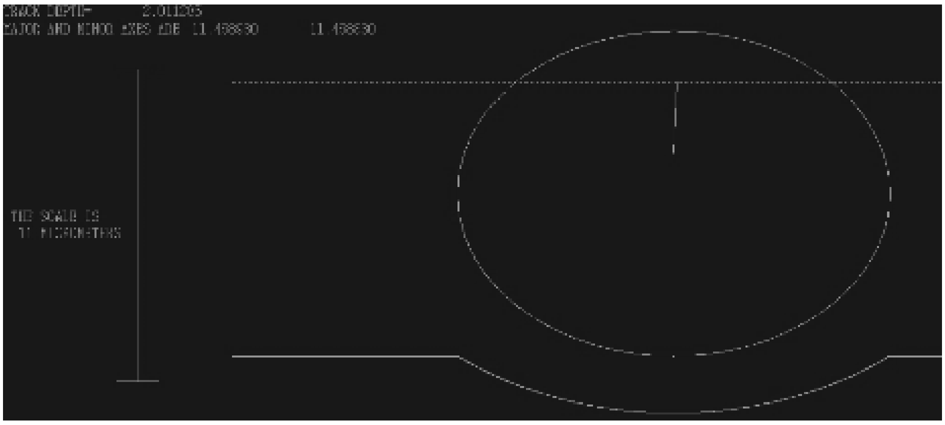

Figure 65: Simulation of 0.5 MeV

Figure 65 shows the track produced by a low-energy α particle. The depth of the track is similar to that illustrated by Figure 64. However, there is a very clear difference in the size of the track diameters. The concave nature of the track is also clear from this example, and this track would appear as a light spot with a slight ring around it when observed through a microscope.

6.2.3 Limitations

The α particles lose energy as they travel towards the detector surfaces, since there are material obstacles in the way. Therefore, only the sources on the surface will produce particles with the exact energy indicated.

However, the only detector that was exposed to air is the control detector, since the detectors that formed part of the experiment were prepared in an anaerobic environment and were effectively shielded from all but the Li-6 α source.

Since the highest α energy that should be observed during the course of the experiment is 4.783 MeV if there is no $LiD \rightarrow Be$ reaction, it is safe to assume that any track that indicates a higher-energy α particle is an indication of a successful fusion in the crystal. These reactions may be attenuated even further and could be detected as even lower energy tracks, but this cannot be considered as definitive evidence due to the presence of other reactions.

Thus, it was decided to define a track that indicates a successful transition as one that was produced by an α particle with an energy between 5 and 12 MeV. This translates to any completely dark or grey track with a diameter of less than 11.5 μm.

This can, in turn, be used to determine the depth into the LiD from where detectable α particles could be produced.

The first step is to calculate the distance that an α particle could travel before being reduced to the target energy. This can be done using Figure 66.

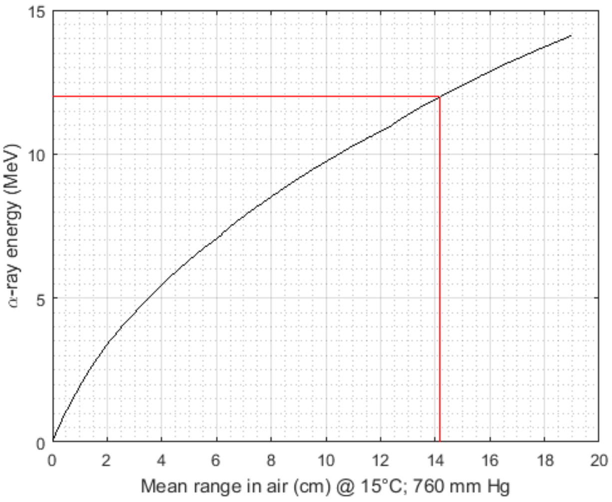

Figure 66: Range of α particles as a function of energy in air. Adapted from: (Lamarsh & Baratta, 2012)

The range in air is about 14.2 cm, but this leaves the particle with no kinetic energy. For higher-energy α particles, the relation between particle energy and the distance that can be travelled through air seems to be approximately linear[18]. Assuming that the relation to the distance travelled and the energy lost for high energies is relatively linear, it can be argued that a linearised relation between particle energy and distance travelled in air can be considered as shown in Equation 82.

$$E_{new} = \left(1 - \frac{d_{travelled}}{d_{max}}\right) \cdot E_{original} \qquad \{82\}$$

Thus, the distance travelled in air before the energy of the particle, which started with 12 MeV, is 5 MeV after 7.832 cm.

Furthermore, the relative stopping power can be determined using the Bragg-Kleeman rule, specifically for air as shown in Equation 83.

$$\frac{Ra}{R} = 3\,100 \cdot \frac{\rho}{\sqrt{M}}, \qquad \{83\}$$

where the root of the molar mass for use in Equation 83 is described by Equation 84.

$$\sqrt{M} = \sum \gamma_i \sqrt{M_i} \qquad \{84\}$$

In Equation 78, γ_i is the mass percentage of a particular element or isotope and M_i is the molecular mass of that element or isotope. The present isotopes for LiD are displayed in Table 10.

Table 10: LiD composition

Isotope	**Atomic percentage**
Li-6	7.59
Li-7	92.41
H-1	2
H-2	98

---

[18] Applying a linear fit to data between 5 MeV and 12 MeV for Figure 66 yields an average error of 3%.

With CO_2 present, as in the spaces between the crystals for the set-up, $\sqrt{M}$ is calculated as 2.989 and the density of the mixture is $0.794\frac{g}{cm^3}$. This produces a relative stopping power of 823.58.

Finally, Equation 79 can be applied and the furthest point in the sample that can be measured with confidence is at a depth of 0.095 mm from the detector surface. These are, however, only for particles that enter perpendicular to the track surface.

An analysis where TRACKTEST is used to simulate particles that do not enter perpendicular to the detector shows that the detection of tracks at other angles is relatively limited. As before, the figure heading indicates the α particle energy. This time, the incident angle is also included.

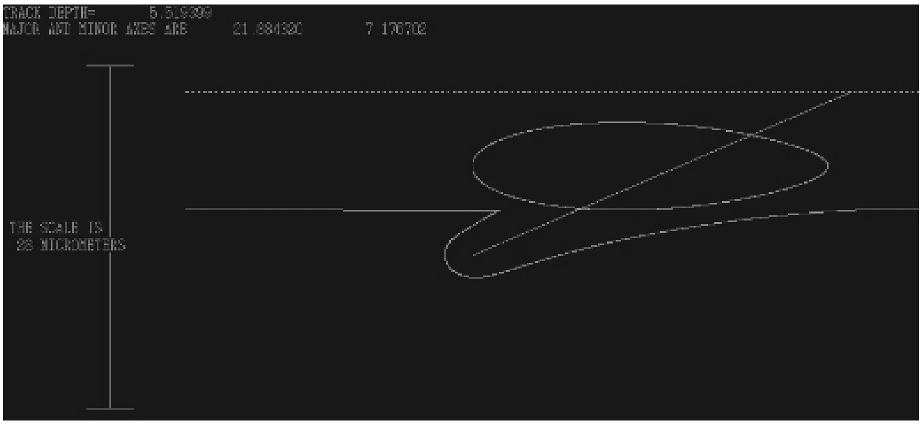

```
TRACK DEPTH=        5.519399
MAJOR AND MINOR AXES ARE      21.884320         7.176702
```

Figure 67: 4.783 MeV track at 30°

Figure 67 shows that the track tip is concave for lower energies, as described in Figure 60 for the same energy. The main difference is that the light spot is less visible since there is still some detector matrix above the tip. Physically, such a track would look like an elongated oval with a blunt tail. However, for higher energies, as in Figure 68, the tracks become very difficult to detect.

```
TRACK DEPTH=        2.016857
MAJOR AND MINOR AXES ARE      11.425380         4.557426
```

Figure 68: 7 MeV track at 45°

The depth of the track in Figure 68 is very low and the result will be a slightly grey elongated oval.
Analysis indicates that tracks with energies down to 10 MeV are only detectable within 10° of the perpendicular. Tracks with energies down to 7 MeV are detectable within 45° and lower energy

tracks are detectable within 60°. The problem is that the light from the tip is no longer visible, which makes it difficult to differentiate between positive events and calibration tracks.

Due to the dynamics of track etching, the detection efficiency decreases as the particle energy increases, since fewer particles damage the detector enough to etch tracks faster than the bulk etching rate. As the source moves away from the detector, the range of identifiable events also decreases due to the energy lost through the material. The fact that each reaction produces two α particles that move away from one another means that, effectively, 180° needs to be considered. For a particle within a detectable range, the etching efficiency as defined is 39.068%.

6.2.4 Conclusions

Several tracks should be visible on the detector surface due to particles that are not α particles. However, they are easily differentiable from α particle tracks. Only purely dark tracks can indicate positive events, but dark tracks with small bright spots in the centre can be used for calibration purposes. Considering energy loss and etching factors, only 40% of the event tracks[19] within 0.095 mm will show for the active depth of the material. It is reiterated that 100% certainty of α particles resulting from the fusion reaction being investigated can only be obtained if two α particles that originated with the same 11.2 MeV are observed to move in separate directions. This is difficult because it requires aligning the detectors on a nearly atomic scale. The experimental set-up also only allows the detection of one of the particles. Therefore, events are detected with a high confidence – but not with certainty.

7. Data

7.1 Tracks

Due to the damage caused by photons, as mentioned in section 4.2.2.2.1, the diameters will differ from those of section 6.2.2. The control slides are thus used to calibrate the diameter types. Using the maximum natural α-source energy of 7.68 MeV, as mentioned in Table 9, the control slides were searched and it was found that the highest energy track still has a light spot in the centre as shown in Figure 69.

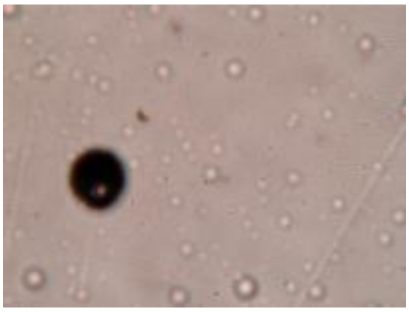

Figure 69: Control track

---

[19] An "event track" refers to a track that has formed from the track left by an α particle that was produced in a fusion reaction.

As expected, several lower energy tracks were also detected on the control surface.

Figure 70: Lower energy tracks

This calibration led to the determination that any track that does not contain a bright circle within it should be considered a positive event.

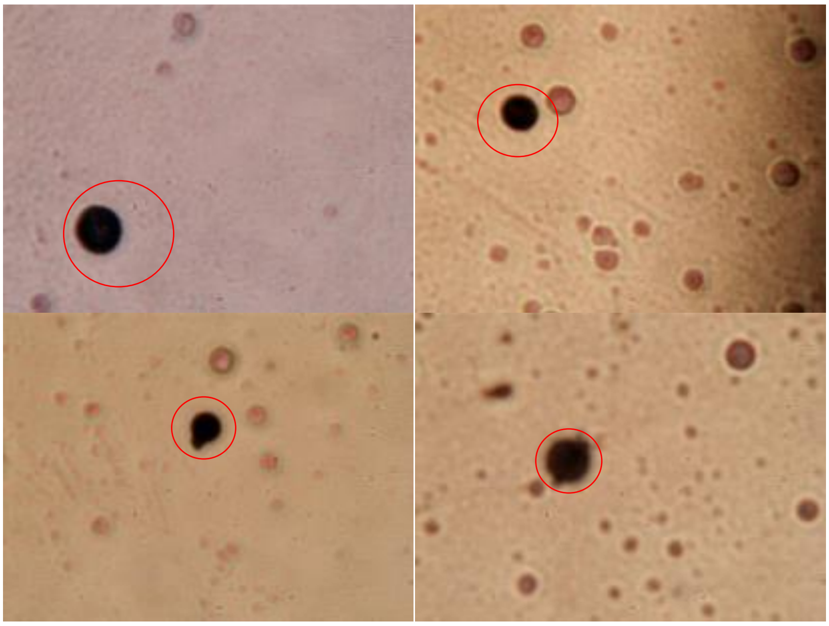

Figure 71: Positive events(In the images show the circled features are considered evidence of fusion events)

The diameters of these tracks were measured in Adobe Photoshop® and the pixel-µm ratio could be determined with a calibration slide, which resulted in accurate measurements.

Throughout the process, some non-events were recorded and borderline[20] events were indicated as such. These are shown in Figure 72.

---

[20] Borderline tracks are defined as tracks that would not be indicative of positive fusion α particles based on the TRACKTEST calibration, but may be considered as positive fusion α particle tracks, since the X-ray exposure has damaged the CR-39 lattice, resulting in a different baseline based on calibration from natural α sources.

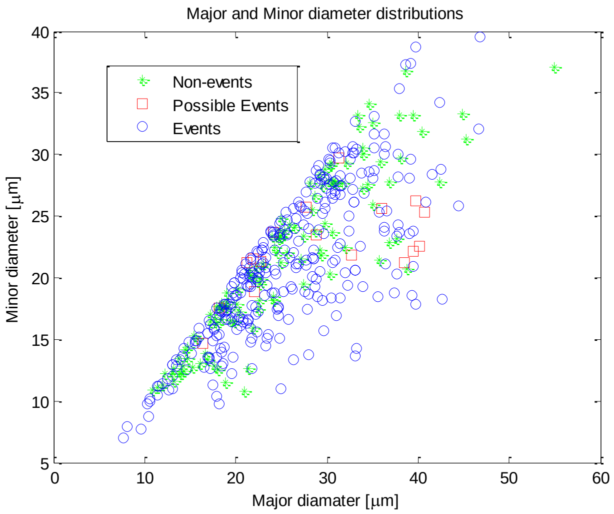

Figure 72: Track size distributions

The equipment that the CR-39 detectors were etched in was not large enough to process all the detectors at the same time. For this reason, the detectors were arbitrarily divided into two groups that would be etched in two separate sessions. The two sessions are also compared to ensure that the etching conditions were similar – allowing results from both sessions to be considered simultaneously.

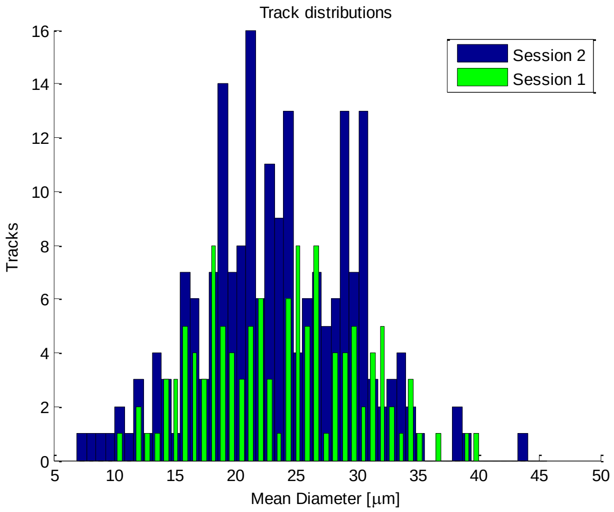

Figure 73: Session comparison

From Figure 73, it can be seen that although there are some outliers, the data from the two sessions is similar. The magnitude of the graph for Session 1 is less, because fewer detectors were etched in the first session and both sessions have mean track diameters mainly between 11 and 35 micrometres.

7.2 Results

The physical properties of the experimental set-up for all the samples are not the same. The reader is referred to section 5.1.3 for clarification should there be confusion. The naming convention is described in Figure 74 and Figure 75.

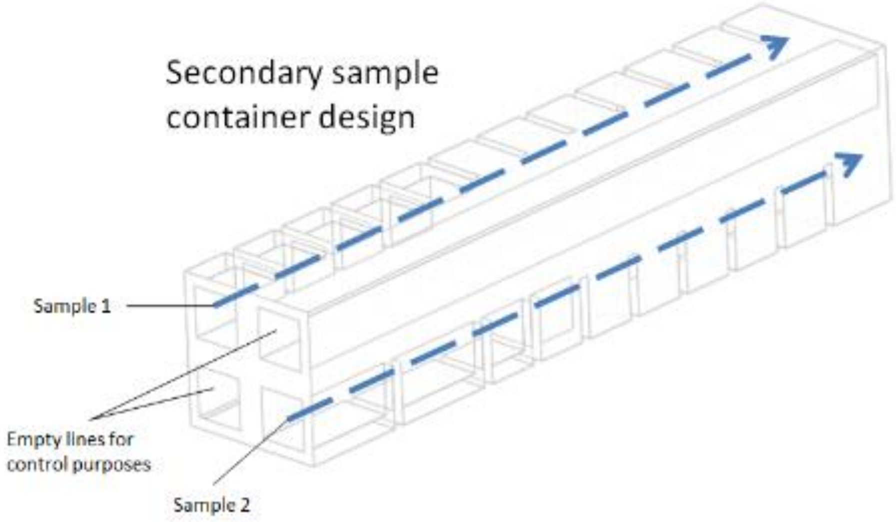

Figure 74: Definition for Sample 1 and Sample 2

Figure 74 shows that samples 1 and 2 will refer to the two lines with LiD powder/detector configurations that are in the second container design. All the powder containers for Sample 1 are 1 cm in length, whereas Sample 2 has two chambers with a length of 2 cm of LiD powder.

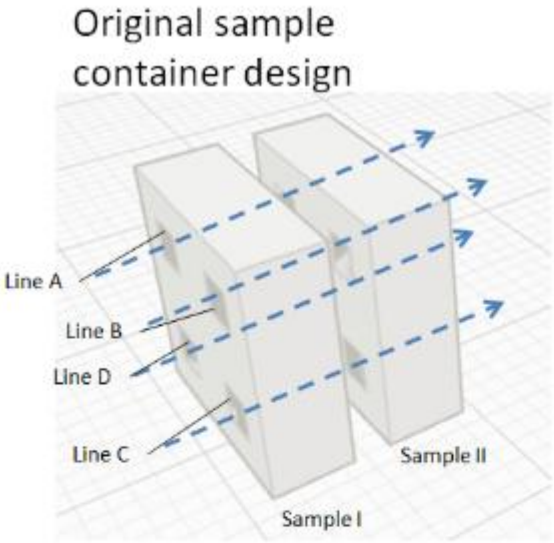

Figure 75: Definition for Sample 1, Sample 2 and lines A to D

Figure 75 indicates that the rest of the powder was placed in two containers of the original design that have been placed behind one another. Lines A to D are thus used to describe the lines that are composed of LiD powder/detector configurations.

Neither Figure 74 nor Figure 75 displays the container lids in order to facilitate easier visualisation of the configurations.

7.2.1 Sample 1

The total energy absorbed in the active zones for Sample 1 is shown in Figure 76, where the entire spectrum of energy being absorbed is considered relevant. The trend is logarithmic considering that the energy absorbed, as calculated by Equation 75, has a logarithmic nature.

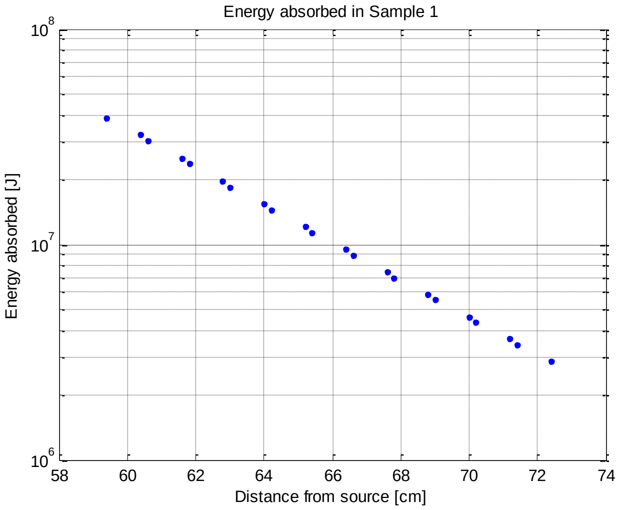

Figure 76: Energy absorbed in active zones (Sample 1)

It is thus simple to assume that the energy absorbed through the material will follow the trend regardless of the specific photon energies being investigated. The active zones, as described in Figure 76, refer to the areas in the specific line where α particles produced by fusion can be measured. These zones are generally on either side of the detectors. The first dot in Figure 76 is the first active zone (just after the first detector) and the last dot is the active zone just before the last detector. The gap between dots that are close together is filled by CR-39 track detectors, whereas the larger gaps are filled with LiD powder.

Analysis is done on the total photon energy absorbed in all of the active areas for the different energy ranges, so that this may be compared to the energy produced, as suggested by the tracks.

Table 11: Total energy absorbed for various photon energies in Sample 1

Range			
E_{min} [keV]	**E_{max} [keV]**	**Range width**	**Energy absorbed [MJ]**
1	100	99	305.7
20	40	20	53.9
25	35	10	25.6
29	31	2	5.1
30	31	1	2.8
29	30	1	2.3

ested by the tracks.

Table 11 indicates the energy absorbed by active zones, so in order to consider the efficiency of the system, the energy produced must also be analysed. A comparison can then be made between the energy input and the energy output of the active zones.

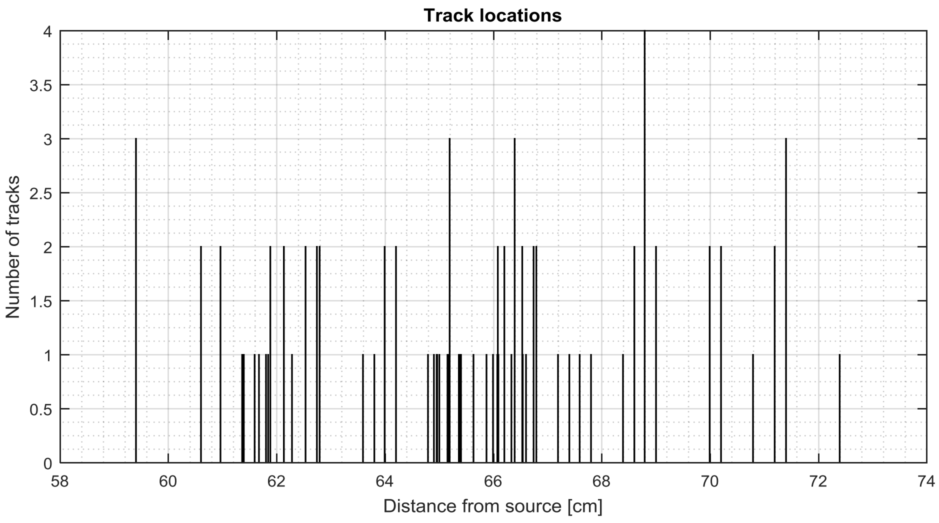

Figure 77: Track counts

In order to determine the energy output, the number of tracks per detector is graphed in relation to the energy absorbed by LiD in that area, and is shown in Figure 78. The energy produced is determined by considering that each track represents 22.372 MeV, and simply converting that to joules.

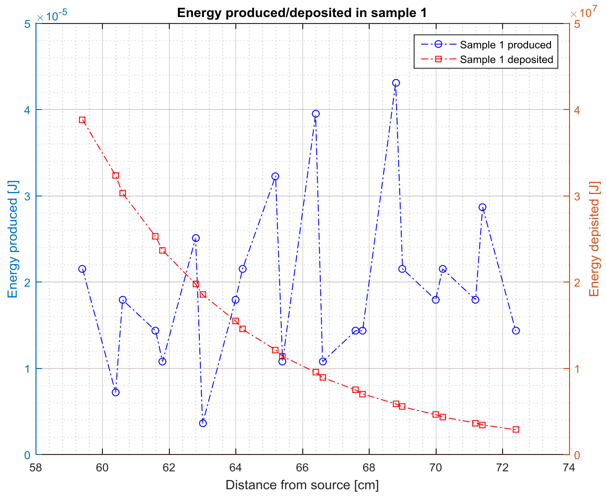

Figure 78: Energy absorbed or produced in Sample 1

Figure 78 is a superposition of Figure 77 and was developed to assist in analysis. It is difficult to draw a correlation between the energy deposited and the locations where fusion reactions took place for Sample 1.

7.2.2 Sample 2

Since the set-up of Sample 2 is different to that of Sample 1, the distribution of X-rays is different and selected energies are shown in Figure 79.

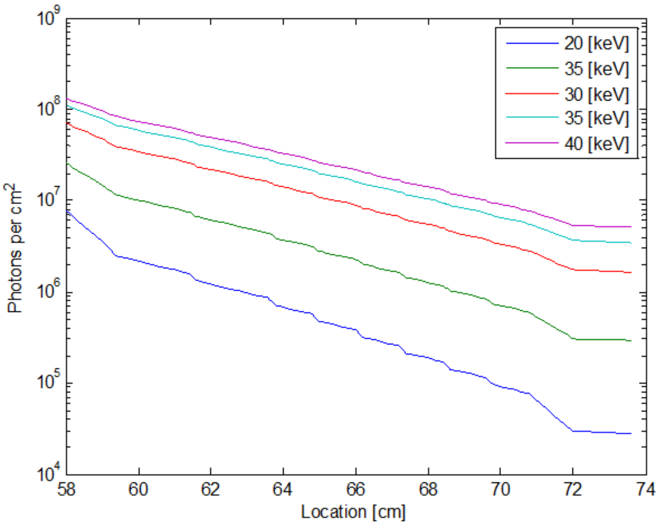

Figure 79: X-ray intensity through Sample 2 for various energies

A comparison of Figure 79 and Figure 58 shows that the main difference between the shapes of the graphs occurs before a distance of 64 cm from the X-ray source. The physical reason for this difference is shown in Figure 74, which indicates that the first two powder chambers of Sample 2 are longer than those of Sample 1. The result is two long (2 cm) gradual steps where the X-rays are attenuated by LiD, followed by 1 cm steps between detectors. The location referred to in the x axis is the distance from the X-ray source.

Table 12: Total energy absorbed for various photon energies for Sample 2

Range			
E_{min} [keV]	**E_{max} [keV]**	**Range width**	**Energy absorbed [MJ]**
1	100	99	216.3
20	40	20	38.4
25	35	10	18.3
29	31	2	3.6
30	31	1	2.0
29	30	1	1.7

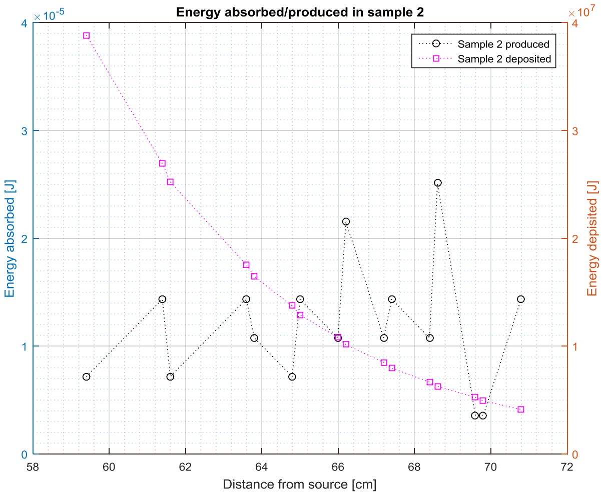

Figure 80: Energy absorbed or produced in Sample 2

Figure 80 shows results similar to Figure 78, which indicates that there may not be a direct correlation between the position where energy is deposited and where fusion reactions occur for Sample 2. The energy deposited is calculated using Equation 75.

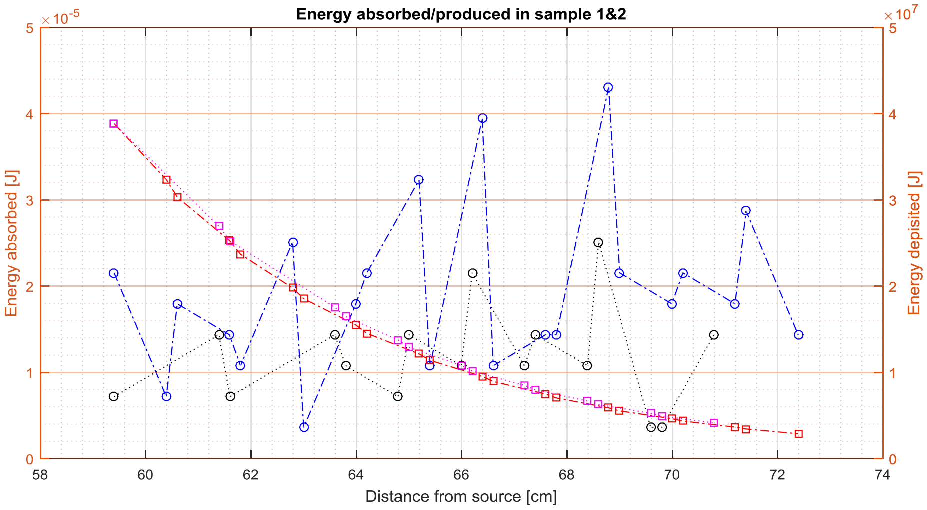

Figure 81: Energy absorbed or produced in samples 1 and 2

When superimposing the comparisons for both samples 1 and 2, the deposited energy matches closely, as expected. They cannot be identical because the physical layout of Sample 1 is not identical to the physical layout of Sample 2. Both track energies vary, but seem to follow a general increasing trend, as the distance from the source increases.

7.2.3 Sample 2A

The energy for line A is shown in Figure 82 and follows the general stepwise function where LiD exists as expected. It should be noted that, unlike samples 1 and 2, the configurations represented by lines A to D do not contain 1 cm of LiD between detectors and that the steps in the X-ray intensity graphs are more frequent.

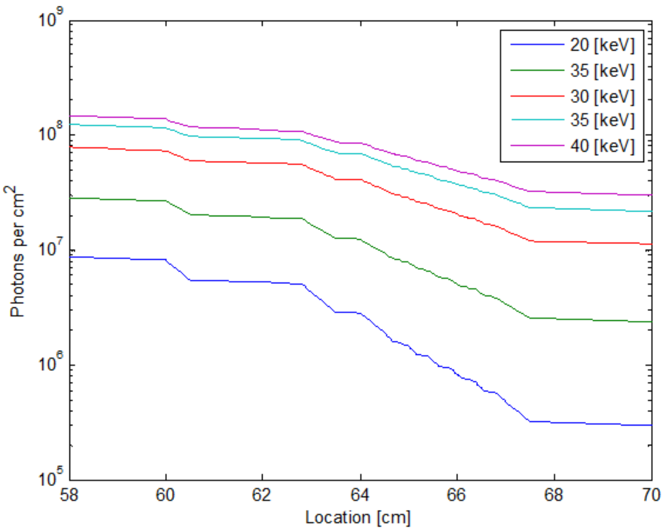

Figure 82: X-ray intensity through line A

The original lack of steps, as observed in Figure 82, is a result of line A being empty in Sample 1, which occurred because the tolerance in that sample container was insufficient and could not be filled with the detector/powder configuration. As a result, two sharp steps occur due to the attenuation of the X-rays by the Perspex, with a gradual CO_2 attenuation between them. Sample 2 begins at a distance of about 64 cm from the X-ray source.

When comparing the total energy absorbed for the letter lines[21], it is generally greater than that of the number lines. This occurs because the area of exposed material is greater (1 cm^2 instead of 0.9025 cm^2).

Table 13: Total energy absorbed for various photon energies for line A

Range			
E_{min} [keV]	**E_{max} [keV]**	**Range width**	**Energy absorbed [MJ]**
1	100	99	253.9
20	40	20	45.3
25	35	10	21.5
29	31	2	4.3
30	31	1	2.3
29	30	1	2.0

---

[21] Letter lines refer to lines numbered by letters such as A, B, C and D, whereas number -lines refer to Sample 1 or Sample 2, as described in Figure 74 and Figure 75.

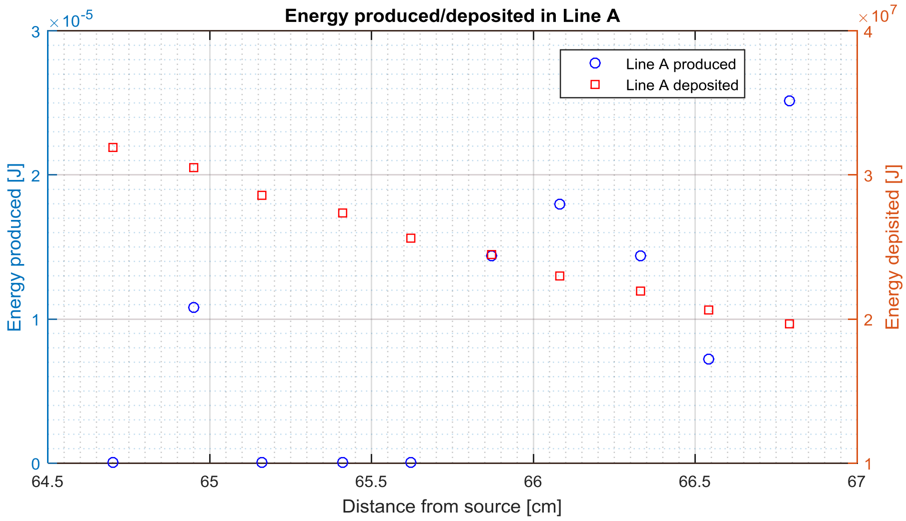

Figure 83: Energy absorbed or produced in line A

As expected, Figure 83 shows no produced energy in the first area where there is no material powder. Once again, the tracks seem to be more pronounced further away from the source.

7.2.4 Sample 1B and 2B

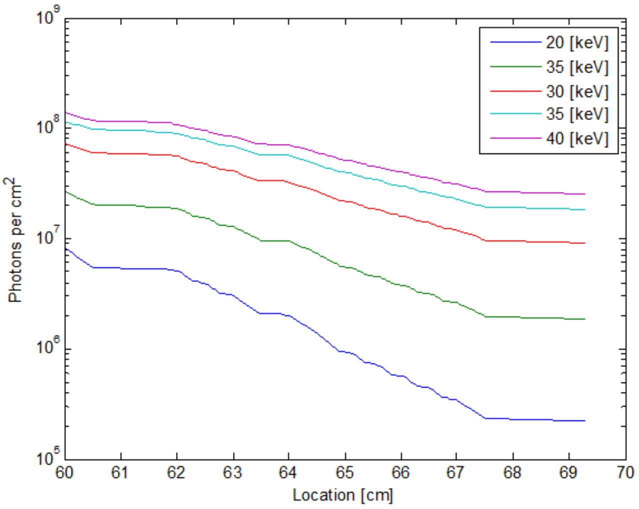

Figure 84: X-ray intensity through line B

Figure 84 indicates that initially line B in Sample 1 has an empty area similar to that of line A. Unlike line A, a portion of line B contains the powder/detector configuration. As a calibration, there are several detectors without LiD powder in between at the start of line B in Sample 2. This can be seen because the sharp decline between 64 cm and 65 cm from the X-ray source is longer than that produced by the 0.5 cm Perspex lid.

Table 14: Total energy absorbed for various photon energies for line B

Range			
E_{min} [keV]	E_{max} [keV]	Range width	Energy absorbed [MJ]
1	100	99	362.5
20	40	20	68.2
25	35	10	32.9
29	31	2	6.6
30	31	1	3.6
29	30	1	3.0

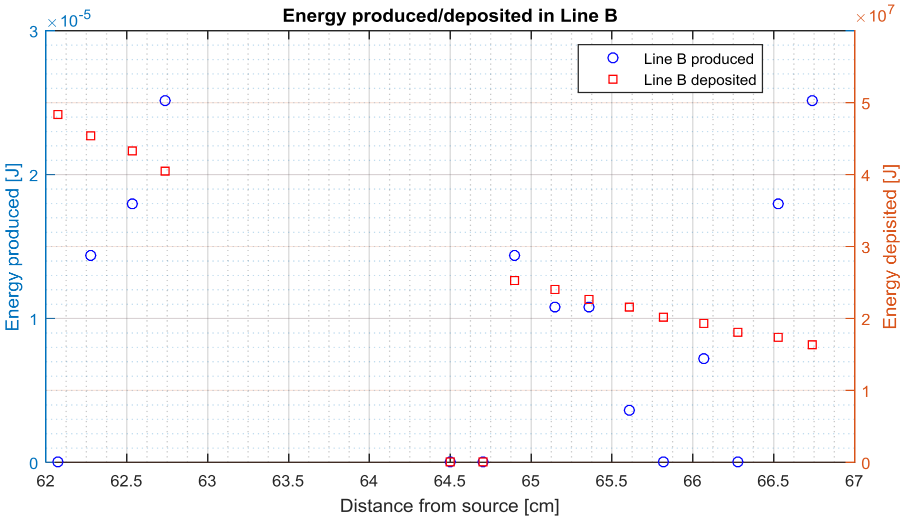

Figure 85: Energy absorbed/produced in line B

Figure 85 shows the locations between 64 and 65 cm where detectors were present as a calibration measure and that no fusion-produced α particles were detected there.

7.2.5 Sample 1C and 2C

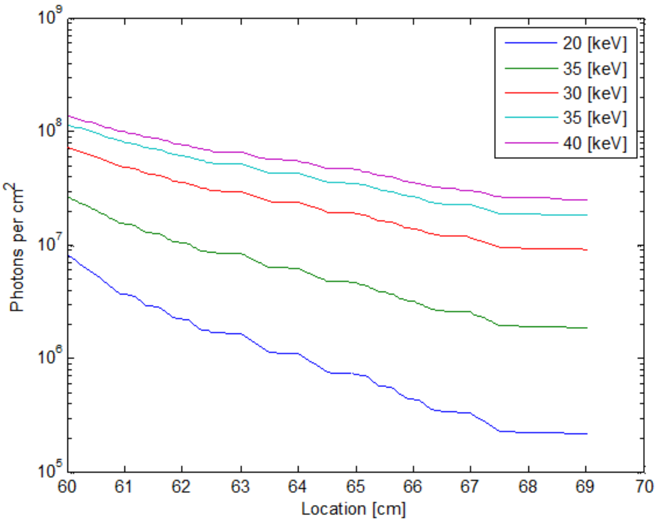

Figure 86: X-ray intensity through line C

Figure 86 shows that line C was completely filled with the powder/detector configuration in both samples 1 and 2.

Table 15: Total energy absorbed for various photon energies for line C

Range			
E_{min} [keV]	E_{max} [keV]	Range width	Energy absorbed [MJ]
1	100	99	436.7
20	40	20	81.5
25	35	10	39.2
29	31	2	7.9
30	31	1	4.3
29	30	1	3.6

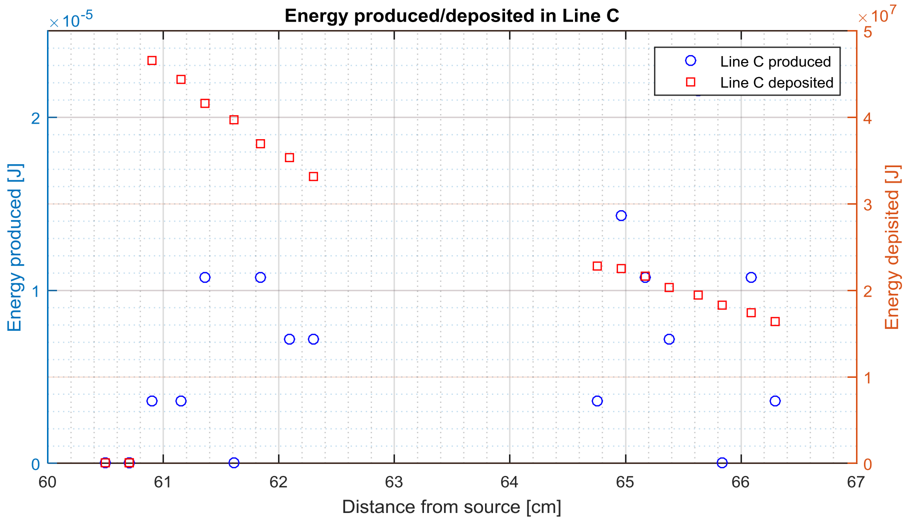

Figure 87: Energy absorbed/produced in line C

7.2.6 Sample 1D

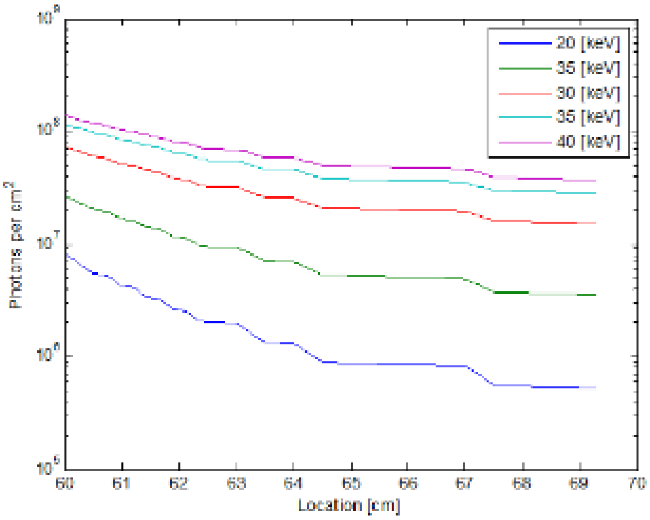

Figure 88: X-ray intensity through line D

Figure 88 indicates that Sample 2 was empty in line D. Therefore, the step pattern associated with the powder/detector configuration is not present.

Table 16: Total energy absorbed for various photon energies for line D

Range			
E_{min} [keV]	E_{max} [keV]	Range width	Energy absorbed [MJ]
1	100	99	333.5
20	40	20	67.6
25	35	10	33.2
29	31	2	6.7
30	31	1	3.6
29	30	1	3.1

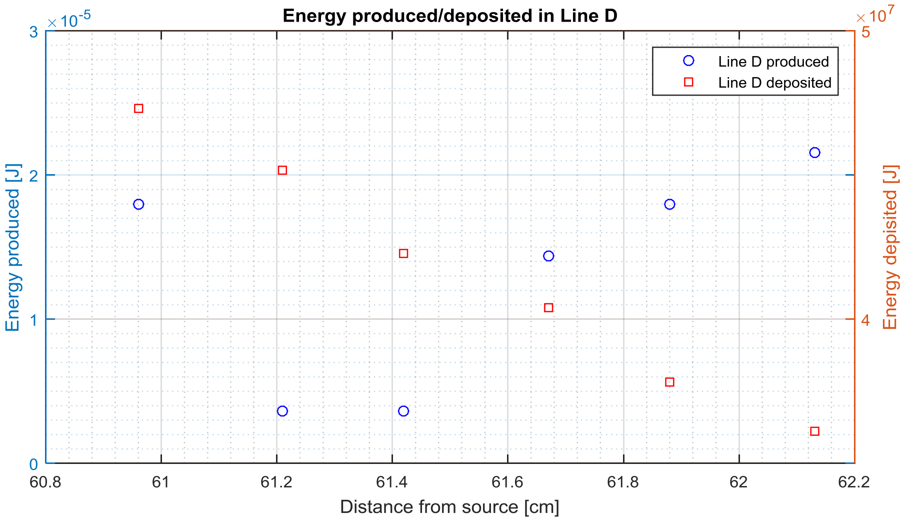

Figure 89: Energy absorbed/produced in line D

7.2.7 Summary

As far as the distance from the source is concerned, there is no clear relation between the energy absorbed and the energy produced. Combining all the results and comparing the deposited energy directly to the energy produced as in Figure 90 does, however, allow for a level of analysis.

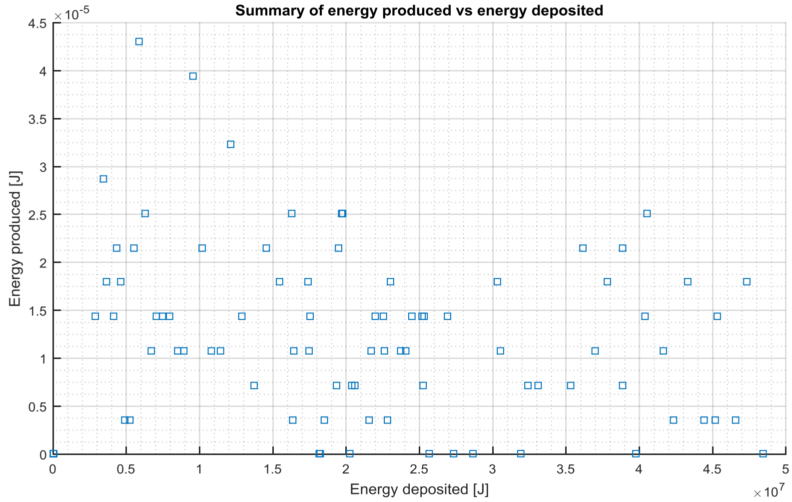

Figure 90: Summary of results (Energy deposited is representative of a case where all photon energies are of interest)

Although the data is incoherent, it is clear that the energy produced seems to decrease as the deposited energy increases. The most logical explanation would be that, in the cases where a lot of energy is produced, additional energy might disturb states where resonance would have occurred. However, in situations where there are fewer photons, this type of interference does not take place.

Table 17: Energy comparison

Range		**Energy absorbed [J]**	**Energy produced [MJ]**
E_{min} [keV]	**E_{max} [keV]**		
1	100	1.909E+09	1.048E-03
20	40	3.549E+08	
25	35	1.707E+08	
29	31	3.421E+07	
30	31	1.859E+07	
29	30	1.562E+07	

The energies absorbed and produced are summed and shown in Table 17 for comparative purposes. It is clear that the energy produced does not begin to compare with the energy absorbed, not to mention the energy provided by the X-ray source. The total energy produced can be corrected for the lack of detector efficiency, as well as the Li-6D enrichment of the LiD powder and the resulting total energy produced would be 3.606×10^{-2}J. This is still at least an order of 10^{9} smaller than the energy deposited into the system.

7.2.8 Conclusions

Based on comparison between the tracks observed on the control detectors and those exposed to LiD; the determination is made that the experimental set-up was successful in limiting environmental exposure as evidenced in the relative low number of environmental tracks observed on the experimental detectors. Additionally the type of tracks that were deemed to be possible fusion events were not observed on the environmental detectors, adding to the credibility of tracks deemed to be indicative of fusion reactions. The sizes of the positive tracks as measured from the two separate etching groups are similar, adding confidence to the etching process. Overall it is difficult to determine a correlation between the energy deposited and produced in each individual sample, however a loose correlation may be inferred as discussed in section 7.2.7. Finally the data would seem to indicate that far more energy is used than is absorbed in this process.

8. Discussion

8.1 Reaction rate based on incoming X-ray energy

The nature of the results makes it difficult to draw any conclusion about the specific energy required for the process to take place. As indicated in Figure 90, the process seems to occur more readily when there is less energy available. The reason for there being less energy available is that much of the energy has already been deposited up to this point. As described when discussing attenuation, the total energy available is less the further the spectrum travels, however the average energy of the photons in the spectrum is higher. From this, one could conclude that higher photon energies more readily accelerate the reaction rate. However, this may also be coincidental. The physical explanation for this is that the lower-energy photons excite the atom in the lattice enough to make it a more difficult target for the rest of the photons to hit, but not enough for fusion to occur.

8.2 Power required or produced

The power absorbed far outweighs the power produced by the reactions. Even if all the inefficiencies of X-ray production, X-ray spread, attenuation, correct photon energy, material enrichment and energy conversion efficiency are removed, the system is still not remotely viable for energy production. It must be noted that this technical design is for the detection of fusion events, and not for energy production. As alluded to before in this study there may be a specific wavelength that preferentially promotes fusion. Determining this wavelength and then using a synchrotron source rather than X-ray Bremsstrahlung may also prove useful, especially if the fuel is compressed and refined.

8.3 Fusion in crystals

A total of 88 positive tracks, which indicated 88 reactions, were recorded. The total exposure time was 111.466 hours, which means that the reaction rate was $2.193 \times 10^{-4}\, s^{-1}$ or that a reaction occurred every 1.2666 hours (every 4.56×10^{3} seconds). The number of atoms involved must, however, also be considered to produce meaningful results. The active depth was always $9.509 \times 10^{-3}\, cm$, where the powder was in contact with 85 detector sides. Consequently, the amount of active material is $\left(38 \times (0.95 \times 0.95 \times 9.509 \times 10^{-3})\right) + \left(47 \times (1 \times 1 \times 9.509 \times 10^{-3})\right) = 0.77 cm^{3}$, translating into 0.61 g of powder and thus $4.57 \times 10^{-2}\, g$ of Li-6D. Finally, this equates to 2.74×10^{21} nuclear pairs. Thus, it takes 3.6×10^{17}years per nuclear pair. This lifetime is a reduction of 10^{-2} years compared to the minimum lifetime of 10^{19}years as in Belyaev et al. (2006). Thus, there is a significant increase in reaction rate due to the application of X-rays. From this perspective the experiment was a success in that it has thus shown that fusion in crystals can indeed be used by means of exposure to electromagnetic waves.

8.4 Future work

There are, of course, several improvements that can be made and should be applied to improve this investigation.

- Rays of mono-energetic X-rays should be used to determine the energy that most stimulates the reaction rate. This can be either in the form of characteristic X-rays or synchrotron radiation
- Thinner layers of LiD should be used between CR-39 detector plates to determine double coincidences to validate these results. This is a method that would require precision markings on the detector as well as orientation. Since the reaction produces two α-particles moving at 180˚ away from one-another, determining co-incidence od two such particles may be considered even stronger evidence to suggest that reactions had occurred.
- Lower energy X-rays should be used to investigate the effect of the photon energy on the stimulation of the fusion reaction. This type of experiment would however need to be extremely prolonged. An additional hurdle is that the detectors would need to be close to the source in order to limit attenuation of low energy photons, or the experiment would need to be conducted in a vacuum. Additionally damage to the detectors closest to the X-ray source due to high temperatures is a distinct possibility.
- Different samples should be exposed to X-rays of varying time intervals in order to determine a correlation between reaction rate and exposure time. This type of experiment would require a set of identical samples. These samples may be removed at different points in time at set time intervals (longer than the exposure time used in the experiment quoted in this study). A significant downside to this type of experiment is the time that will need to be invested before any results are available.
- Automation of the analysis of CR-39 detectors should be considered to increase future research speed. There is already software capable of analysis available. Defining rigorous bounds and then running such software will make having more detectors in each experiment more viable.
- A different X-ray source directly attached to the samples would reduce attenuation energy losses through air and the target material. This could be used to produce varying spectra for smaller time intervals, increasing the resolution of the results.
- An X-ray source with a different anode material could be used to determine the effect of the specific characteristic X-rays on the fusion process. This would be a step in determining a preferential electromagnetic wavelength.
- Should the procedure somehow be found to be viable for energy production, a method of extracting the energy for useful work should be investigated.

9. Conclusions

It is clear from experimental results that the use of X-ray-induced molecular-nuclear transition for power generation by fusion is not recommended, since the reaction rate is still incredibly slow.

The reaction rate is, however, sped up by two orders of magnitude through the introduction of X-rays to the LiD system. As a result, more work should be done to determine the energy that most stimulates the reaction. The experiment was thus consequently a success in showing that electromagnetic radiation such as X-rays can be used to increase the reaction rate of fusion in LiD crystals. The inference is thus that this method may also be used to accelerate fusion reactions in water as described in the literature review.

This experiment could not determine the most effective energy due to incoherent results when investigating that aspect of the reaction. One of the greatest hurdles was that the number of fusion events is extremely low making statistical analysis difficult. Should a similar experimental procedure be followed for a longer period of time this data may be used to make some of the determinations that this study was unable to. The main purpose was to determine if X-rays can be used to increase the fusion reaction rate in crystals, and the other determinations would be made based on that data. (V. B. Belyaev, Miller, Otto, & Rakityansky, 2016) should be consulted in order to determine exposure times that would be required to make the fringe determinations that this study investigated.

Work along the lines of X-ray-induced molecular-nuclear transitions should continue in order to understand the quantum dynamics, and may hold potential for the production of energy. The procedure does, however, hold potential for use as a means of evaluating an experimental cross-section[22] of such reactions at extremely low energies that are not accessible in direct collision experiments.

10. Recommendations

After completion of this study, the following recommendations can be made:

- Much work should be done to increase the understanding of molecular-nuclear transitions on both a theoretical and a physical level.
- Determining the right energy band to amplify the transitions would be valuable for research purposes.
- Some research should be devoted to the exploration of the phenomenon of fusion.
- Similar studies would require greater exposure time or a more powerful X-ray source in order to yield results that may be subjected to statistical analysis

---

[22] Astrophysical S factor

11. References

AMETEK. (2014). Mini-X Miniature X-Ray Tube. Retrieved September 30, 2014, from http://www.amptek.com/products/mini-x-ray-tube/

Beckhoff, B., Kanngießer, B., & Langhoff, N. (2006). *Handbook of practical X-ray fluorescence analysis*. Retrieved from http://books.google.com/books?hl=en&lr=&id=c6d8EPYHn1EC&oi=fnd&pg=PA1&dq=Handbook+of+Practical+X-Ray+Fluorescence+Analysis&ots=Im_jtez3MX&sig=QrYM4pX1cFujrDl9vfBZIIu5Sk8

Belyaev, V. B., & Miller, M. B. (2010). Induced molecular–nuclear transitions in water and some other molecules. *Journal of Molecular Liquids*, *154*(1), 23–25. http://doi.org/10.1016/j.molliq.2010.03.005

Belyaev, V. B., Miller, M. B., Otto, J., & Rakityansky, S. A. (2016). Nuclear fusion induced by x rays in a crystal. *Physical Review C*, *93*(3), 034622. http://doi.org/10.1103/PhysRevC.93.034622

Belyaev, V. B., Motovilov, a K., & Sandhas, W. (1996). Fusion reactions in molecules via nuclear threshold resonances. *Journal of Physics G: Nuclear and Particle Physics*, *22*(7), 1111–1113. http://doi.org/10.1088/0954-3899/22/7/016

Belyaev, V. B., Motovilov, a. K., Miller, M. B., Sermyagin, a. V., Kuznetzov, I. V., Sobolev, Y. G., … Vasiliev, S. I. (2001). Search for Nuclear Reactions in Water Molecules. *Institute for Nuclear Research, RAS, 117312*, 4. Nuclear Experiment. http://doi.org/10.1016/S0370-2693(01)01260-6

Belyaev, V., & Miller, M. (2011). Quantum Amplification on Molecular-Nuclear Transitions. *arXiv Preprint arXiv:1104.2709*. Retrieved from http://inspirehep.net/record/896135/files/arXiv:1104.2709.pdf

Belyaev, V., Miller, M., & Sobolev, Y. (2006). Molecular-Nuclear Transition 6LiD→ 8Be*: Search with a Paired ΔE-E Telescope. *Few-Body Systems*, *38*(2-4), 103–107. http://doi.org/10.1007/s00601-005-0146-7

Belyaev, V., Motovilov, A., & Sandhas, W. (1996a). Can Water“ Burn”? *Physics-Doklady*, (June), 211–215. Retrieved from http://theor.jinr.ru/~motovilv/mypapers/dan96bms.pdf

Belyaev, V., Motovilov, A., & Sandhas, W. (1996b). On the possibility of fusion reactions in water molecules. *arXiv Preprint Nucl-th/9601021*, (6), 5–8. Retrieved from http://arxiv.org/abs/nucl-th/9601021

Bracci, L., & Fiorentini, G. (1982). Mesic molecules and muon catalysed fusion. *Physics Reports*, *86*(4), 169–216. http://doi.org/10.1016/0370-1573(82)90095-3

Cassou, R., & Benton, E. (1978). Properties and applications of CR-39 polymeric nuclear track detector. *Nuclear Track Detection*, *2*, 173–179. Retrieved from http://scholar.google.com/scholar?hl=en&btnG=Search&q=intitle:PROPERTIES+AND+APPLICATIONS+OF+CR-39+POLYMERIC+NUCLEAR+TRACK+DETECTOR#0

CODATA. (2010a). CODATA Value: Boltzmann constant in eV/K. Retrieved August 18, 2014, from http://physics.nist.gov/cgi-bin/cuu/Value?tkev

CODATA. (2010b). CODATA value: Fine-structure constant. Retrieved March 25, 2015, from http://physics.nist.gov/cgi-bin/cuu/Value?alph

D.R. Tilley, C.M. Cheves, J.L. Godwin, G.M. Hale, H.M. Hofmann, J.H. Kelley, G. S. and H. R. W. (2004). TUNL Nuclear Data Evaluation Project, “Energy Level Diagram, 8Be.” Retrieved August 17, 2014, from http://www.tunl.duke.edu/nucldata/index.shtml

Eliezer, S., Tajima, T., & Rosenbluth, M. (1987). Muon catalysed fusion-fission reactor driven by a recirculating beam. *Nuclear Fusion*, *527*, 527–547. Retrieved from http://iopscience.iop.org/0029-5515/27/4/001

Fleischer, R. L., Price, P. B., & Walker, R. M. (1975). *Nuclear Tracks in Solids: Principles and Applications*. University of California Press. Retrieved from http://books.google.com/books?id=yfTBvben3GoC&pgis=1

G.Audi, M.Wang, A.H.Wapstra, F.G.Kondev, M.MacCormick, X. X. (2012). Atomic Mass Adjustments. Retrieved August 18, 2014, from http://amdc.impcas.ac.cn/evaluation/data2012/data/mass.mas12

Grodstein, G. (1957). X-ray attenuation coefficients from 10 keV to 100 MeV. *NBS Circular*, *583*. Retrieved from http://oai.dtic.mil/oai/oai?verb=getRecord&metadataPrefix=html&identifier=ADA278139

Harley, D., Muller, B., & Rafelski, J. (1990). Muon catalysed fusion of nuclei with Z>1. *Journal of Physics G: Nuclear and Particle Physics*, *16*(2), 281–294. http://doi.org/10.1088/0954-3899/16/2/017

HVAC Air Conditioning Designs. (2010). The Nature of Heat. Retrieved March 25, 2015, from http://www.hvacairconditioningdesign.com/the-nature-of-heat/

IAEA. (2012). Livechart - Table of Nuclides - Nuclear structure and decay data. Retrieved from https://www-nds.iaea.org/relnsd/vcharthtml/VChartHTML.html

Jackson, D. F., & Hawkes, D. J. (1981). X-ray Attenuation Coefficients of Elements and Mixtures. *Physics Reports Review Section Of Physics Letters*, *70*(3), 169–233. Retrieved from http://www.sciencedirect.com/science/article/B6TVP-46P3X41-7H/2/af96b42990e48202f7b49e0058e60bcb

Jones, S. E. (1986). Muon-catalysed fusion revisited. *Nature*, *321*(6066), 127–133. http://doi.org/10.1038/321127a0

Kawamura, N., Ishida, K., Matsuzaki, T., Imao, H., & Nagamine, K. (2010). Muonic molecule formation in muon-catalyzed fusion. *Journal of Physics: Conference Series*. http://doi.org/10.1088/1742-6596/225/1/012025

Krestel, E. (1990). Generation of x-ray and gamma radiation. In *Imaging Systems for Medical Diagnostics*.

Lamarsh, J. R., & Baratta, A. J. (2012). *Introduction to Nuclear Engineering* (Third Inte). New Jersey: Pearcon.

Martin, B. (2009). *Nuclear and Particle Physics - An Introduction* (2nd ed.).

Musumarra, A., Pizzone, R., Blagus, S., Bogovac, M., Figuera, P., Lattuada, M., … Zadro, M. (2001). Improved information on the 2H(6Li,α)4He reaction extracted via the “Trojan horse” method. *Physical Review C*, *64*(6), 068801. http://doi.org/10.1103/PhysRevC.64.068801

Nikezic, D. (2005). Track Test. Retrieved from http://www.cityu.edu.hk/ap/nru/test.htm

NIST - Physical Meas. Laboratory. (2014). XCOM - Photon cross section data. Retrieved from http://physics.nist.gov/PhysRefData/Xcom/html/xcom1.html

OpenSTAX. (n.d.). Binding Energy per Nucleon. Retrieved February 23, 2015, from http://cnx.org/resources/c47149992511611c5b7fab39ff7cd6ff/Figure_32_06_03a.jpg

Plechaty, E., Cullen, D., & Howerton, R. (1975). Tables and graphs of photon interaction cross sections from 1.0 keV to 100 MeV derived from the LLL evaluated nuclear data library. *UCRL-50400*, *6*. Retrieved from http://www.osti.gov/energycitations/product.biblio.jsp?osti_id=4033019

Rafelski, H., & Harley, D. (1991). Cold fusion: muon-catalysed fusion. *J. Phys. B: At. Mol. Opt. Phys*, *24*, 1469–1516. Retrieved from http://iopscience.iop.org/0953-4075/24/7/006

Roussetski, A. (2006). CR-39 track detectors in cold fusion experiments: Review and perspectives. *11th International Conference on Cold Fusion*. Retrieved from http://books.google.com/books?hl=en&lr=&id=Fsm5iewynnEC&oi=fnd&pg=PA274&dq=CR-39+TRACK+DETECTORS+IN+COLD+FUSION+EXPERIMENTS:+REVIEWAND+PERSPECTIVES&ots=xapAEtzlpC&sig=_PrxFeRElLouAYd2ywzuwa0JfP0

Sprawls, P. (1995). *The Physical Principles of Medical Imaging. P. Sprawls, The Physical Principles of Medical Imaging, 2nd ed. Madison, Wis: Medical Physics Publishing, 1995.* Retrieved from http://www.sprawls.org/ppmi2/XRAYPRO/

Staritzky, E., & Walker, D. I. (1956). Crystallographic Data. 124. Lithium Hydride, LiH; 125. Lithium Deuteride, LiD. *Analytical Chemistry*, *28*(6), 1055–1055. http://doi.org/10.1021/ac60114a043

Tucker, D., Barnes, G., & Chakraborty, D. (1991). Semiempirical model for generating tungsten target x-ray spectra. *Medical Physics*, *18*(2), 211–218. Retrieved from http://link.aip.org/link/?MPHYA6/18/211/1

Unsworth, M., & Greening, J. (1970). Theoretical continuous and L-characteristic X-ray spectra for tungsten target tubes operated at 10 to 50kV. *Physics in Medicine and Biology*, *621*, 621–630. Retrieved from http://iopscience.iop.org/0031-9155/15/4/001

Wallace, O. J. (1974). *Gamma-ray dose and energy absorption build-up factor data for use in reactor shield calculations*. Springfield. Retrieved from http://www.iaea.org/inis/collection/NCLCollectionStore/_Public/06/167/6167564.pdf

Williams, B. (1977). *Compton scattering: the investigation of electron momentum distributions*. New York: McGraw-Hill International. Retrieved from https://0-inis.iaea.org.innopac.up.ac.za/search/searchsinglerecord.aspx?recordsFor=SingleRecord&RN=10486110

Zettili, N. (2009). Quantum Mechanics: Concepts and Applications. Jacksonville: Wiley. Retrieved from http://eu.wiley.com/WileyCDA/WileyTitle/productCd-EHEP002383.html

12. Appendices

12.1. Appendix A – Track detectors

12.1.1. Experimental procedure (example)

12.1.1.1. Etching

12.1.1.1.1. Etchant preparation

12.1.1.1.1.1. Equipment

- Thick-walled measuring cylinder
- Measuring flask
- Scale - beurer S-36
- Pipette
- Funnel
- Polypropylene container
- Mixing rod
- NaOH
- Distilled water

12.1.1.1.1.2. Steps

1. Measuring cylinder is placed on scale and scale is zeroed
2. 125g of NaOH is deposited into the measuring cylinder
3. Measuring cylinder is taken to ventilated area and distilled water is added
    a. Stirring improves reaction rate
    b. Reaction is exothermic
    c. Solution should be left to cool to room temperature
4. Mixture is decanted into a measuring flask with the aid of a funnel
    a. Distilled water should be added to the original container to dissolve remaining precipitates and added to the flask
5. Correct water-level should be obtained in the flask (500ml)
    a. Mixture should be mixed after each addition of distilled water since the level will drop due to the temperature difference (warm water being cooled)
    b. Distilled water should be slowly added using a pipette
6. Mixture should be decanted into Polypropylene container for long-term storage
    a. Mixture cannot be stored in glass containers for prolonged periods

12.1.1.1.2. Etching (Old samples)

12.1.1.1.2.1. Equipment

- Magnetic agitator - MLW RH-3
- Circulation thermostat - MLW U-8
- Heating container
- Clamp stand
- Thermometer
- Tweezers
- Optic microscope

- Cotton pads
- Copper wire
- Timer - Cassio SPF-60D
- NaOH solution - 6.25Mol/l
- CH_3COOH - 98%
- CR-39 sample
- Distilled water
- Filter paper

12.1.1.1.2.2. Steps

1. Heating container clamped into position over magnetic agitator
2. NaOH solution decanted into heating container
3. Magnetic agitator mixing magnet placed into solution, and magnetic agitator is activated
4. Heating container is connected to Circulating thermostat
5. Circulating thermostat is set to 75°C and activated
    a. Set-up is left for a while so that the solution can reach the correct temperature
    b. Thermometer is used to check current temperature of circulating water
6. A thermostat is used to check the temperature of the NaOH solution - 74°C
7. CR-39 sample is cleaned using cotton pad and distilled water
    a. Tweezers should be used to hold the sample in position
    b. Care should be taken not to touch the operating surface of the sample
8. Copper wire is tied around the sample so that it may be vertically suspended (Copper does not react with NaOH)
9. The sample is suspended in the solution
    a. Magnetic agitator speed is decreased
    b. Timer is started
    c. Sample is left for 4 hours
10. Sample is removed and washed
    a. Sample is rinsed in distilled water
    b. Sample is rinsed in 250 ml distilled water with 3 ml of acid
    c. Sample is rinsed in distilled water
11. Sample is dried
    a. Using the folds of filter paper
12. Sample is inspected
    a. Sample is viewed under microscope to detect tracks and determine if the sample should be etched again
        i. Tracks were very few, and hardly detectable
        ii. Decision was made to re-etch
13. Steps 9 to 11 repeated so that total etching time is 8 hours
14. Sample is inspected using optical microscope

12.1.1.1.3. Observations

12.1.1.1.3.1. Track density

1. The entire surface is studied and tracks are counted
    a. This method is painstaking and tedious
2. Sample views at various magnifications are taken and tracks are counted
    a. The fov is used as a reference area in determining track density

12.1.1.1.3.2. Track diameter

1. Magnification is calibrated
    a. Calibration slide used to determine size of reference blocks as well as fov
2. Tracks are located and images are taken
3. Image editing software is calibrated and used in order to measure track diameters

12.1.1.2. Alpha Irradiation

12.1.1.2.1. Experimental setup

- An aluminium sheet with a thin layer of ^{212}Pb is used as the alpha source
- A layer of steel is used to shield the detector
- In the steel shield there is a 5mm diameter hole
- On the opposite side of the shield the detector is placed
- Air is allowed to be present in the hole
- Samples were irradiated for various time intervals

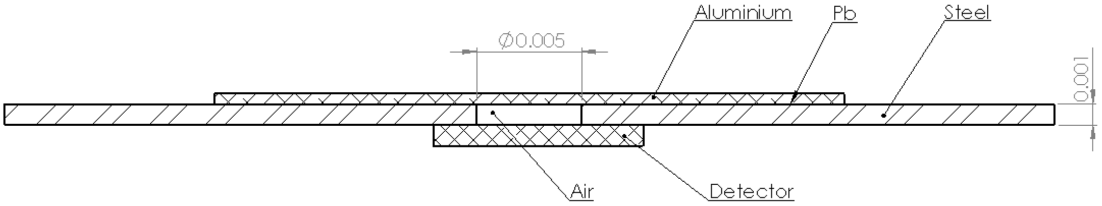

Figure 91 - Thin alpha irradiation setup (setup 1)

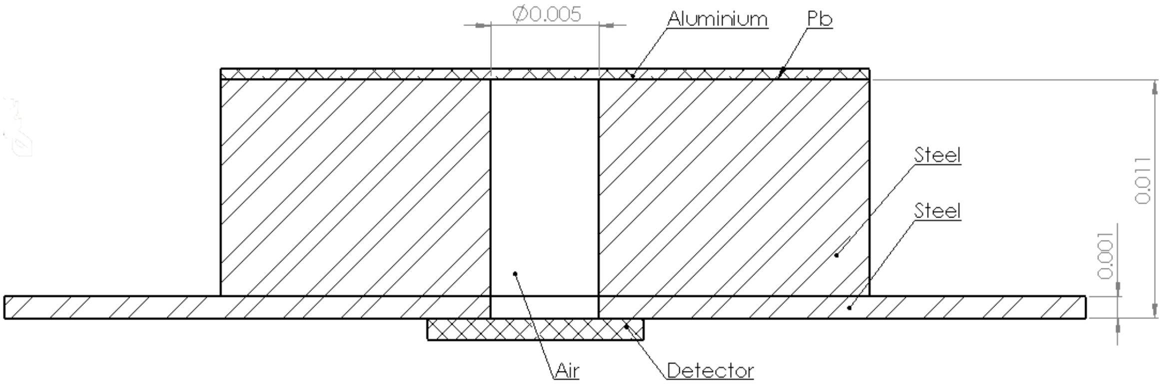

Figure 92 - Thick alpha irradiation setup (setup 2)

12.1.1.2.2. Explanation

Lead decays according to the scheme indicated according to Figure 93.

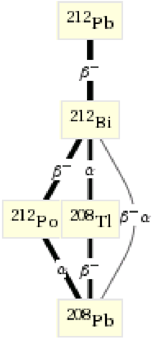

Figure 93 - 212Pb decay chain[23]

The decay of ^{212}Po to ^{208}Pb produces 8.95412 [MeV], and that of ^{212}Bi to ^{208}Tl produces 6.20726 [MeV]. By applying $Q_c = \frac{Q}{1+\frac{m_c}{m_d}}$ the ^{212}Po α-particle has an energy of 8.785047844 [MeV], and the ^{212}Bi α-particle has an energy of 6.090057163 [MeV].

Since the experiment does not take place in a vacuum corrections for energy loss in air must also be made:

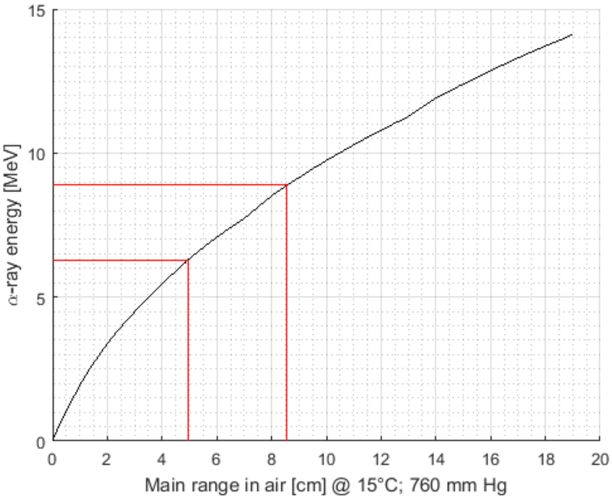

Figure 94 - Distance travelled by α -particles in air

From Figure 94 it can be seen that an 8.78 [MeV] α-particle can travel 8.42 [cm] in air, and a 6.09 [MeV] α-particle can travel 4.7 [cm] in air. Assuming the relationship between energy lost and distance travelled is linear the new energies for the α-particles can be calculated as such that $E_{new} = \left(1 - \frac{d_{travelled}}{d_{max}}\right) \cdot E_{original}$. This leads to:

- For setup 1
    - 5.960481479 [MeV]
    - 8.680712359 [MeV]
- For setup 2

---

[23] http://www4b.wolframalpha.com/Calculate/MSP/MSP74981h4ife92497i752100000h1cf7cdee16a95d?MSPStoreType=image/gif&s=44&w=91.&h=210

- 4.664724635 [MeV]
- 7.637357508 [MeV]

Using $\frac{R_a}{R} = 3100\frac{\rho}{\sqrt{M}}$ we can estimate what shielding would be sufficient to prevent α-particles from entering the environment, or reaching the parts of the detector that is not exposed to air. The thickness of the aluminium would need to be 0.0196317288 [cm], and 0.01388713965 [cm] for the steel. This means that no α-particles are released to the environment, or reach the detector through the steel.

12.1.2. Environmental exposure

12.1.2.1. Experiment

The purpose of the experiment was to determine the background of α-particles present at the JINR. Samples were exposed to the environment for 5 years and experienced α-irradiation mostly from Radon decay. It should be noted that the Radon concentration at the JINR is 3 times higher than in general.

12.1.2.1.1. Expectations

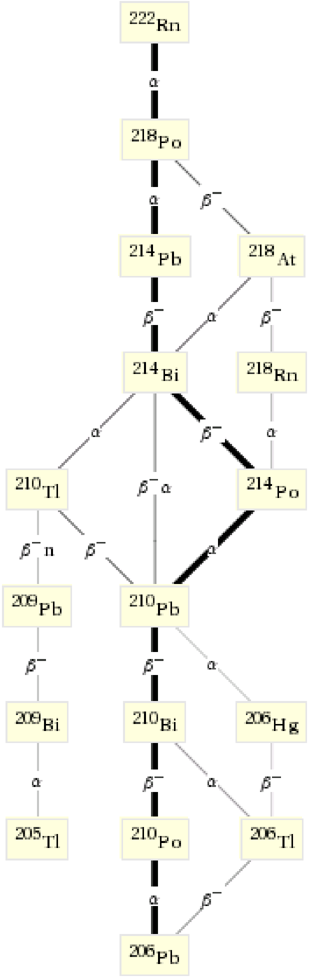

Figure 95 - ^{222}Rn decay chain

The decay chain for ^{222}Rn is shown in Figure 95. Using this we can isolate the energies we could expect to observe.

Table 18 – ^{222}Rn decay

Isotope	Rn222	Po218	At218	Rn218	Bi214		Po214	Bi209	Po210
Energy [MeV]	5.59031	6.11468	6.874	7.26253	11.1023	5.62119	7.83347	3.13721	5.40745
Half-life	91.7639 [hrs]	185.9[s]	1.5[s]	35[ms]	19.9[min]		164.3[us]	1.9E19[yrs]	138.376[d]
Probility	1	0.9998	0.0001998	2E-07	3E-05	0.00021	0.99976	1.89E-08	0.99999998

Table 1 shows that some alpha decays are very unlikely to occur, whereas others have very long half-lives and may also not be observable. The results indicate that the most expected energies are those from ^{222}Rn (5.59031[MeV]), ^{218}Po (6.11468[MeV]), and ^{214}Po (7.83347[MeV]).

These decays however exist in the environment around the track detectors at varying distances. It would thus be foolish to expect to isolate tracks of varying energies, since α-particle energies will be lost in collisions on the way to the track detector. The only conclusion we can draw with confidence is that no α-particles with energies over 11.1023[MeV] should be encountered (as a result of Radon), and that it's unlikely to encounter α-particles with energies greater than 7.83347[MeV] (as a result of Radon).

Calculations indicate an expected value of 2500[α/cm^2].

12.1.2.2. Measurements

There were 3 measurement techniques that were employed, and 2 purposes. One purpose was to investigate the track density, whereas the second was to investigate the track development as etching time was changed. The measurements were conducted with an optic microscope, as well as a SEM.

12.1.2.3. Results

12.1.2.3.1. Density Measurements

12.1.2.3.1.1. Set I

The first experiment was conducted after etching the track-detector for 8 hours at 70°C. Tracks were counted on both sides, however only 75% of tracks on side B were counted before the end of the day. With no markers available it was assumed that the tracks should be dispersed homogenously on the detector and that the values could be considered representative.

The readings resulted in a density of 916[tracks/cm^2] on side A, and 1207.4667[tracks/cm^2] on side B.

12.1.2.3.1.2. Set II

The next experiment comprised of 14 measurements per magnification at arbitrary locations on each side of the detector respectively. An average was taken between these measurements for each magnification, and finally these values were averaged.

The readings suggested a density of 2588.49[tracks/cm^2] on side A, and 2896.54[tracks/cm^2] on side B.

12.1.2.3.1.3. Set III

Finally 11 readings were made for each of the magnifications, this time differentiating to a certain extent between sizes and shapes of the tracks. By this time it had been noticed that some tracks were very vague and probably represented proton tracks instead of α-particle tracks.

The total averaged track density for side A was 5466.079[tracks/cm^2] and for side B was 4789.766[tracks/cm^2]. However when disregarding suspected neutron tracks the averaged densities were 1333.17[tracks/cm^2] for side A and 1377.559[tracks/cm^2] for side B.

12.1.2.3.1.4. Conclusions

Averaging the relevant densities yields a track density of 1612.33[tracks/cm^2] fro side A, and 1826.6[tracks/cm^2] for side B. This is only about 70% of the expected results. However it should be considered that the expected results includes α-particles with incident angles ranging over 180°. However etching efficiency does not allow for all these particles to be registered. Furthermore statistical variances may occur, thus the results seem representative of what was expected.

12.1.2.3.2. Size measurements

For this experiment the major and minor diameters of tracks on one side of a detector were measured. All tracks were measured numbering well over 3000.

The distributions of the means is displayed in figure 2.

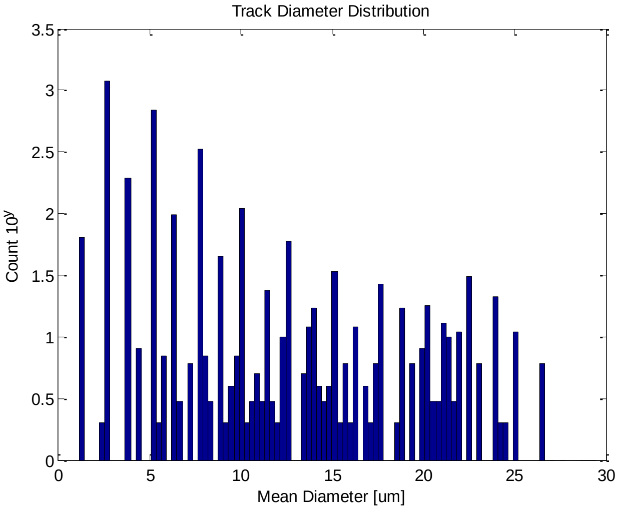

Figure 96 - Diameter distribution for environmental exposure

A logarithmic scale was chosen for this figure due to the overwhelming number of tracks with a small mean diameter. These are assumed to be neutron tracks.

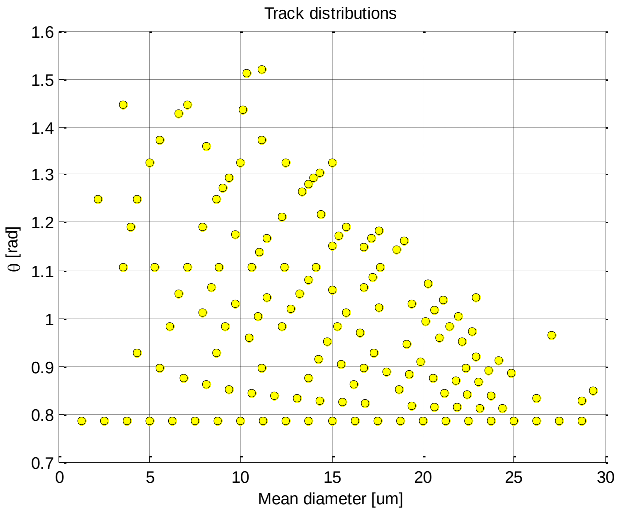

Figure 97 - Environmental tracks

Figure 97 indicates a different way at looking at the distribution where $\theta = \tan^{-1}\left(\frac{d_{maj}}{d_{min}}\right)$. The reason for this distribution will be indicated in a different section.

12.1.2.3.3. Etching development

The purpose of this experiment was to determine track development as etching time is increased. The original etching time was 2 hours, and the etching time was increased by 2 hour steps up to 16 hours. Various samples were used for each time-interval since the processing of the detector in order to view the tracks using the SEM would complicate continued etching.

12.1.2.3.3.1. Simulation

Track_test was used to simulate the development in order to determine if the yielded results made sense.

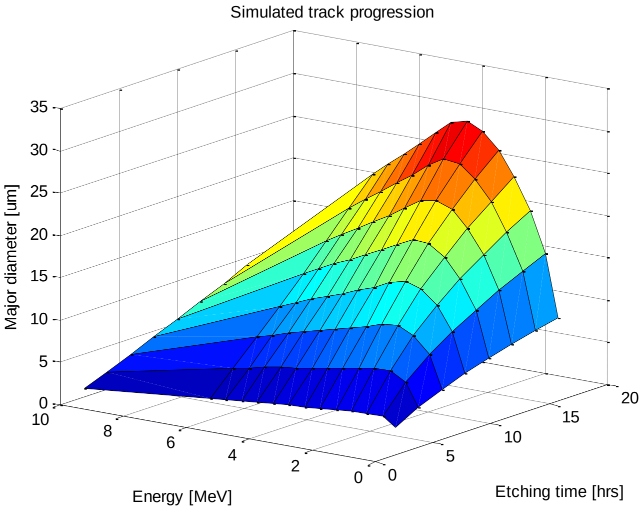

Figure 98 - Simulated track progression

Figure 98 indicated the expected major diameter for particles incident at 90° to the detector surface at varying energies as etching time is varied. It is interesting to note that the maximum diameter for a given etching time is not always at the lowest energy, but instead is moved to increasing energies as etching time is increased.

12.1.2.3.3.2. Results

Measurements were made using a SEM. The expected results were for the average diameter to increase as etching time is increased.

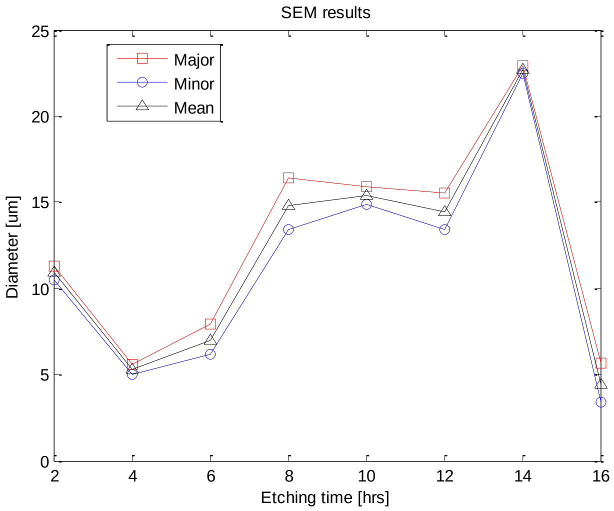

Figure 99 - SEM results

The results as shown in Figure 99 do not agree at all with the expected results. The reason for this is simple – with no reference energy the number of tracks considered were not statistically representative. To gain meaning from this type of experiment tracks of a known energy should be analysed, or alternatively enough tracks should be measured to gain accuracy.

12.1.3. α-particles

12.1.3.1. Experiment

The purpose of this experiment was to determine if a distinction could be made between tracks of varying energies.

12.1.3.1.1. Experimental setup

There were 2 experimental setups. The first was a thin setup where an α-source was close to the detector. The detector was exposed for 1, 10, and 30[s] respectively.

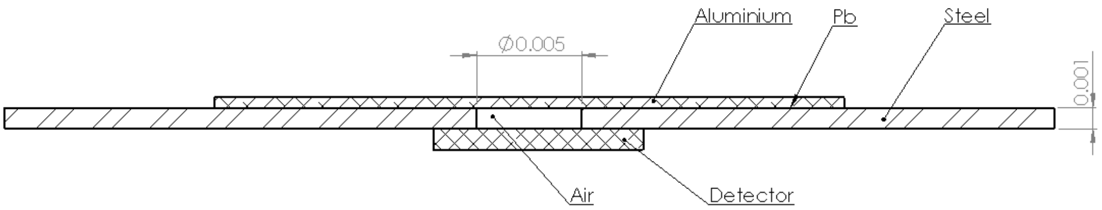

Figure 100 - Thin experimental setup

The secondary setup increased the distance between the α-source and the detector, the exposure time was 60[s].

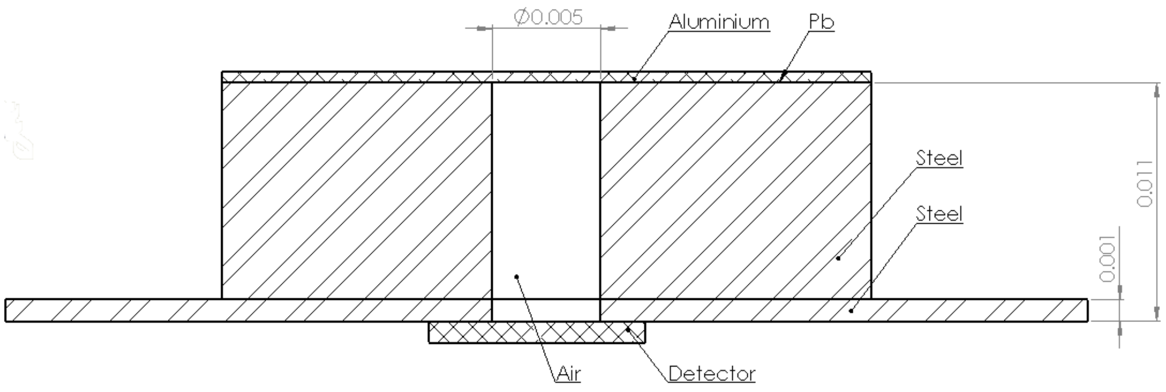

Figure 101 - Thick setup

12.1.3.1.2. Preparation

The ^{222}Pb is prepared in the following fashion:

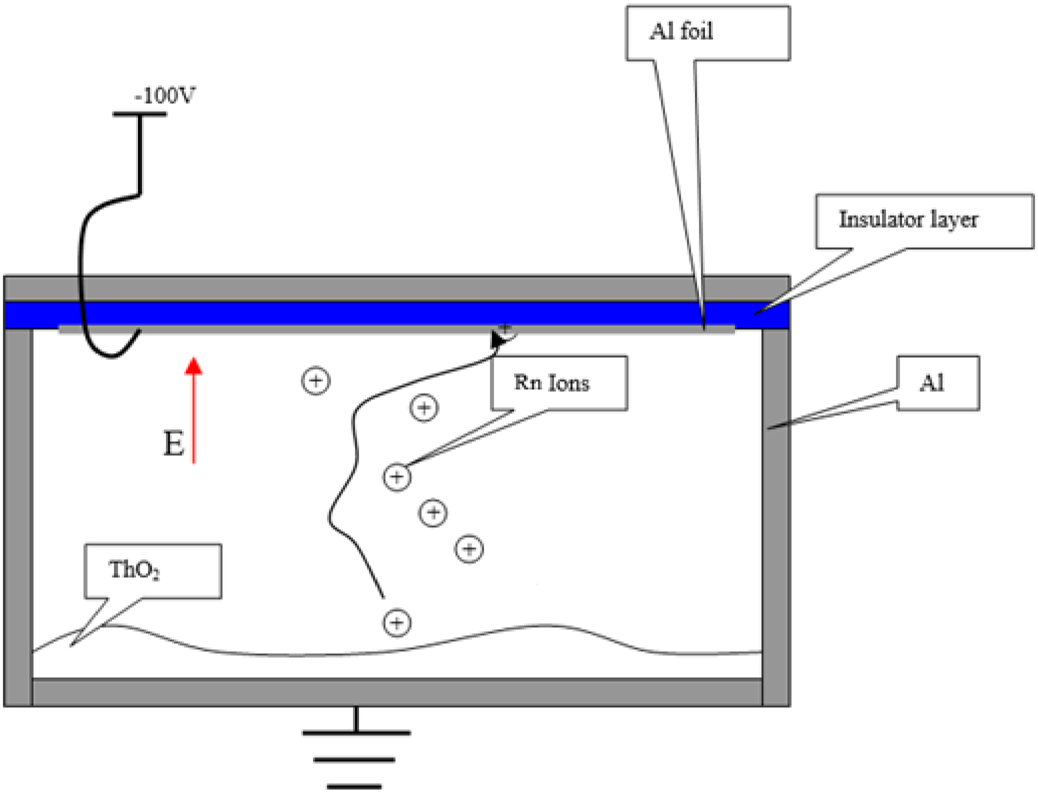

Figure 102 - Schematic representation of preparation of ^{222}Pb layer

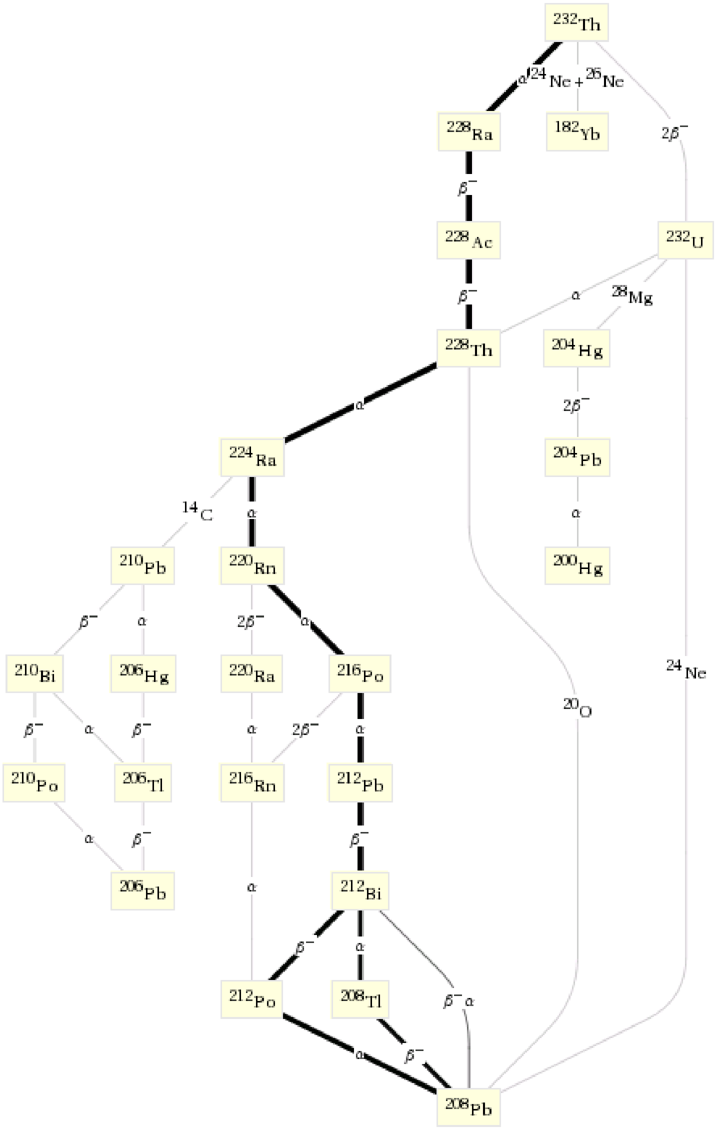

Figure 103 - ^{232}Th decay chain

^{220}Rn is produced through the decay chain of ^{232}Th. These are in the form of positive ions due to the fact that electrons were lost when recoiling as a result of the emission of an α-particle in the decay ^{224}Ra → ^{220}Rn. The positive ions then drift to the cathode and continue to decay to ^{212}Pb.

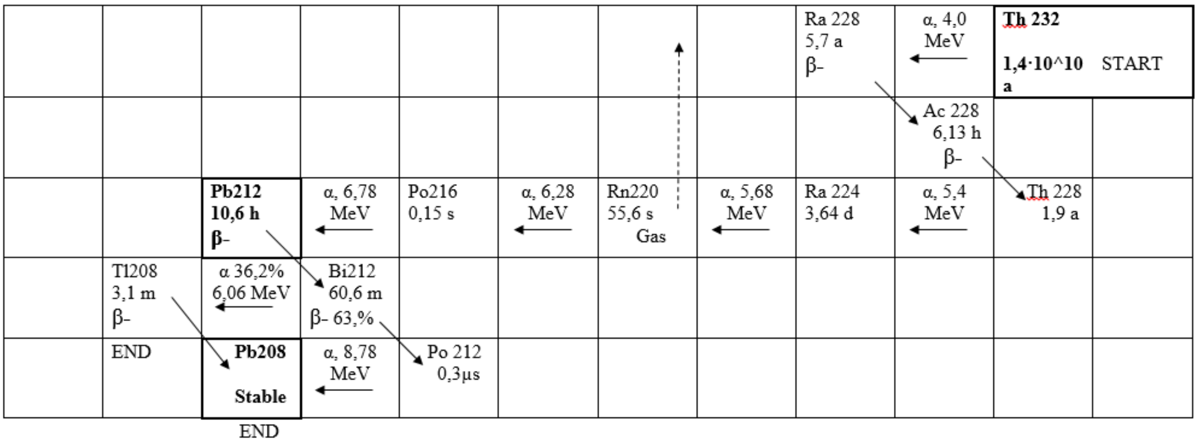

Figure 104 - Schematic representation of decay chain

12.1.3.1.3. Expectations

The decay chain of the resulting ^{212}Pb (as indicated in both Figure 103 and Figure 104) is:

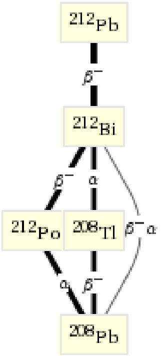

Figure 105 - Decay chain of ^{212}Pb

From this it can be seen that α-particles will be emitted at 2 energies, namely 8.78 and 6.06[MeV] respectively (the likelihood of the $\beta^-\alpha$ decay mode is negligible, however it produces a 11.2[MeV] α-particle)

Due to energy loss in air the expectation is to encounter tracks deposited by α-particles wit energies of 5.96 and 8.68[MeV] respectively. For the same reason the particles in the second setup should have lower energies, and 4.66 and 7.64[MeV] α-particle tracks are expected in this configuration.

12.1.3.1.3.1. Simulation

Track_test was once again used to simulate the experiment in order to provide more accurate expectations. It should be noted that since the bulk and preferential etch rates were not determined the software can only be used to estimate shapes, and should not be expected to provide accurate analysis with reference to diameters.

Secondly $\theta \neq \sin^{-1}\left(\frac{d_{min}}{d_{maj}}\right)$ since this does not truly represent the incident angle. This is shown in figure 12, where very large errors are often encountered using this method. The reason for this deviation is that the simple trigonometric ratio does not take the etching dynamics into account.

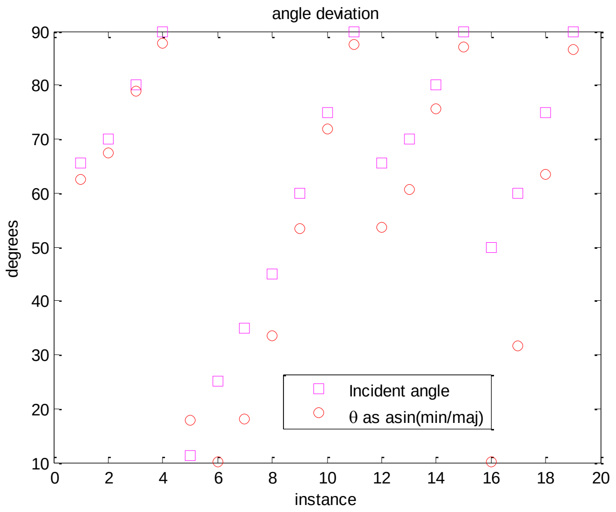

Figure 106 - Angle deviation

It was also noted that since the second setup has α-particles coming in from further away, the allowable range of angles is diminished. This was taken into account and the expected distributions are as follows (for 8 hours etching at 70°C):

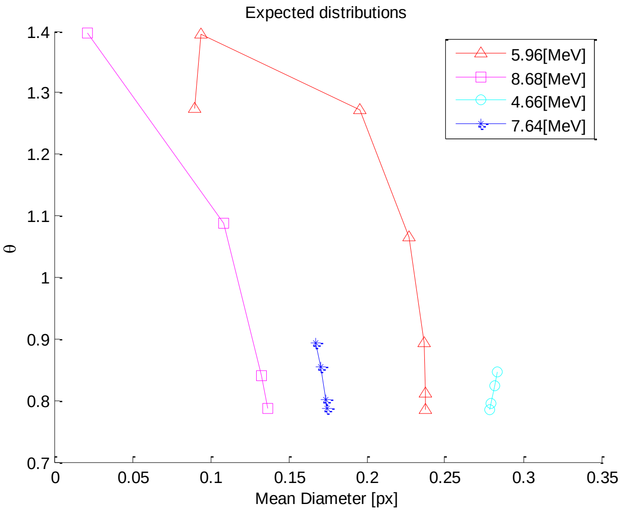

Figure 107 - Simulated track distributions

It must be noted that the larger the mean diameter (in general) the lower the energy of the α-particle that left the track under these conditions.

12.1.3.1.4. Problems

The etching involved 3 samples being etched at once at first, followed by a batch of 2. However due to an equipment malfunction the first 3 samples were etched at about 64°C for between 1 and 2.5 hours. This means that all the samples cannot be directly compared to one-another since these track diameters will have been etched significantly less.

12.1.3.2. Measurements

Considering the energies imparted by the α-particles, as well as the difficulties introduced by the proton tracks a decision was made to only consider certain tracks that seemed dark enough. This can be considered a problem since some lower-energy tracks may have been neglected. However all the high-energy tracks will be noted. This decision allowed the detectors to be processed at a significantly greater rate, and it will be seen that adequate results were obtained. To improve accuracy photographs were taken of all the relevant tracks, and image-editing software was used to for measurements.

12.1.3.3. Results

The mean diameters of the tracks were tabulated, plotted and compared.

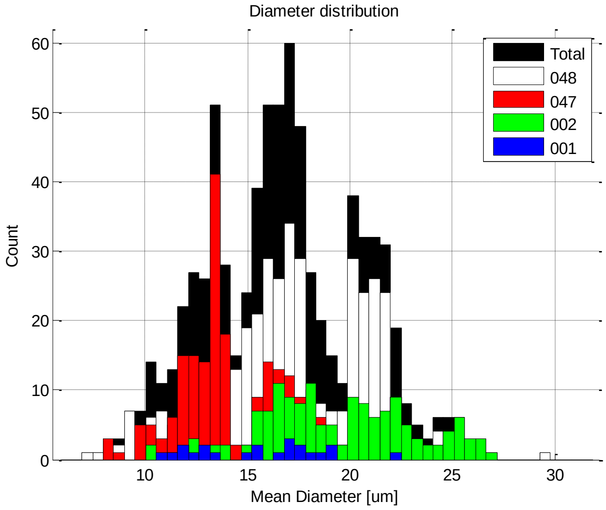

Figure 108 - Diameter distribution

The black bars indicate 3 peaks. It is roughly assumes that each peak represents a different energy. Our expectation would have been 2 peaks, however the under-etched results are also included here, and for that reason a third peak emerges. The peaks of the cyan and blue bars line up. This is in agreement with reality since they were etched together. The purple, green, and yellow bars represent the other 3 detectors that were processed together. The counts also make sense. Detector 145 was only exposed to background radiation. 001 Was exposed for 1[s], 002 for 10[s], 048 for 30[s] and 047 for 60[s] at a greater distance to the source.

The distributions as before were also plotted

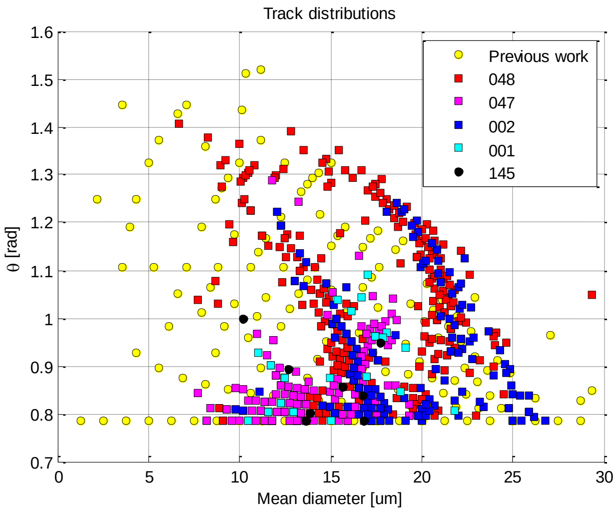

Figure 109 - All track distributions

For this case it would make sense to isolate the samples and compare only those that are of relevance.

The first investigation is made into detectors 002 and 048.

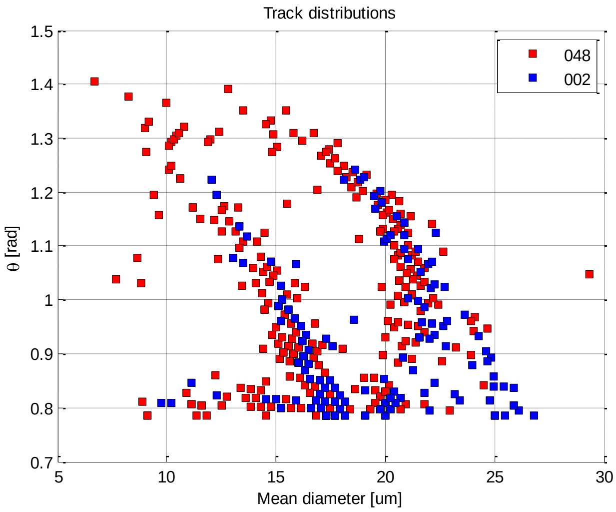

Figure 110 - Track distributions for 002, 048

The distribution of these combined tracks is thus:

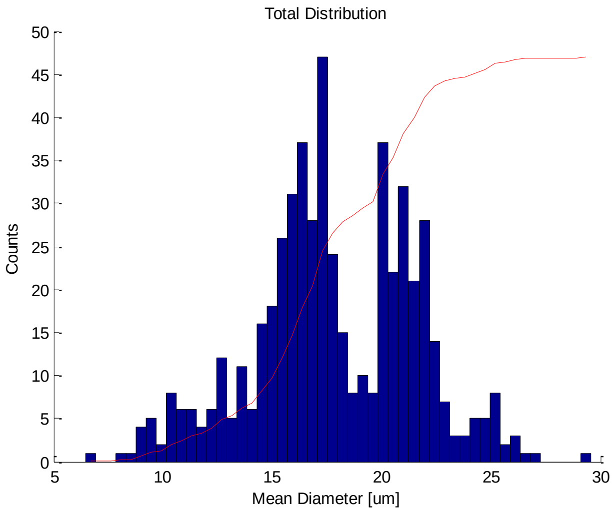

Figure 111 – Diameter Distribution for 002, 048

Figure 111 clearly shows 2 peaks, however in order to obtain more accurate results these peaks should be separated.

From figure 16 it is clear that there are 2 distinct track groups. The bend predicted in figure 13 is also present, and using this as a guide the tracks can be isolated into their respective energy groups.

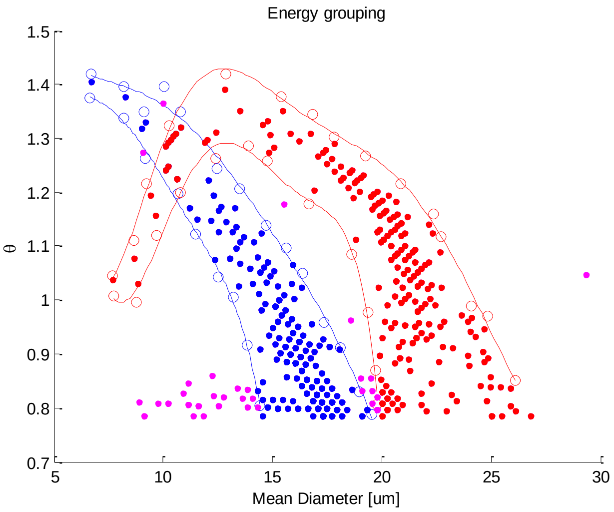

Figure 112 - Energy grouping for 002 and 048

Diameter distributions can then be considered.

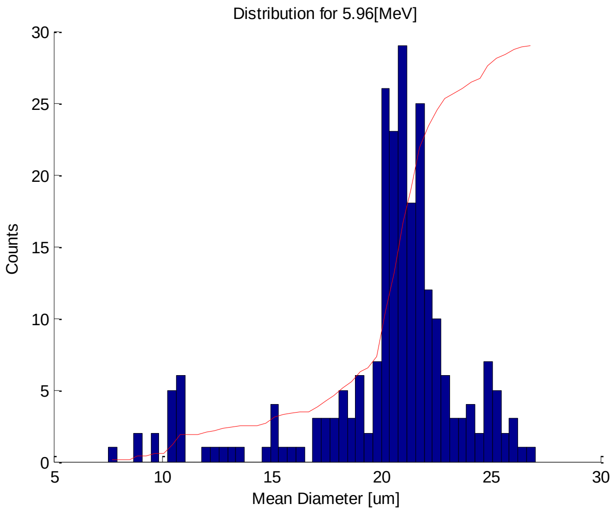

Figure 113 - 5.96[MeV] diameter distribution

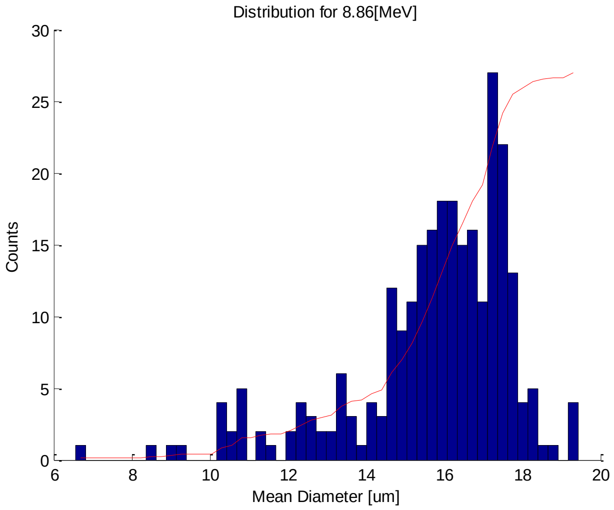

Figure 114 - 8.86[MeV] diameter distribution

Figure 113 and Figure 114 show that there is a clear peak for each energy. Furthermore the long leading tail rather indicates values that do not need to be included when considering the diameter distributions for each of these energies (Especially since they both share a common peak).

The total number of tracks in each instance is also similar with 5.96[MeV] having 241 tracks, and 8.86[MeV] having 266 tracks. The expectation is however for the 8.86[MeV] group to have significantly more tracks, however at small incident angles these high energy particles fail to etch, and this would explain the discrepancy.

Considering 047 and 001 a similar process may be followed.

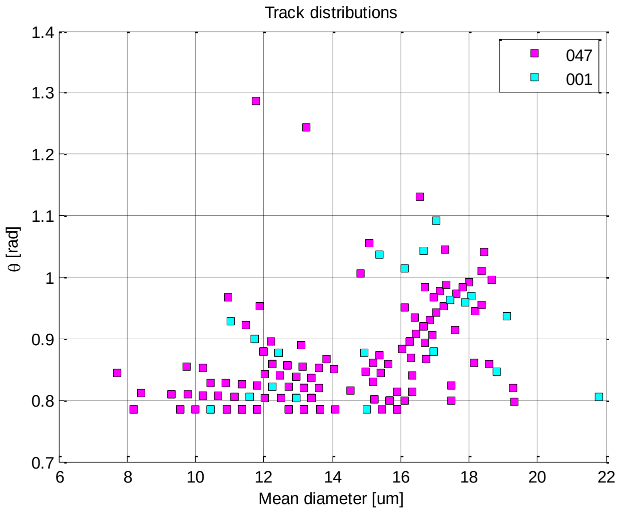

Figure 115 - Track distributions for 001 and 047

Figure 115 also shows 2 groups, however the tendrils are not as long as expressed in figures 16 and 18. This is however in agreement with the predictions made represented in figure 13. The number of tracks in 001 is very small and for that reason it is not reasonable to expect to be able to compare the distribution peaks of 001 and 047 in order to display the energy shift thanks to the increased distance. The shortness of the tendrils also means that it is not necessary to differentiate between the patterns in order to identify which tracks belong to which energy group.

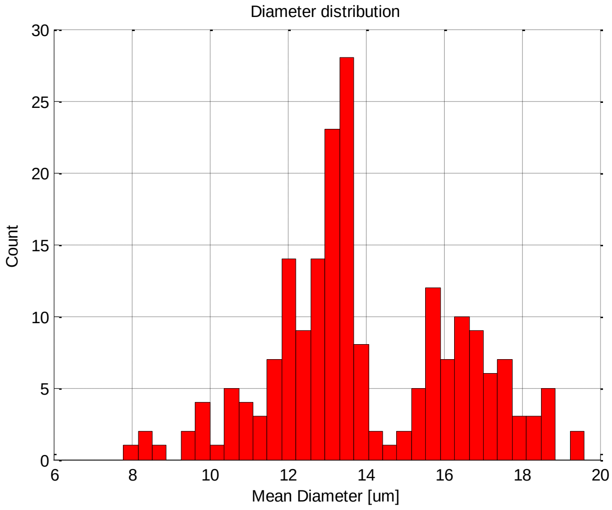

Figure 116 - Diameter distribution for 047

The 2 peaks are well separated. The total number of counts in the 7.64[MeV] group is 110, and there are 65 counts in the 4.66[MeV] group. This is a 63%-37% split, and thus in agreement with the theoretical data.

12.1.3.4. Second attempt

In order to gain an understanding of the preparation of the initial alpha irradiation experiment, a second wave of experimentation was conducted. This experiment would serve as an attempt to correct some of the mistakes that were made in the initial experiment.

12.1.3.4.1. *Experimental setup and expectations*

The setup was similar to that of the initial experiment, however distances were varied once more. Table 19 indicates the setup as well as the expected energies.

Table 19 - Second configuration

Detector no.	Distance from Source	Irradiation time	^{212}Po α-energy	^{212}Bi α-energy
050	11 [mm]	30 [s]	4.66 [MeV]	7.64 [MeV]
095	3 [mm]	10 [s]	5.70 [MeV]	8.47 [MeV]
098	3 [mm]	3 [s]	5.70 [MeV]	8.47 [MeV]
143	16 [mm]	60 [s]	4.02 [MeV]	7.12 [MeV]

12.1.3.4.2. *Uncertainty*

In this instance the irradiation was conducted very soon after the radiation source had been prepared. This means that α-particles from isotopes higher up in the decay chain may also have been present. This results in it being impractical to compare the sizes of the peaks, since the branching ratio would not be the only factor involved when considering the energy of incident particles. Finally the etching started at 74°C but dropped to 72°C at some point in time. All samples for experiment 2 were thus etched the same, however comparison with experiment 1 should take into account that experiment 2 had a slightly lower etching rate.

12.1.3.4.3. *Results*

The mean diameters were once more calculated and compared.

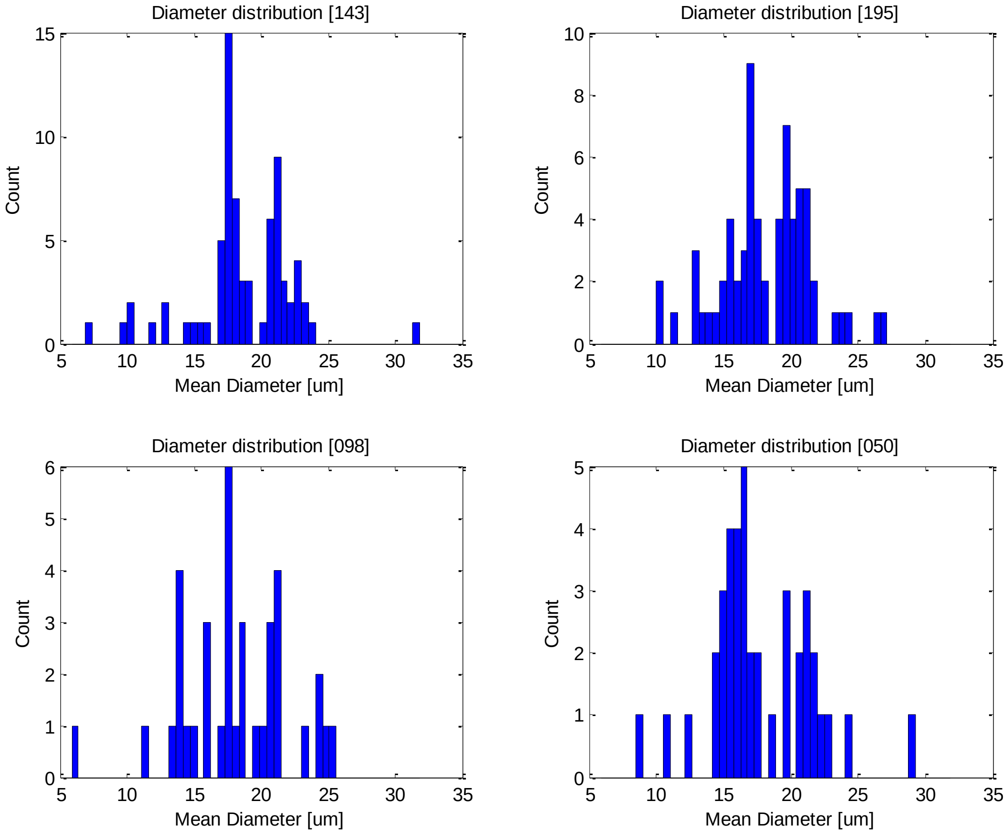

Figure 117 - Diameter distributions for second set of experiments

Figure 117 once again displays the duel peak traits we have come to expect. The peaks for 050 are however not very discernible. Unlike the previous experiment there are far fewer particles with higher mean diameters present. The reason for this was that stricter requirements were set for the measurement of tracks. One of the results of this however is that some tracks that contribute to a certain energy group have been missed.

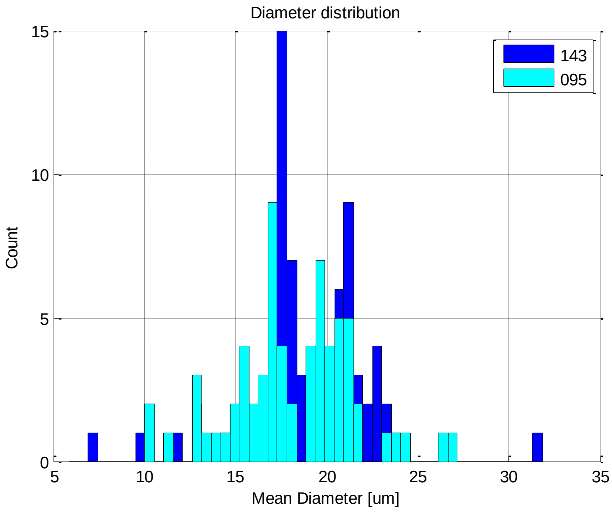

Figure 118 - Distribution comparison

Figure 118 shows that the peaks for the mean diameter shift to the right when comparing 095 with 143. This is what we have expected all along, since the energy of the α-particles that made the tracks in 143 is lower than that of the α-particles that made the tracks in 095.

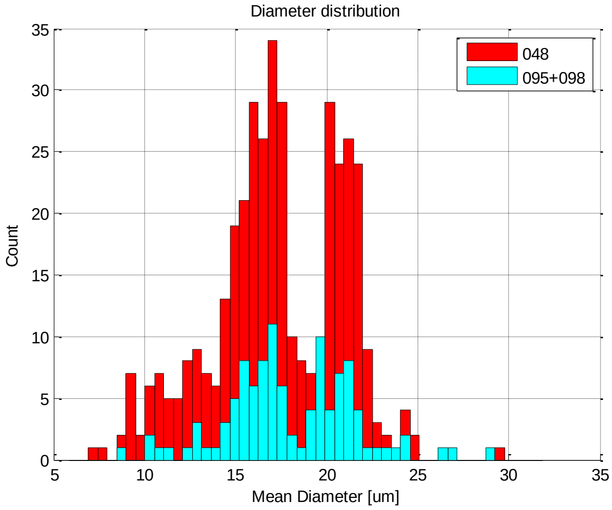

Figure 119 - Comparison between experiments

By considering Figure 119 it can be seen that the peaks do not line up exactly between the experiments, even though they are very close. This means that the etching rates for the 2 experiments were not exactly the same. This is just another indication for the clear need to etch all the detectors together in order to ensure that they all are etched under the same conditions – or to ensure the precision of the etching equipment.

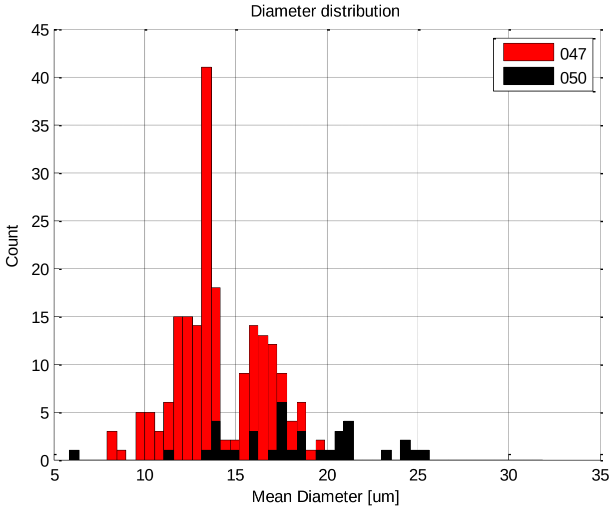

Figure 120 - Etching time shift

The assumed etching time shift can be seen in Figure 120. It was mentioned before that there was a deviation in the etching conditions. Figure 120 compares results from similar radiative circumstances. Although the peaks for 050 are not clear their position does not coincide with the peaks for 047 confirming that the assumption.

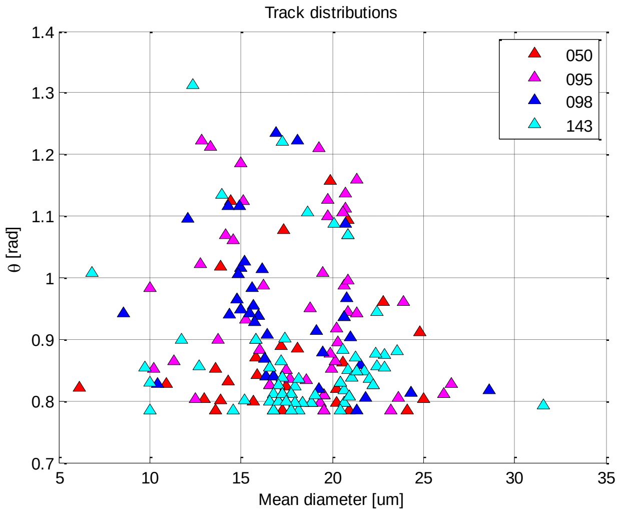

Figure 121 - Angle-based distribution for second experiment

The Results of the second experiments are not as clear as those of the first experiment. There are two possible reasons for this. The first is that the stricter requirements for track measurement may have missed several relevant tracks. The second is that no long-term exposure at close range took place. Part of this is also that only 1 distance of measurement agrees, but the etching rates were not equivalent. The best comparison between the first and second experiment is between 002 and 095.

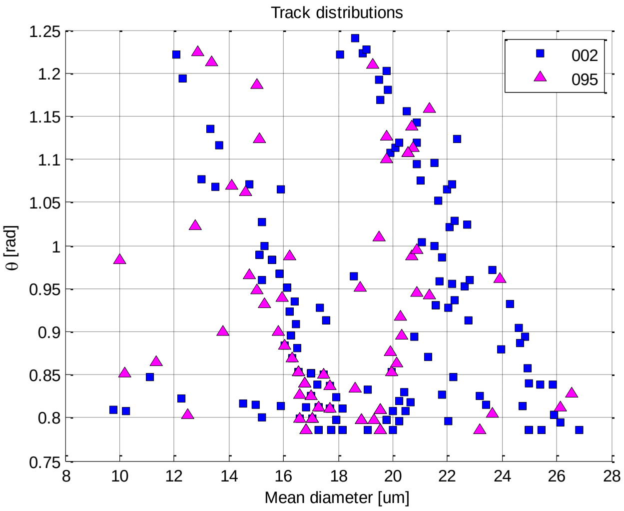

Figure 122 - 002 vs 095

Both these samples were exposed for a similar period however the activity of the α-source may not be equivalent. The distance between the source and the detector is also 2mm for 095. This should mean that the points for 095 should lie to the right of 002. The fact that this does not happen indicates that the etching conditions were not identical.

12.1.4. Protons

12.1.4.1. Experiment

The purpose of this experiment was to identify tracks made by protons with known energies. The protons were provided by a van der Graaf accelerator, and deposited to the detector as a result of Rutherford back scattering off a material.

The proton spectrum was measured using electronic detectors and is shown in Figure 123.

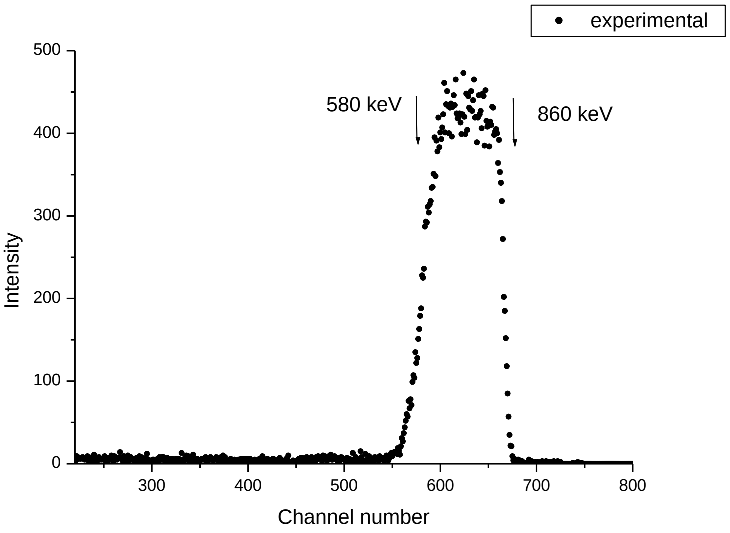

Figure 123 - Proton spectrum

12.1.4.2. Measurements

Two different samples were investigated, exposed to different fluxes. An original analysis was made of the track density for each of the detectors by arbitrary selection of slides, and counting the number of tracks in the slide. The values determined throughout the slides were averaged in order to determine the track density.

A second investigation was made into the development of the tracks with varying etching time. Sample 144 was investigated after 4 and 8 hours. Sample 096 was investigated every 2 hours for a total of 10 hours. In each instance measurements were made at both a medium and large magnification. The purpose of this was to indicate the measurement error.

12.1.4.3. Results

12.1.4.3.1. Distributions

To determine the distribution of energy of the particles the number of particles that fall within each energy group was determined and represented.

12.1.4.3.1.1. Sample 144

At t = 4 [hrs] for sample 144 only one set of measurements are available. These are shown in Figure 124

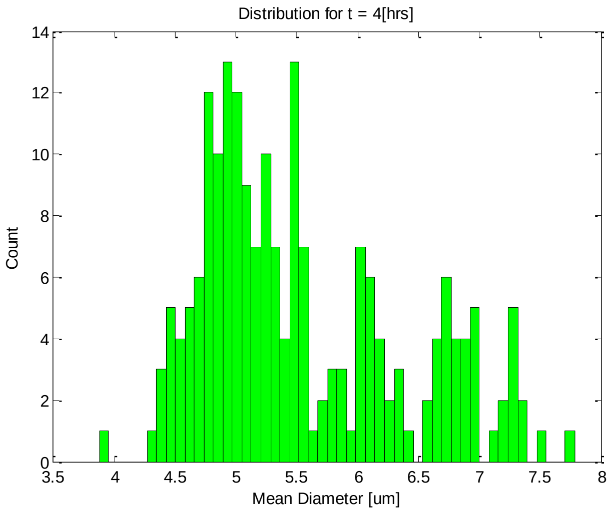

Figure 124 - Detector 144, t = 4[hrs]

Figure 124 shows that the distribution is quite wide. This is entirely to be expected since Figure 123 indicates that the tracks represent a range of energies. The peak is simply a statistical anomaly since not all tracks on the detector surface were measured.

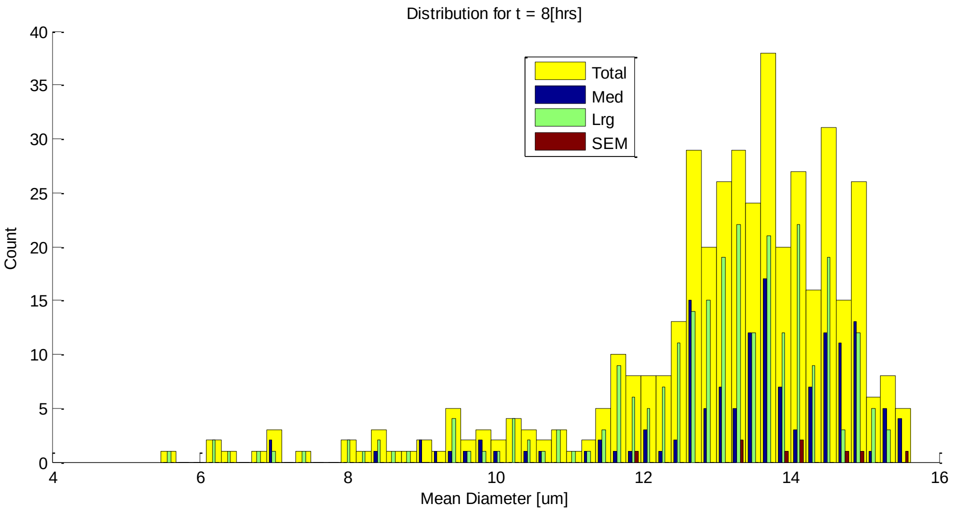

Figure 125 - Detector 144, t = 8[hrs]

The distribution for the same detector after being etched for 8 hours is shown in Figure 125. The distribution is once again wide as expected.

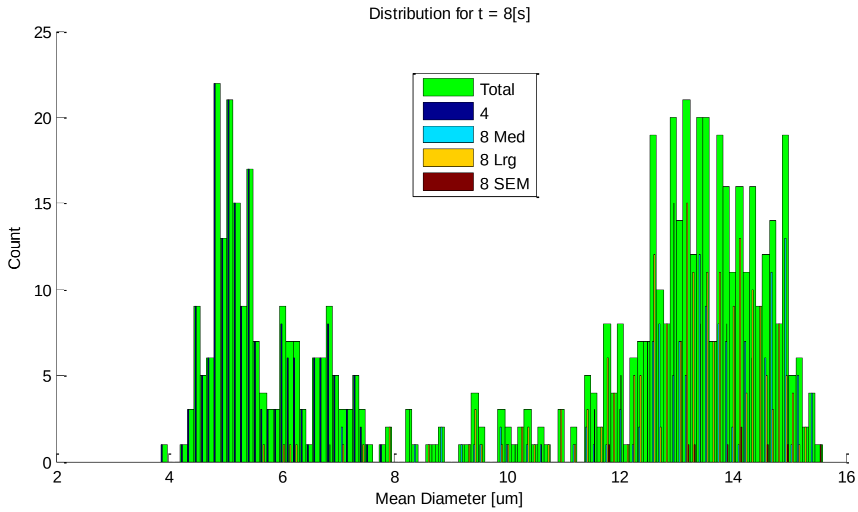

Figure 126 - Detector 144

Figure 126 is generated by combining Figure 124 and Figure 125. There are 2 peaks that are generated, and it can thus be concluded that the track diameter has increased with increasing etching time.

12.1.4.3.1.2. Sample 096

The distributions for detector 096 follow:

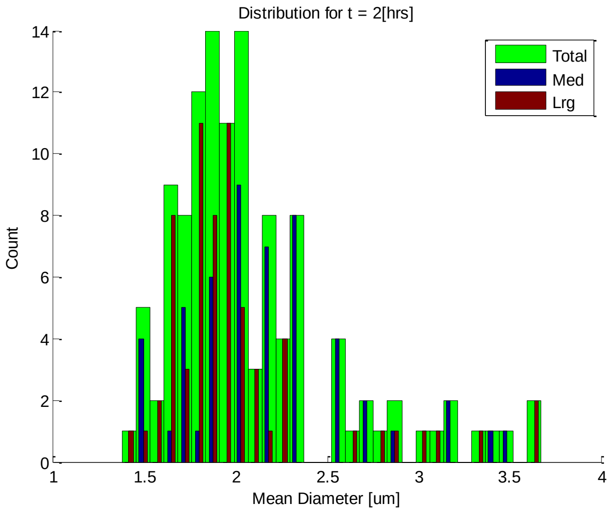

Figure 127 - Detector 096, t = 2[hrs]

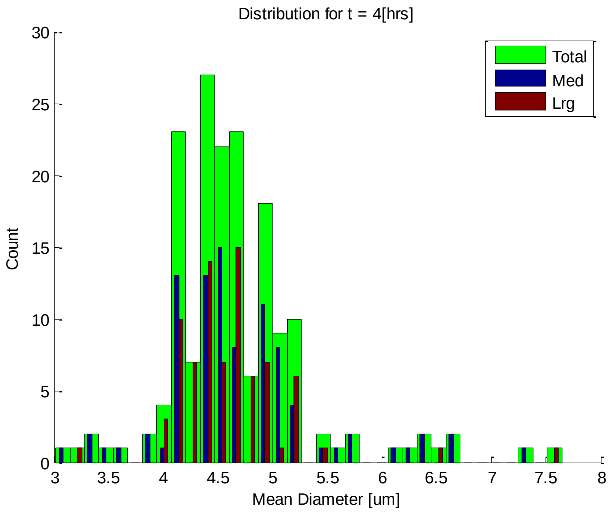

Figure 128 - Detector 096, t = 4[hrs]

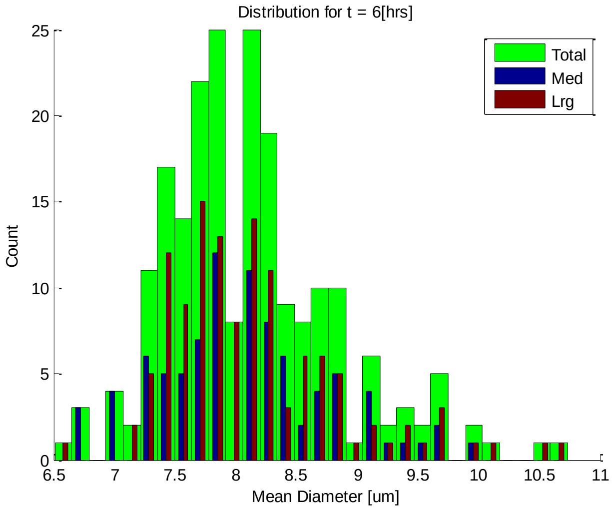

Figure 129 - Detector 096, t = 6[hrs]

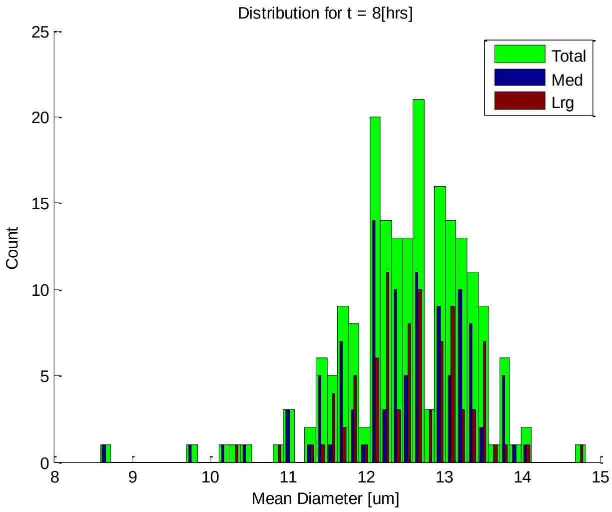

Figure 130 - Detector 096, t = 8[hrs]

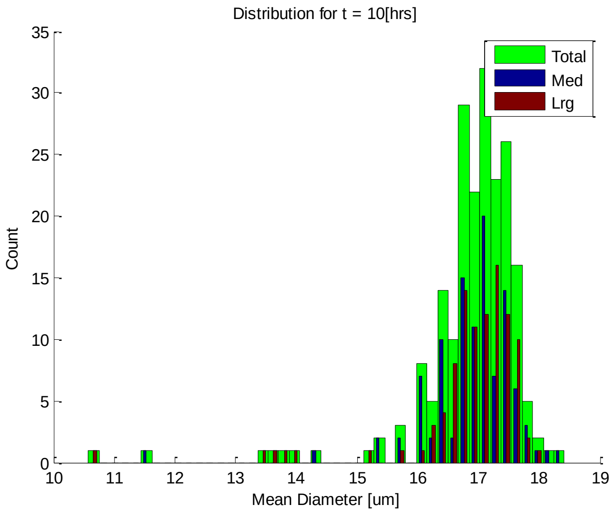

Figure 131 - Detector 096, t = 10[hrs]

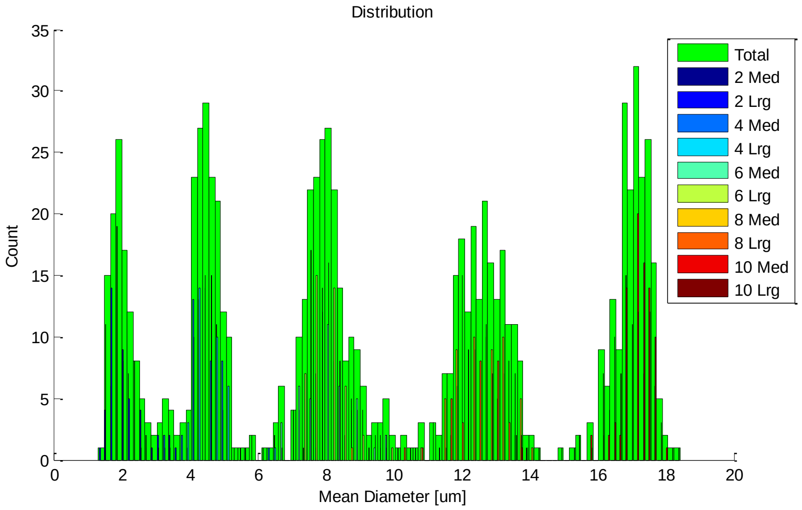

Figure 132 - Detector 096

Figure 127 - Figure 132 show that as with detector 144 the results of detector 096 carry broad width peaks. Figure 127 - Figure 131 are combined in Figure 132, and it can be clearly shown that the mean diameter of the tracks increases for each time step, but not by the same amount. In order to accurately consider the development analysis in a statistic form is required.

12.1.4.3.2. Accuracy

In this section a comparison will be made between the distributions for different measurements at the same time interval. Unless otherwise indicated the box and whisker plot labelled “1” represents measurements taken at a medium distance, and “2” with a large magnification. “3” Is then the combination of these results.

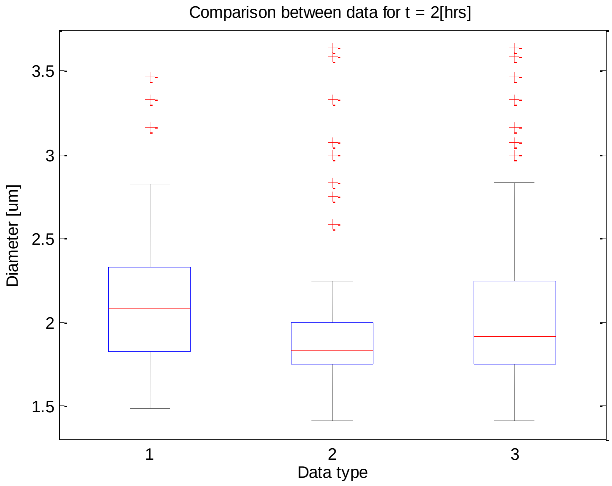

Figure 133 - Data comparison t=2[hrs]

The results at medium magnification are far broader than those for large magnification. At this level the reason for this is that the tracks are remarkably small.

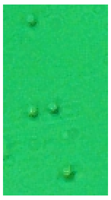

Figure 134 - 096, t=2, med

Figure 135 - 096, t=2, lrg

Figure 134 and Figure 135 show the difference. At this level of magnification the equipment used has a very low resolution. For that reason the results obtained are less accurate for smaller objects. There is however reasonable overlap between the boxes of the measurements.

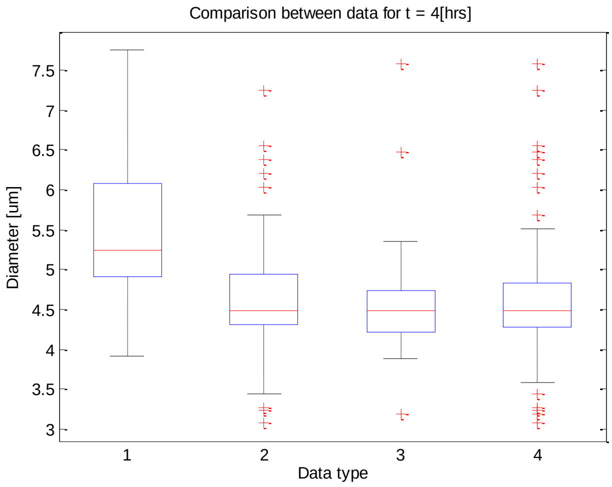

Figure 136 - Data comparison t=4[hrs]

The data indicated as "1" in Figure 136 are the results of detector 144. The other results are the results for detector 096 in the standard order. Considering data 2 and 3 there is very good overlap, especially of the median to provide data 4. Comparison of data 1 and 4 however show very little agreement other than that they are in the same range. These detectors were processed in similar conditions and for the same length of time. It t can only be concluded that subtle environmental differences were present leading to different etching rates. This is one of the main problems with this type of track detector – replication of results is extremely difficult to achieve, and precision equipment should be required.

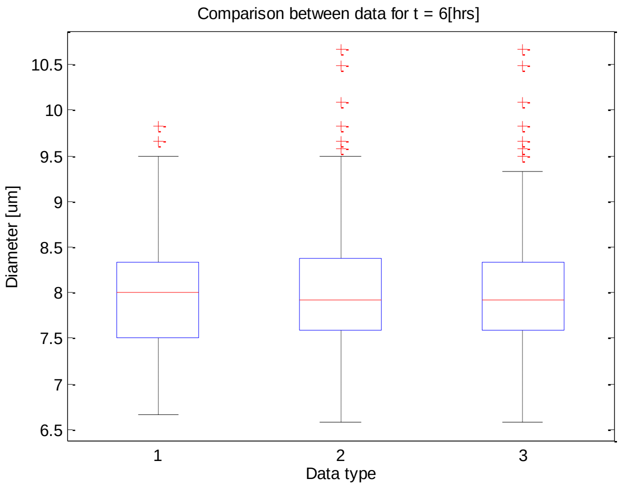

Figure 137 - Data comparison t=6[hrs]

Figure 137 shows very good agreement at 6[hrs].

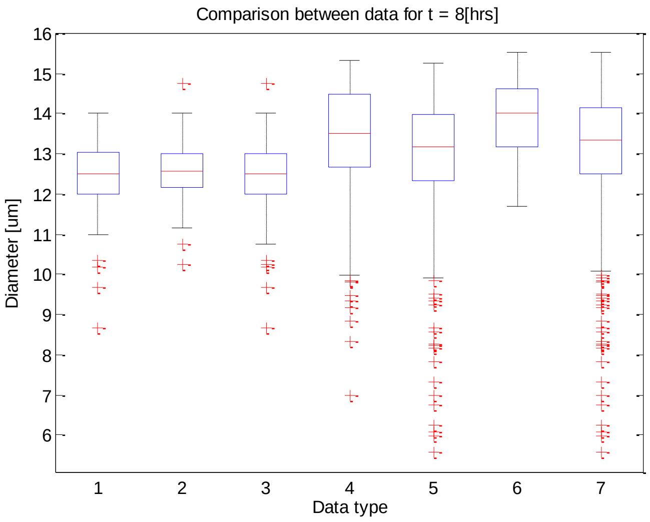

Figure 138 - Data comparison t=8[hrs]

The first 3 sets of data for figure 44 are standard. Data 4,5 and 7 represent the same but for detector 114, where data 6 is the results using the SEM for detector 144. There is very good agreement for each of the detectors respectively. As in figure 42 however the tracks under the same conditions for detector 144 are larger than those in detector 096.

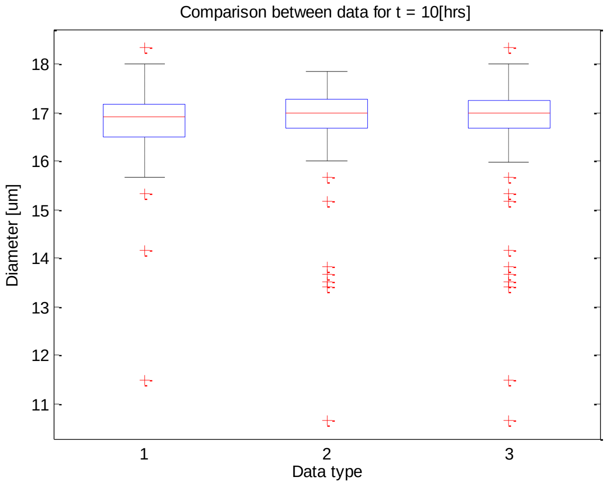

Figure 139 - Data comparison t=10[hrs]

The results for 10 hours also have good agreement.

12.1.4.3.3. Development

The development of each of the detectors should also be considered.

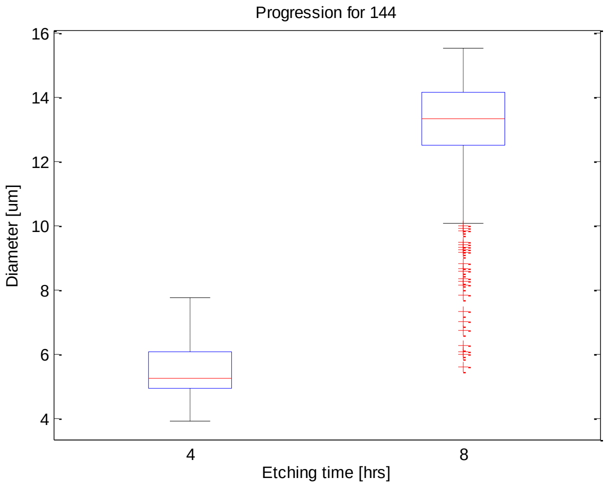

Figure 140 - Development of 144

Table 20 - Numerical representation of Figure 140

	T = 4[hrs]	T = 8[hrs]
Q1 [μm]	4.910306620885412	12.498888839501783
Median [μm]	5.249338582674541	13.329166015421471
Q [μm]	6.082762530298219	14.165686240583852
Width	1.172455909412808	1.666797401082070

Figure 140 clearly shows growth of track diameters. The total increase of the mean is 8.1[um]. The width of the quartile range also increases by about 0.5 in 4 hours. The reason for the increase in width is that tracks development may differentiate enough in this period of time. This means that greater resolution is available for increased etching time with the same equipment.

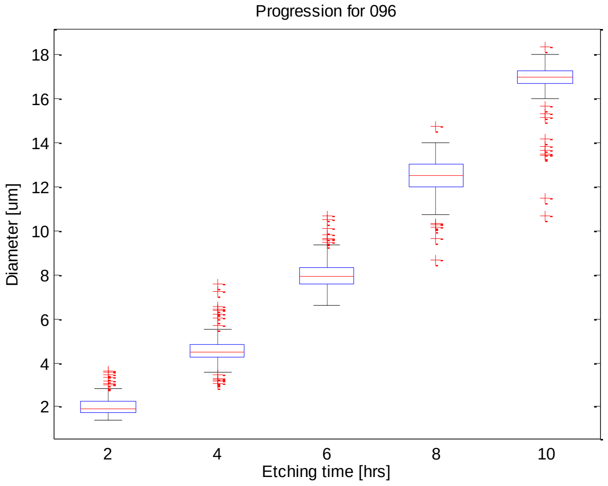

Figure 141 - Development of 096

Table 21 - Numerical representation of Figure 141

	T = 2[hrs]	T = 4[hrs]	T = 6[hrs]	T = 8[hrs]	T = 10[hrs]
Q1	1.748015	4.286122	7.581043	12	16.66396
Median	1.914854	4.482759	7.916228	12.5	16.99673

Q3	2.248456	4.827586	8.333333	13	17.2498
Width	0.500442	0.541464	0.75229	1	0.585841

Analysis of the widths in Table 20 compared to Table 21 indicates that the results obtained from sample 096 have smaller widths, and should as such be considered as more accurate. The width of the fields increases with time, but decreases again after 8 hours. This has to do with the development of tracks indicated in Figure 13, where over etching begins to remove some of the worthwhile data. From this the best resolution for this energy of protons is thus obtained at 8 hours. The increase in the median should also be considered.

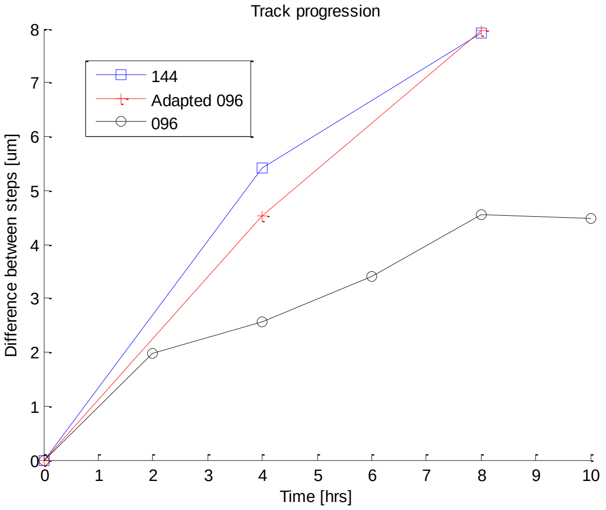

Figure 142 - Median progression

Figure 142 compares the difference in the mean between each previous time step and the next. Since the max means at the same time step have already been shown not to agree. The "adapted 096" line represents the values for 096, but adapted to the same time-steps as 144. Ie. t=2 and t=4 were combined, and the same for t=6 and t=8. Comparing these results to that of 144 indicates that even though there is variation in size, the etching dynamics are similar. The curve represented by 096 implies that the etching rate of change begins to stabilize after 10 hours. This is an indication of the difficulty of track detectors. The etching rate is not constant with time, and should not be assumed as such. It is for this reason that the etching process is so sensitive to environmental conditions.

12.1.4.3.3.1. Measurement errors

The accuracy of the results was considered in another analysis.

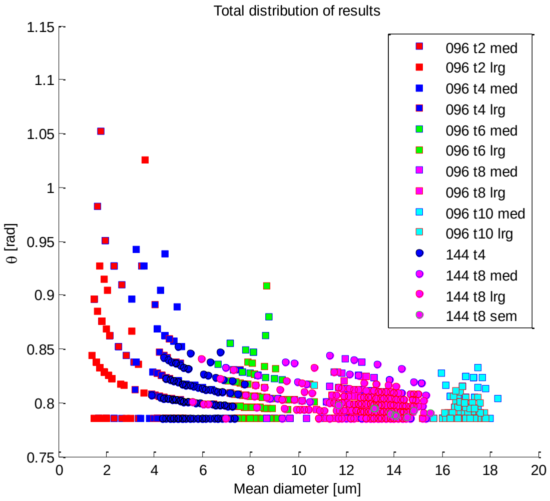

Figure 143 - Result distribution

Since the protons were provided by an accelerator and not a natural source, the incidence of the angles should be 90° in most cases. Under these conditions the minor and major axis should be the same size. As with the α-particles theta was measured again. However for the α-particles theta served as a means of identifying a group, here it is designed to indicate variation. As expected the greatest variation lies at the lower times, since as indicated the resolution was not very good. No conclusions should be drawn from the nearly horizontal line groupings that are shown in Figure 143 since these are simply a function of the resolution of the measurements. Figure 144 shows that the measurements obtained using the SEM (that have a greater resolution) do not fall within these lines.

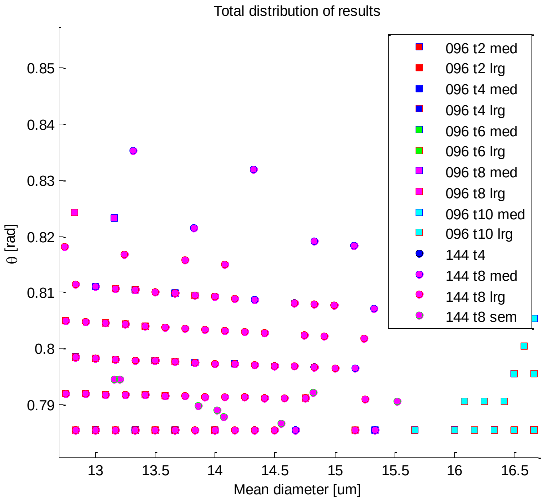

Figure 144 - Closer investigation of Figure 143

12.1.4.4. Conclusions

The largest conclusion that should be drawn from the entire process is that for meaningful results either instrumentation must be extremely precise, of a calibration piece should accompany any investigation in the same etch. Only in this way can the high variation of the etching process be counteracted. It is thus extremely difficult to duplicate results.

The use of copper wire to suspend the samples should also be adapted, since α-particles are produced by this wire. While processing 144 the detector freed itself and was not suspended by the wire. During analysis hardly any background particles were noticed, whereas this is not the case for 096. During the α-investigations too lines were noticed that seemed to lie where the wires were present. Furthermore the difference in flow dynamics between samples 144 and 096 must have played a major role in the difference of etching rates.

Finally it seems that 8 hours is the optimum time to etch this energy of proton particles.